Energy & Environmental Science

ROYAL SOCIETY OF CHEMISTRY

REVIEW

View Article Online
View Journal | View Issue

Cite this: *Energy Environ. Sci.*, 2021, **14**, 2670

A mechanistic study of electrode materials for rechargeable batteries beyond lithium ions by *in situ* transmission electron microscopy

Muhammad Yousaf, [ab] Ufra Naseer, [c] Yiju Li, [bd] Zeeshan Ali, [de] Nasir Mahmood, [f] Lei Wang, [g] Peng Gao *[a] and Shaojun Guo *[bd]

Understanding the fundamental mechanisms of advanced electrode materials at the atomic scale during the electrochemical process is necessary to develop high-performance rechargeable batteries. The complex electrochemical reactions involved in a running battery, which cause intensive structural and morphological changes in electrode materials, have been explored to a certain extent by the use of real-time characterization techniques. *In situ* transmission electron microscopy (TEM) is one of the most noteworthy diagnostic techniques to understand and monitor dynamic electrochemical processes because of its atomic-scale resolution and real-time monitoring, which can provide information about chemical and physical characteristics. In this review, the current progress in the development of electrode materials using *in situ* TEM for rechargeable batteries beyond the lithium ion is summarized. First, the various battery designs used for *in situ* TEM and their challenges are elaborated. Afterward, we systematically summarize the basic science and fundamental reactions including phase transformation and electrode/electrolyte interfaces in electrode materials for heavier alkali ion (sodium, potassium calcium and magnesium) batteries (H-AIBs). Particularly, the real-time insights into three types of electrochemical mechanisms: intercalation, alloying, and conversion reactions are elaborated. Moreover, *in situ* electrode chemistry in lithium sulfur (Li–S) batteries, alkali-metal oxygen batteries (AOBs) including lithium, sodium and potassium oxygen batteries, and all-solid-state batteries (ASSBs) is also discussed. Finally, we provide a summary and future perspective of *in situ* TEM in rechargeable batteries along with the most feasible electrode design.

Received 16th October 2020,
Accepted 22nd February 2021

DOI: 10.1039/d0ee03295f

rsc.li/ees

1. Introduction

Highly efficient and economical energy storage technologies are at the forefront of research to meet the rapidly growing energy requirements of the modern world and to tackle the arising environmental and climate change issues.[1–5] Since their commercialization in 1991, lithium ion batteries (LIBs) have been extensively used in powering portable electronic devices (laptops, mobile phones, smartwatches, *etc.*) and electric vehicles. However, some issues such as high cost, non-uniform distribution of lithium and a relatively low specific capacity are the main threats to economical energy storage from various intermittent renewable energy sources (solar, wind, biomass, *etc.*).[6–9] Therefore, other rechargeable batteries beyond LIBs should be explored for the expansion of energy storage at low fabrication cost.

Heavier alkali ion batteries (H-AIBs) including sodium ion batteries (SIBs) and potassium ion batteries (PIBs) have recently been found to be promising alternatives to LIBs due to their low cost and the high abundance of sodium and potassium.[7,10] Moreover, other high energy density energy storage systems including lithium sulfur (Li–S) batteries and alkali-metal oxygen batteries (AOBs) such as lithium, sodium, or potassium oxygen batteries are also of particular interest.[11–13] In addition, all-solid-state batteries (ASSBs) are more feasible than liquid electrolyte based rechargeable batteries due to their superior safety and

[a] *International Center for Quantum Materials and Electron Microscopy Laboratory, School of Physics, Peking University, Beijing 100871, China. E-mail: pengg@pku.edu.cn*
[b] *School of Material Science and Engineering, Peking University, Beijing 100871, China. E-mail: guosj@pku.edu.cn*
[c] *State Key Laboratory of Resources and Environment Information System, Institute of Geographical Sciences & Natural Resources Research, Chinese Academy of Sciences, Beijing 100871, China*
[d] *College of Engineering, Peking University, Beijing 100871, China*
[e] *School of Chemical and Materials Engineering (SCME), National University of Sciences and Technology (NUST), H-12, Islamabad 44000, Pakistan*
[f] *School of Engineering, RMIT University, 124 La Trobe Street, Melbourne, Victoria, 3001, Australia*
[g] *Key Laboratory of Eco-chemical Engineering, Key Laboratory of Optic-electric Sensing and Analytical Chemistry of Life Science, Taishan Scholar Advantage and Characteristic Discipline Team of Eco Chemical Process and Technology, College of Chemistry and Molecular Engineering, Qingdao University of Science and Technology, Qingdao 266042, P. R. China*

higher energy density. However, these systems are facing many challenges such as low cyclic stability and poor rate capability due to the sluggish diffusion kinetics of Na and K ions in SIBs and PIBs, respectively,[14–16] soluble polysulfide shuttle effects in sulfur batteries[17] and the insulating nature of discharge products in AOBs.[13] The stability issues of solid state electrolytes (SSEs) and high resistance at interfaces in ASSBs are also very critical.[18] To put these alternative rechargeable batteries into commercial applications, a profound understanding of electrochemical reactions and the development of strategies to prevent the failure of cells are necessary.

Anodes, cathodes and electrolytes are the essential components of rechargeable batteries and the improvement in cell performance needs advancement in these battery components. Therefore, a better understanding of mechanical degradation in electrodes, the formation of electrode/electrolyte interfaces, internal battery mechanisms, and the microstructural and morphological evolution of electrode materials during battery operation is necessary to design innovative electrodes and electrolytes.[19,20] In this regard, real-time information during the operation of the battery is very imperative to enhance the electrochemical performance.[21–23] This information can be obtained by monitoring the dynamics of electrochemical reactions during the charge/discharge processes. The real-time observations may include the understanding of active/inactive interface formation, evolution of intermediate reaction products, diffusivity of ions in the electrodes, propagation of grain boundaries and metal ion coordination in active materials. The information will be helpful in optimizing and designing various components of rechargeable batteries including anodes, cathodes and electrolytes, and, in turn, contributing to further improvement in battery performance. However, this information cannot be obtained using *ex situ* characterization techniques, as these rechargeable devices need a sealed working environment and are hard to stop the reaction at a specific point. This has propelled the development of *in situ* characterization tools to obtain real-time information, revealing the evolution of battery electrodes and their complex electrochemical reactions.[21,22,24,25]

Various *in situ* techniques have been used to characterize these processes, each with its advantages and limitations. For instance, X-ray diffraction (XRD), neutron diffraction, Raman spectroscopy and X-ray photoelectron spectroscopy (XPS) can be used to study the structural properties and chemistry of electrodes, but only at the bulk level.[26] Scanning electron microscopy (SEM) provides the real-time changes in the surface morphology of electrodes at the nanoscale, but cannot provide information about atomic-level structural dynamics. Atomic force microscopy (AFM) is limited to providing the local morphology and structure information (volume change and ion and electron transport) of electrode materials at the atomic scale.[27] In contrast, *in situ* transmission electron microscopy (TEM) is a powerful tool due to its high spatial resolution, having the ability to investigate the morphology, volume changes, composition, atomic structure, material phases and electronic structure of individual electrode particles and interfaces in real time; in fact, a single technique can provide all the information at the atomic level.[28] Therefore, *in situ* TEM is an emerging approach that can provide substantial insights for understanding the fundamental mechanisms that are responsible for capacity fading during the electrochemical process, the degradation of electrodes, thermal runway and safety issues. The first *in situ* TEM experiment for electrode materials in LIBs was conducted in 2010.[29] Since then, a lot of progress has been made in investigating advanced electrodes in real-time operation for rechargeable batteries.

Many articles extensively reviewed the *in situ* TEM study on traditional LIBs,[24,28,30–37] but there is a lack of studies on other rechargeable batteries including SIBs, PIBs, multi-ion batteries (Ca^{2+}, Mg^{2+}, Al^{3+}, *etc.*), Li–S batteries, ASSBs and MOBs including Li–O_2 batteries, Na–O_2 batteries, and K–O_2 batteries. It is worth noting that the chemistry and design, as well as TEM output, of these batteries are entirely different from those of traditional LIBs, and therefore a comprehensive review that covers the most significant contributions made for other rechargeable battery systems is highly desired. The major aim of this review is to summarize the electrochemical behavior of various electrode materials beyond LIBs, in which we will highlight the science and discoveries revealed by *in situ* TEM beyond lithium chemistry. The basic challenges and various battery designs used for *in situ* TEM are discussed in detail. Four types of battery systems including H-AIBs, Li–S batteries, AOBs and ASSBs are presented, and we will discuss how *in situ* TEM helps the researchers to understand the reaction mechanisms and basic science in a battery during the charging and discharging processes. Through these observations, one will be able to tackle the barriers of current electrodes and also configure the novel materials for high performance batteries.

2. Fundamentals and development of *in situ* TEM for rechargeable batteries

TEM is an advanced technique that directly visualizes the materials at a sub-atomic-scale and provides information about crystallography and chemical composition as well. With highly efficient electron detection systems and aberration correctors, the temporal and spatial resolutions of TEM can be effectively improved. However, the real-time events occurring inside the sample such as the electrochemical phenomenon in working rechargeable batteries cannot be visualized in traditional TEM. By introducing suitable external stimuli such as electrical, optical, mechanical, heating, and cooling in TEM in combination with different functional sample holders such as an electrical biasing holder or a heating chip, complex processes during the working condition of a device can be investigated.[25] The stimuli can be applied either in vacuum or under liquid or gas environments, examining the phenomenon at solid–solid, solid–liquid, and solid–gas interfaces, respectively. Up to now, various TEM holders have been introduced to study the interesting phenomenon in real time. For example, the *in situ* heating chip is used to investigate the dynamic microstructural evolution at the atomic scale during a high temperature calcination process. The electric biasing holder under vacuum

has the ability to study the electrochemical phenomenon in electrode materials or solid electrolytes of rechargeable ion batteries (LIBs, SIBs, KIBs, ASSBs, Li–S batteries, *etc.*). The TEM holder, having the ability to combine the electric biasing with liquid, can be used to examine the dynamic electrochemical processes of electrodes at a solid–liquid interface in rechargeable batteries. Moreover, the TEM holder-integrated electric biasing in a gas-cell or environmental TEM (ETEM) could be utilized to explore the reaction mechanisms of MOBs. However, the operation of TEM requires a high vacuum, while electrolytes used in most rechargeable batteries are organic liquids or volatiles that are incompatible with the vacuum conditions of TEM and cannot be used directly. Therefore, finding a suitable electrolyte and cell design to be used in the TEM column with a high vacuum of $\sim 10^{-5}$ Pa is a grand challenge. Broadly speaking, open cell and sealed liquid cell nanobattery setups have been used in *in situ* TEM to study the electrochemical processes. In the following section, we will elaborate on the various *in situ* TEM cell designs for rechargeable batteries, and their schematic description is shown in Fig. 1.

2.1. Ionic liquid open cell design

The liquid open cell nanobattery was first successfully assembled by Huang and his co-workers[29] using a low vapor pressure ionic liquid electrolyte, which can maintain a high vacuum in the TEM column. It consists of an individual nanowire as the working electrode (anode), $LiCoO_2$ as the cathode and lithium bis(trifluoromethanesulfonyl)imide (LiTFSI) dissolved in a hydrophobic ionic liquid, 1-butyl-1-methylpyrrolidinium (P_{14}) TFSI (P14TFSI), as the electrolyte.

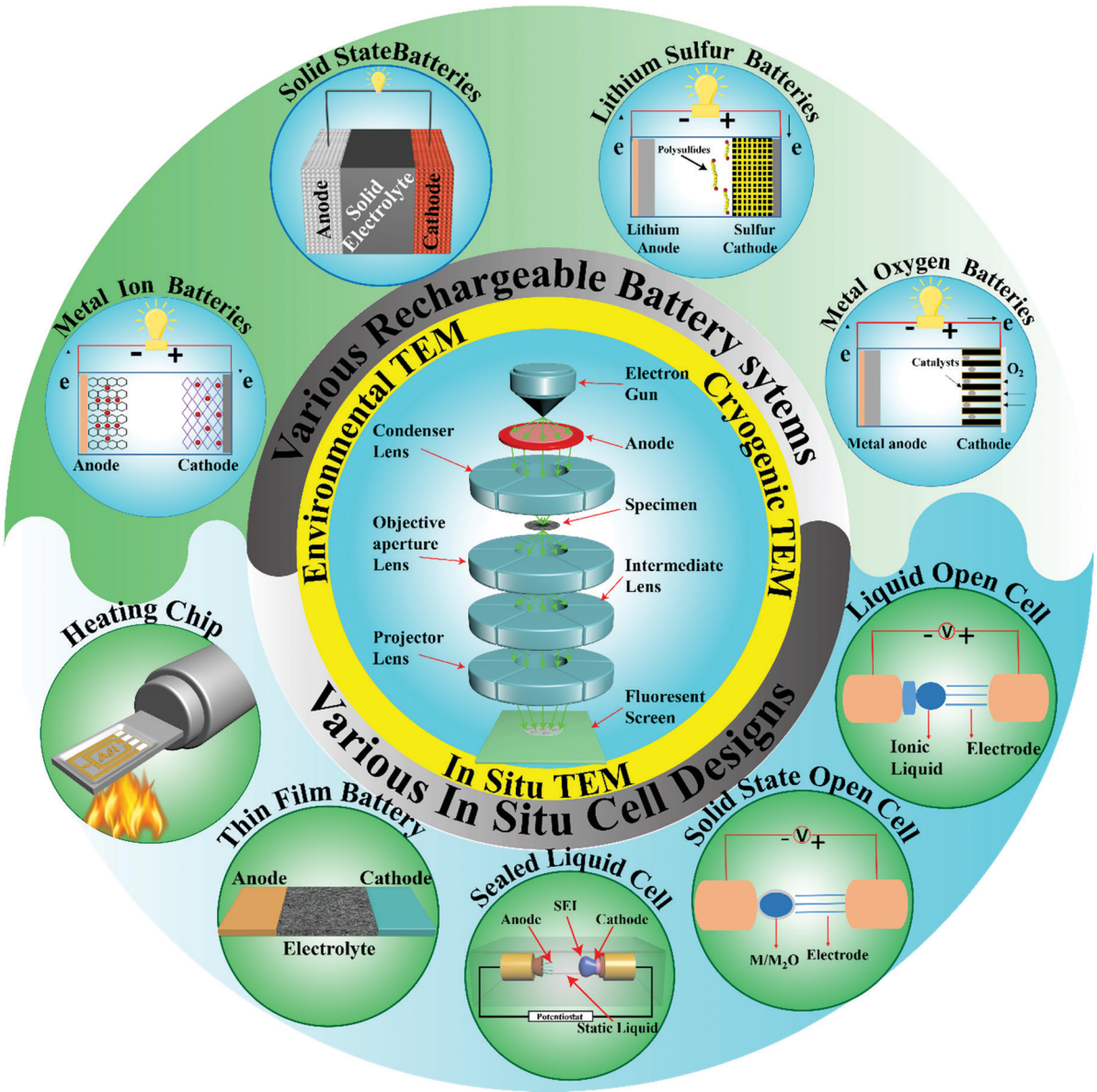

Fig. 1 Schematic illustration of various innovative nanocell designs for *in situ* TEM to study various rechargeable batteries.

The liquid open cell design is particularly compatible with electrochemical testing of one-dimensional nanotubes or nanowires. It is also observed that the ionic liquid can distribute uniformly on the entire surface of the nanowire like a thin film coating. Therefore, this design may mimic the practical battery to some extent. However, the ionic liquid electrolyte may polymerize during the operation of the battery, which is the main drawback of this design. Consequently, the battery may run only for few cycles, which is not enough for studying the structural evolution of the electrode materials.

2.2. Solid state open cell design

In this design, the *in situ* biasing holder applies the bias between the electrode and the scanning tunnelling microscope (STM) holder tip, where an alkali metal is placed on the STM tip that serves as the anode. The metal oxide thin layer (Li_2O, Na_2O, K_2O) is spontaneously formed on the alkali metal (Li, Na, K) when exposed to air during the insertion of the holder into the TEM column that further shields the alkali metal surface and serves as a solid electrolyte. However, alkali metal oxide has low conductivity, and therefore a negative voltage of 2–4 V is usually applied between the anode and cathode to move the alkali ions into the cathode. It provides a high spatial resolution and more insightful information about the structural and morphological evolution of targeted nanostructured materials. Besides, the all solid state open cell design has two advantages over the liquid open cell design. Firstly, the entire active material is apparent throughout the *in situ* electrochemical experiment. Secondly, very small particles even in the range of a few nanometers can be observed and imaged during battery operation. Therefore, the all solid state open cell design is most commonly used to probe the *in situ* electrochemical processes. However, it still has some drawbacks: (1) the open cell design is not compatible with the real liquid electrolyte battery due to its different point-contact geometry and large contact resistance at the electrode/electrolyte, which may alter the diffusion pattern of metal ions. (2) Many real battery phenomena at the electrode/liquid–electrolyte interface like the evolution of the solid electrolyte interphase (SEI) film and the generation of metal dendrites cannot be observed. (3) It is a partial cell system, and one component of electrode/electrolyte connections can be observed at a time. (4) In the all solid state open cell, alkali metal oxide is used as the electrolyte, and a large potential is required to drive alkali ions into the electrodes that may alter the ionic kinetics and electrochemical behavior of the electrode.

2.3. Thin film nanobatteries

Commercialized SSEs like LLZO and LiPON that cannot be tested using the open cell design are investigated using thin film nanobattery design, where the interface instability, buried interfaces, high interfacial impedance and low ionic diffusivity are the targeted points of investigation. The focussed ion beam (FIB) procedure has been broadly used to prepare the electrochemically active nanobatteries for *in situ* TEM. However, sample fabrication for *in situ* TEM studies using FIB techniques is a quite challenging task due to preferential sputtering, re-coating and surface damage at high current densities, and in most of the cases thin film nanobatteries fail to maintain the electrochemical activity due to short circuiting.[38–40] Numerous approaches to reduce this surface damage such as gas-assisted, low energy FIB, wedge pre-milling step, and cleaning by broad ion beam milling have been proposed to realize the electrochemically active thin film nanobatteries.[39,41,42] Santhanagopalan *et al.*[5] were the first to present the noteworthy FIB fabrication parameters for thin film nanobatteries, which could maintain the electrochemical activity. Later on, a lot of thin film nanobatteries were fabricated using the FIB technique to study the interfacial behavior and electrochemistry of ASSBs.[43,44]

2.4. *In situ* heating chip

The *in situ* heating chip has been used to study the local structural changes during thermal treatment at elevated temperatures. It consists of a TEM lamella sample which is transferred onto the *in situ* heating chip and then mounted onto the *in situ* TEM holder, where a uniform temperature field up to 1300 °C can be applied. The *in situ* heating chip examines the thermal stability of the metal oxide based cathode (P2–Na_xCoO_2, $Li_xNi_yMn_zCo_{1-y-z}O_2$) in alkali ion batteries, where surface degradation, phase change, loss of oxygen, and thermal runway are explored.[45,46] In this way, the improvement in the thermal stability of metal oxide based cathode materials may be possible by controlling their chemical composition. Moreover, the microstructural evolution of SSEs at high temperatures during the synthesis process can also be realized using the *in situ* heating chip in TEM that is crucial for realizing high safety and high energy density ASSBs.

2.5. Sealed liquid cell design

The shortcomings of the open cell design can be overcome using a sealed liquid cell configuration, which can prevent the polymerization of the ionic liquid electrolyte and the poor conductivity of the alkali metal oxide electrolyte. It is compatible and close to real batteries, and therefore the study of SEI generation and growth, and the evolution of dendrites at the electrode/electrolyte interface can be achieved. The first sealed liquid cell design was created by the Gu group.[47] It consists of an individual nanowire as the observer electrode, an alkali metal as the counter electrode, and a thin liquid layer with a thickness of 500–1000 nm as the electrolyte.[24,47] The whole components are sealed with a 20–50 nm thick, electron transparent SiN_x membrane in an Ar-filled glove box. Further, the potential of the sealed liquid cell is increased with the advancement of low-dose automated image acquisition approaches and new imaging detectors like the direct detection device (DDD). Using the closed cell design, (i) a full battery system can be made in which all components, *i.e.* cathode, anode, electrolyte and electrode/electrolyte interfaces, can be investigated at the same time and (ii) organic (volatile) liquid electrolytes can be used. The sealed liquid cell design has some shortcomings as well: (i) the necessary precautions are very

important in using the sealed liquid cell design because after loading the device into the TEM the membrane may lump outward because of the pressure differences. (ii) The evaporation of liquid electrolytes can place the vacuum TEM column at high risk. (iii) The spatial resolution imaging is limited due to the conformal coating of the electrolyte on the working electrode. (iv) The interaction between the suspending medium and electron beam is severe, resulting in bubbles or hydrogen generation, and changes in pH.

2.6. Emerging TEM techniques to study the battery material

2.6.1. Environmental TEM. Traditional TEM has shown tremendous progress to study the dynamic processes of battery materials using various cell designs; however, it has some limitations. For example, in the case of MOBs, the sealed liquid cells have been applied to characterize the mechanisms of chemical reactions by many researchers. They illustrated the benefits of liquid cells (*i.e.* can study the chemical dynamics at ambient pressure) to observe these electrochemical dynamics.[48–54] However, visualization may distort by the interaction of the electron beam with SiN_x membranes, resulting in a lower imaging resolution. Moreover, a high internal vacuum is required in TEM, which precludes the running of the battery in a gas environment. The advent of ETEM allows gas flow in the TEM specimen chamber up to 3000 Pa by differential pumping and high resolution imaging at elevated temperatures. This leads to the use of all commercially available *in situ* TEM holders without modifications.[55] Moreover, it creates an oxygen-rich environment in the vicinity of the running battery, resulting in realistic MOB experiments in ETEM. A lot of pioneering works have been reported by many researchers using open cell designs in ETEM and made substantial innovations for the development of MOBs.[56–61] However, still, the interaction between the fast electrons and gas cannot be neglected because it may cause the ionization of gas molecules, and affect the spatial resolution or beam-induced etching at the specimen, so further development in TEM characterization techniques is required.

2.6.2. Cryogenic TEM. A lot of advancements have been made to study the *in situ* electrochemical dynamics of rechargeable batteries using innovative cell designs in traditional TEM and ETEM as discussed above. However, investigations of these standard characterization techniques are not able to retain the pristine state of electron beam sensitive battery materials (Li, Na, sulfur-based electrolytes, *etc.*) after the operation. It has been demonstrated that these highly chemically active materials can preserve the native state under cryogenic conditions.[62] This has made possible the atomistic imaging of these electron beam sensitive battery materials under cryogenic conditions using cryogenic TEM (cryo-TEM). For instance, Li *et al.* studied the single crystalline Li metal and its interfaces with the SEI at atomic scale resolution using cryo-TEM. They observed that the Li dendrites grew along various crystallographic directions.[62] With cryo-TEM a complete insight into the failure mechanism such as a change in SEI nanostructures and the formation of dendrites in a different environment could be obtained, which was not possible with traditional TEM. Similarly, the sulfur cathode material in the Li–S battery was characterized by cryo-TEM without sublimation artifacts and made the observation concrete.[63] Using cryo-TEM many investigations for Li metal plating/stripping and interface chemistry between the Li metal and solid or liquid electrolytes have been reported.[64–67] However, cryo-TEM is not compatible with the in *operando* study, which is the major limitation of the cryo-TEM study.

In summary, each nanobattery design and developed approach has its own merits and demerits. However, all these *in situ* advancements will provide a clear understanding of the mechanistic insights and reaction mechanisms in rechargeable batteries and guidance to design and optimize the battery materials beyond the limits of recent techniques with an emphasis on high-performance rechargeable batteries.

3. Electrode materials used for H-AIBs and associated challenges undermined by *in situ* TEM

Undoubtedly, the *in situ* TEM study has been widely used to examine the (dis)charge process in LIBs; however, its practicability for H-AIBs is not fully established as its use is still at the initial stage. Moreover, the investigated dynamic electrochemical processes for H-AIBs demonstrate different features compared with intensively studied Li ions due to the variation of ionic sizes and electronegativities.[19,23,30] Using the open solid state nanobattery cell design, various electrode materials including carbonaceous allotropes, metal oxides, metal sulfide/selenides, and semiconductors (Ge) have been examined as electrode material candidates for H-AIBs. In the following sections, we will summarize the *in situ* TEM study for H-AIBs including SIBs, KIBs, and multi-ion batteries.

3.1. Sodium ion batteries

The type of charge storage mechanism involved in novel electrode materials and the mechanical behaviour upon sodiation/de-sodiation need consideration to improve the battery performance. In the early stage, most of the studies to examine the charge storage mechanism in electrode materials were carried out under *ex situ* conditions, which means that the structural and morphological characteristics were analysed before and after battery cycling.[68] However, some dynamic phenomena during (dis)charge remain unidentified. Therefore, an advanced understanding of electrochemical processes during the running of the battery is essential for the development of advanced electrode materials for SIBs. Generally speaking, electrode materials are classified into three types, *i.e.* intercalation, alloying and conversion reactions, based on their charge storage mechanisms. In the following sub-section, we will illustrate the challenges associated with these three kinds of reaction mechanisms in SIBs.

3.1.1. Insertion dynamic studies in intercalation-based materials. Intercalation type reactions involve the insertion of ions in the vacancies or defects available in the electrode material and mostly occur in carbon-based materials and

layered structured materials. However, heavy alkali ions like Na have larger radii than Li ions, which affects the charge storage and mass transport during the electrochemical process.[69–71] Since the first study on the insertion of Na ions into carbon, many disordered and expanded carbon based materials have been reported extensively as anode hosts for SIBs.[72] However, how carbon based electrodes behave during sodiation/de-sodiation processes, *i.e.* storage behavior of sodium ions in various active sites, formation of cracks, volume variations, low first coulombic efficiency (CE), and structural and micro-morphological evolution during the electrochemical process, is very important. Therefore, *in situ* TEM was used to retrieve the sodiation/de-sodiation reactions in various carbonaceous materials including soft carbon,[73] hard carbon,[74,75] expanded graphite (EG),[76] carbon nanofibers (CNF)[77] and reduced graphene oxides (rGO).[78] It is observed that the microstructure of pristine EG contained well aligned and robust long-range-ordered graphitic layers (Fig. 2b and e) with a large spacing between the layers. After the insertion of Na ions into EG, the original shape of EG changed by distorting or tilting to buffer the extensive morphological variations. Besides, the complicated microstructural disordered and ripple-like features in the graphitic layered pattern were found in EG after sodiation (Fig. 2c and f). The electron diffraction pattern (EDP) verified the accommodation of Na ions in between the EG layers (Fig. 2j). During the de-sodiation process, the microstructure of EG reverted to its original shape (Fig. 2d and g) with a negligible amount of Na ions remaining in de-sodiated EG (Fig. 2k), showing high Na ion reversibility in EG. During this study, no direct image of the reaction front was found due to negligible variations of volume during sodiation/de-sodiation, but reversible microstructure processes were detected. These characteristics resulted in a high specific capacity of 284 mA h g^{-1} at 20 mA g^{-1}, outstanding cyclic stability with 2000 cycles and good rate capability (Fig. 2l and m).

In the case of hard carbon, the high potential slope region in the galvanostatic voltage profile is due to either the intercalation mode or the adsorption mode during the first discharge process,

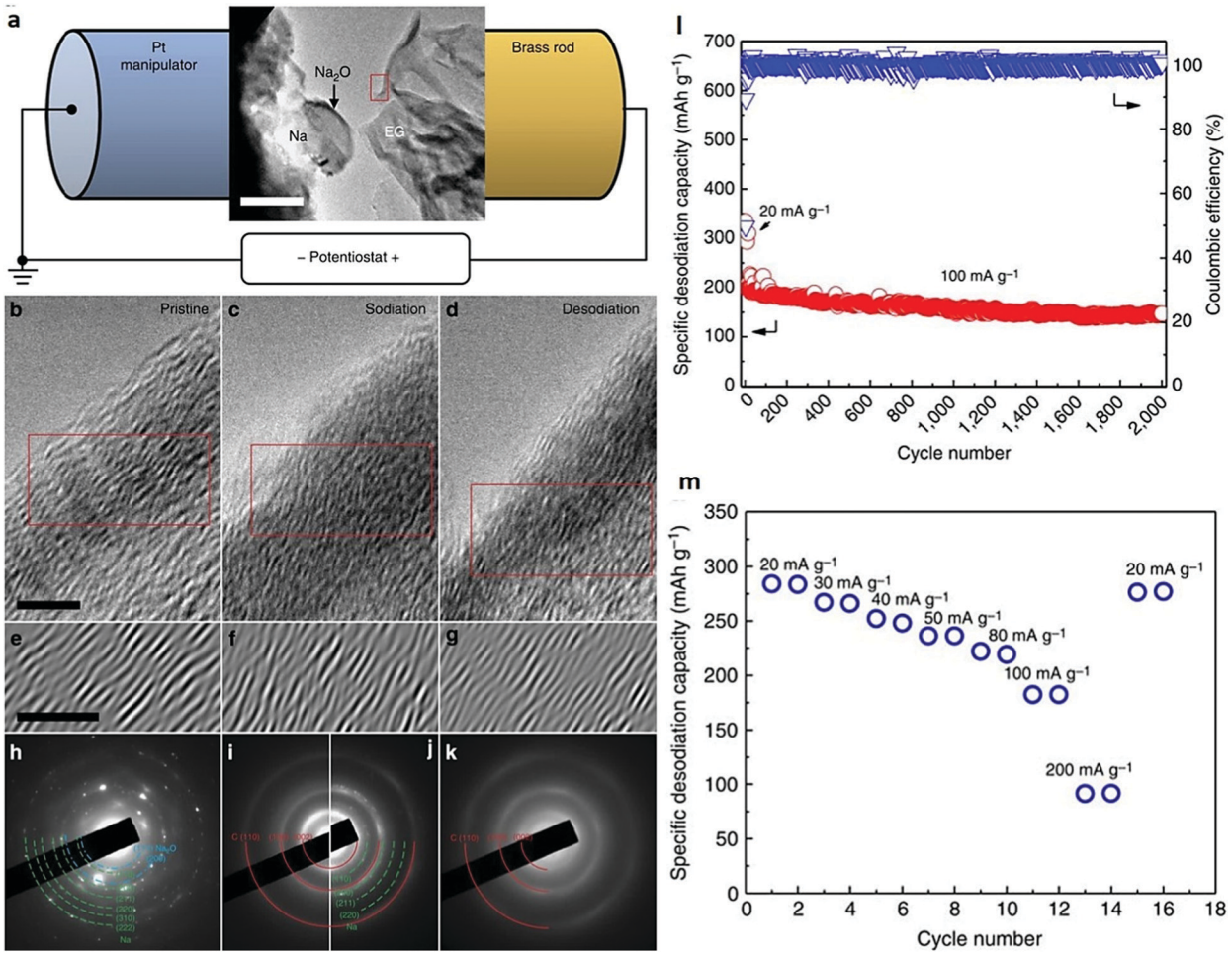

Fig. 2 *In situ* TEM investigation and electrochemical performance during sodium ion intercalation in EG. (a) Schematic illustration of the *in situ* experimental setup. (b–d) Typical microstructures of (b) pristine EG, (c) EG after the first sodiation, and (d) EG after the first desodiation. Scale bar, 5 nm. (e–g) High resolution TEM images corresponding to the boxed areas in b–d, respectively. Scale bar, 5 nm. EDP from (h) the Na source area, (i) EG at pristine state, (j) EG after the first sodiation, and (k) EG after the first desodiation. (l and m) Cyclic stability and rate performance tests of EG. Reproduced with permission.[76] Copyright 2014, Nature Publishing Group.

which was clarified using *in situ* TEM. From *in situ* TEM experiments, it was evidenced that the first sodiation process of hard carbon started with Na ion absorption to high energy sites in the defects, pores or surface (at a high voltage, 2.0 to 0.15 V), followed by intercalation of Na ions in the curved carbon platelets (at a lower voltage, ~0.15 V), which represent the "absorption to intercalation mode".[74] The interlayer distance of hard carbon increased from 0.38 nm to 0.40 nm during the intercalation process, resulting in more ordered graphene layers upon this process. A volume expansion of 10.6% in hard carbon during sodiation was found, which was larger during the intercalation plateau compared with absorption. However, Na ion diffusion during absorption was faster than intercalation as absorption occurred directly at the surface.[74] The sodium storage capacity of hard carbon could be increased by optimizing the pores with a size of a few nanometers with a suitable graphite interlayer distance. Similarly, using *in situ* TEM, the volume expansion in bi-layer CNF anodes upon sodiation could also be observed. The CNF consisted of disordered carbon (d-C) as the outer wall and crystalline carbon (c-C) as the inner wall which expanded to 18.7% and 13.7%, respectively, after sodiation (Fig. 3a and b).[77] Moreover, the interlayer spacing[24] increased for both c-C and d-C from 3.38 Å to 3.67 Å and 4.67 Å, respectively, the value being higher for d-C (4.67 Å) than that for c-C (3.67 Å), which represents higher electrochemical performance in the d-C layers (Fig. 3c–e). Incidentally, a thin film of Na_2O was formed spontaneously on the surface of CNF, whereas bulk sodiation was still continuing, signifying fast diffusion of Na on the CNF (Fig. 3a and b).[33,77,79] It was also suggested that Si could not be a worthwhile anode electrode for SIBs because no changes were observed in the thickness of Si coating on CNF during sodiation.[77] In the case of rGO,[78] the *in situ* electrochemical behavior revealed the reversible growth of Na metal clusters (with a size of >10 nm) on the rapid rGO surface during sodiation. Moreover, rGO nanosheets were curled up along with the deposition of the Na_2O layer after sodiation which was retained on the rGO after the full first de-sodiation. This irreversible deposition of Na_2O produced a side reaction which was considered to be the main reason for the capacity loss during the first sodiation/de-sodiation process.[78] The Na ion storage mechanism in the rGO based anode consisted of two parts: firstly, in a slope region (between 2.0 and 0.3 V), the Na

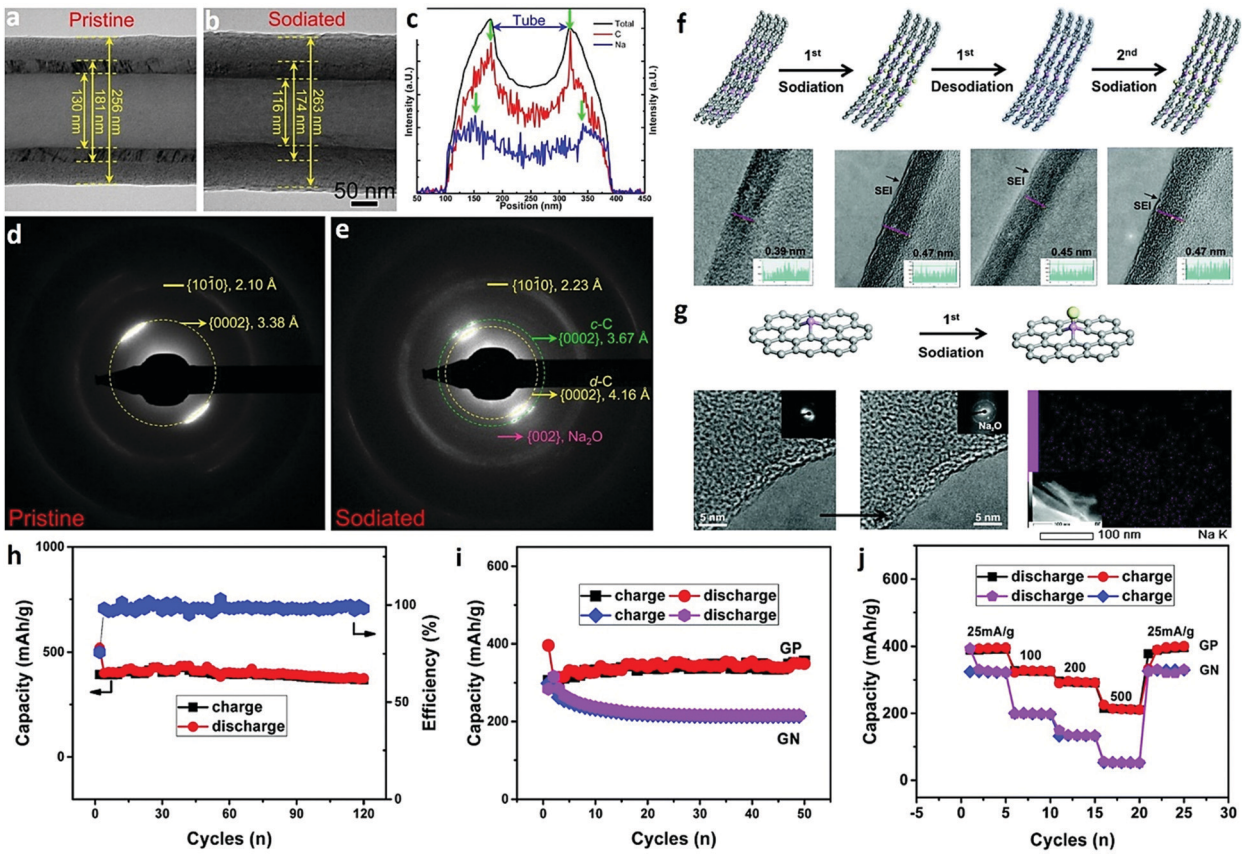

Fig. 3 *In situ* TEM study of the intercalation mechanism in various carbonaceous materials: (a–e) geometry and structure changes of a bilayer CNF upon sodiation. (a) Pristine CNF, (b) sodiated CNF and (c) the line scan profiles of C and Na across the CNF after sodiation. (d and e) EDPs of the CNF before and after sodiation, respectively. Reproduced with permission.[77] Copyright 2014, American Chemical Society. (f–j) Real-time investigation and electrochemical characterization of GP and GN: (f) schematic description and HRTEM micrographs of the micro-structural evolution of the GP edge upon the sodiation/de-sodiation processes. (g) Schematic explanation and HRTEM pictures of the surface structural changes of GP upon sodiation. (h) The cycling performance and CE of GP at 25 mA g^{-1}. (i) Comparison of the cycling performance of GP and GN at 50 mA g^{-1}. (j) The rate capabilities of GP and GN. Reproduced with permission.[81] Copyright 2017, Royal Society of Chemistry.

ions were stored due to defective sites and functional groups. Secondly, below 0.3 V, Na ions were inserted due to the intercalation process in between the interlayers of rGO and Na metal clusters adsorbed on the surface of rGO.[78] These *in situ* TEM findings not only are important for rGO based electrodes in SIBs, but also facilitate the understanding of the electrochemical reactions and the design of a dendrite-free Na metal electrode.

As mentioned above, many carbonaceous electrodes have been reported for SIBs, but their Na ion storage capacity still needs to be improved to achieve a light weight storage system. The introduction of defects (holes, protrusions) *via* doping with nitrogen (GN) and phosphorus (GP) into graphene could be a suitable approach to improve the performance.[81] The underlying mechanism observed by *in situ* TEM revealed reversible volume expansion (20.5%) with lateral expansion from 0.39 nm to 0.47 nm before and after sodiation in GP. A thin SEI layer was also observed during the electrochemical process of GP nanosheets (Fig. 3f) and its basal plane turned into an uneven and rough surface after the first sodiation. This indicated that Na ion insertion into or onto the basal planes of nanosheets is similar to the lithiation process (Fig. 3g).[82] Moreover, the real-time sodiation/de-sodiation process revealed that Na ions could be stored in the GP nanosheets *via* both insertion and adsorption processes, while only the adsorption process occurred in GN, indicating higher Na storage in GP compared with GN (Fig. 3h–j).[81] This was attributed to almost no change in the lateral distance of GN before and after the sodiation process (0.36 nm *vs.* 0.37 nm),[81] signifying that Na ion insertion does not occur on the GN edge, because theoretically a minimum interlayer spacing of 0.37 nm is required for the insertion of Na ions into carbon based materials.[83] Due to the dual Na storage process (*i.e.* insertion and adsorption), the GP exhibited a high capacity of 374 mA h g^{-1} at 25 mA g^{-1} after 200 cycles and displayed an outstanding rate performance (210 mA h g^{-1} at a current density of 500 mA h g^{-1}) (Fig. 3h–j).[81] Therefore, instead of holes in GN, introducing protrusions in GP can be a potential and effective way to improve the electrochemical performance for SIBs.

Besides carbonaceous materials, the intercalation type charge storage mechanism was also involved in layered structured materials such as in cathode materials and transition metal dichalcogenides (TMDs). Sodium transition metal oxides (Na_xTMO_2) are widely used as cathode materials for SIBs due to their high energy density. The chemical and morphological evolution of P_2–Na_xCoO_2 during battery operation in TEM was investigated in depth,[45] wherein the crystallography and morphologies of Na_xCoO_2 changed at elevated temperatures. The results showed that, with an increase in temperature, the surface of Na_xCoO_2 became porous because of thermal decomposition, indicating that the evolution of gas was the main reason for structure degradation (Fig. 4a–c). This thermal decomposition becomes more severe at a higher voltage at a similar temperature (Fig. 4d–f).[45]

Intercalation reactions were also observed in some TMDs.[84] For instance, Gao *et al.* reported a two-phase reaction mechanism involved in layered MoS_2 during Na ion intercalation.[84] It was a phase transition from trigonal prismatic 2H-MoS_2 to octahedral 1T-$NaMoS_2$, followed by the propagation of an $\sim$2 nm thick phase boundary with a velocity of $\sim$3–7 nm s^{-1}. This velocity is 10 times slower than that in lithiation,[85,86] suggesting sluggish kinetics of Na ion diffusion into MoS_2 based anodes; however, the charge storage mechanism is similar for both lithiation and sodiation.[84,85] However, in the case of layered TiS_2, a distinct intercalation reaction was observed during sodiation and lithiation.[87,88]

These reports have provided information on the chemical, structural and morphological evolution in intercalation-mechanism-type materials including carbonaceous materials, layered sodium transition metal oxides and TMDs *via in situ* TEM. These studies have provided valuable guidance, and new paths and horizons to electrochemists for the development of novel electrode materials (*via* surface modification or structural engineering) with improved sodium storage capacity.

3.1.2. Volume and microstructural variations in alloying materials. The alloying-type reaction takes place *via* direct bonding between the host element and the inserted Na ions.[28] Mostly it occurs at low voltages (*versus* Na^+/Na), yielding a high ratio of Na per formula unit (Na–A, where A is Sn, Ge, P, Sb, *etc.*) and thus providing high theoretical capacity and energy density.[20] With the development of high energy density alloying-type anodes, it is important to understand the sodiation/de-sodiation process of alloying reactions. Contrary to the intercalation mechanism, which takes place with slight modifications in the local crystal structure and morphology (*i.e.* small volume expansion/contraction) of the host material, alloying reactions were accompanied by entire reconstruction of the crystal structure and formed new phases.[20] It caused large volume changes that led to the pulverization and degradation of active materials, which consequently detached from the current collector, and thus capacity fading. Therefore, a comprehensive understanding of mechanical degradation and phase transformation of the active materials is very important to achieve highly stable and long life battery performance. *In situ* TEM has been used to provide insights into the mechanism of alloying anode materials.

Among various alloying electrodes, phosphorene-based electrodes provide the highest theoretical specific capacity (2596 mA h g^{-1}) for sodium storage with the formation of the Na_3P phase.[89] Therefore, mostly an *in situ* TEM study has been conducted to explore the Na storage mechanism in phosphorene.[89–92] Sun *et al.* demonstrated that the sodiation mechanism in black phosphorous consists of two steps, *i.e.* intercalation and alloying.[89] The intercalation reaction can take place only in channels along the *X*-axis because they are wide enough (3.08 Å) compared with *Y*-axis channels (1.16 Å). It occurs in the potential range from 0.54 V to 1.5 V between the layers of phosphorene with the generation of the $Na_{0.17}P$ phase. Below 0.54 V, Na ions were inserted due to the alloying mechanism to form an amorphous Na_3P phase, which was mainly responsible for the excellent gravimetric capacity of black phosphorus. Nevertheless, the alloying reaction resulted in a huge theoretical volume expansion of 500%, which led to

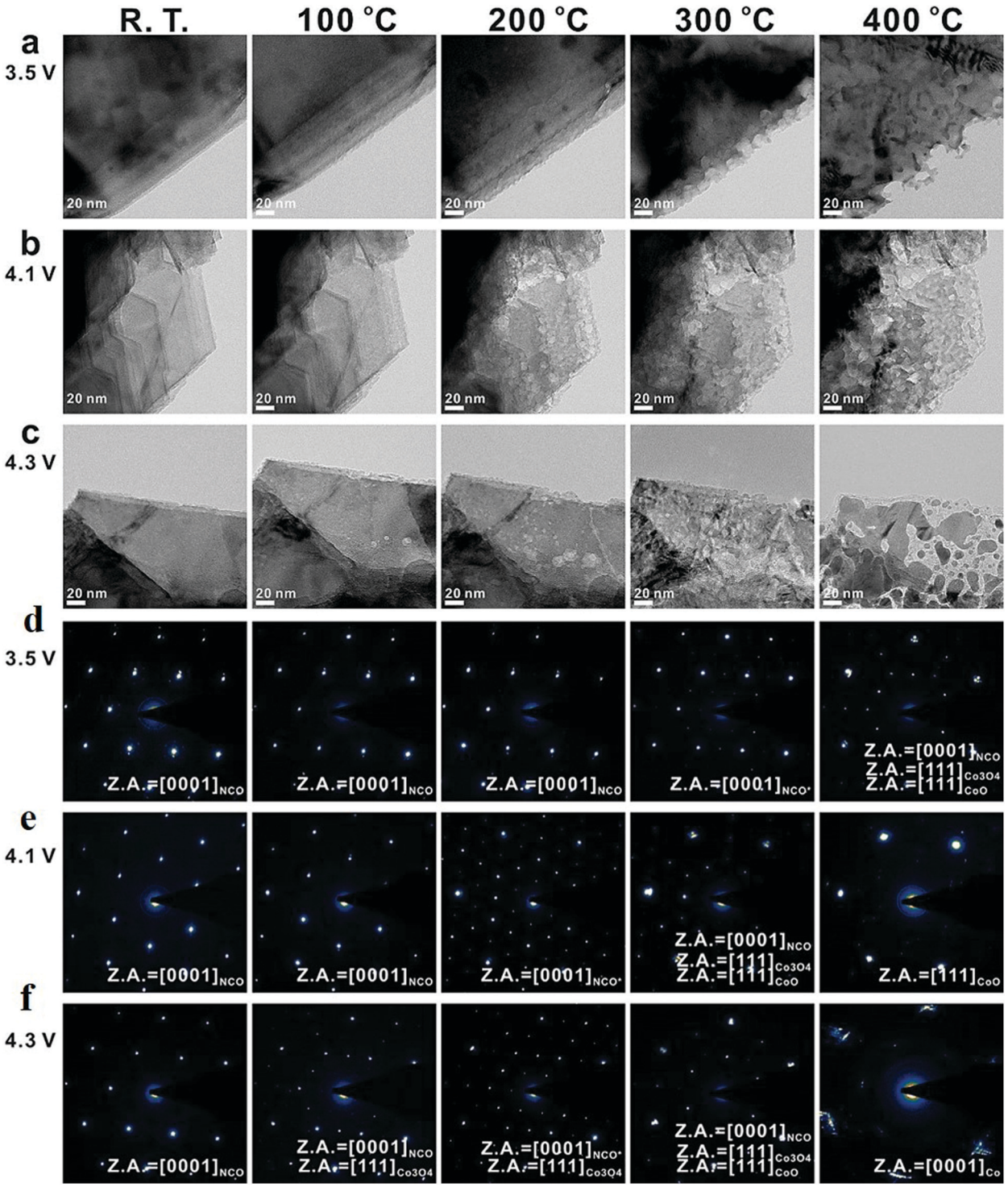

Fig. 4 (a–c) *In situ* bright field micrographs of the surface of Na_xCoO_2 cathode charged to: (a) 3.5 V, (b) 4.1 V, (c) 4.3 V during heating. (d–f) *In situ* EDP from the Na_xCoO_2 cathode's surface charged to: (d) 3.5 V, (e) 4.1 V, (f) 4.3 V during heating. Reproduced with permission.[45] Copyright 2017, American Chemical Society.

structural and mechanical degradation and capacity fading (Fig. 5a).[89] However, the reported volume expansion in black phosphorus along the *Y*-axis was 92%, and no changes were observed along the *X*-axis (Fig. 5b–d). The anisotropic volume variation along the *Y*-axis is due to the poor P–P bonding and fast diffusion of Na ions along the *X*-axis. But black P with complete sodiation producing Na_3P exhibited a theoretical expansion of 500%. Thus, it can be concluded that a huge volume expansion along the *Z* direction also occurred. These challenges prompted by *in situ* TEM, *i.e.* the nature of strains

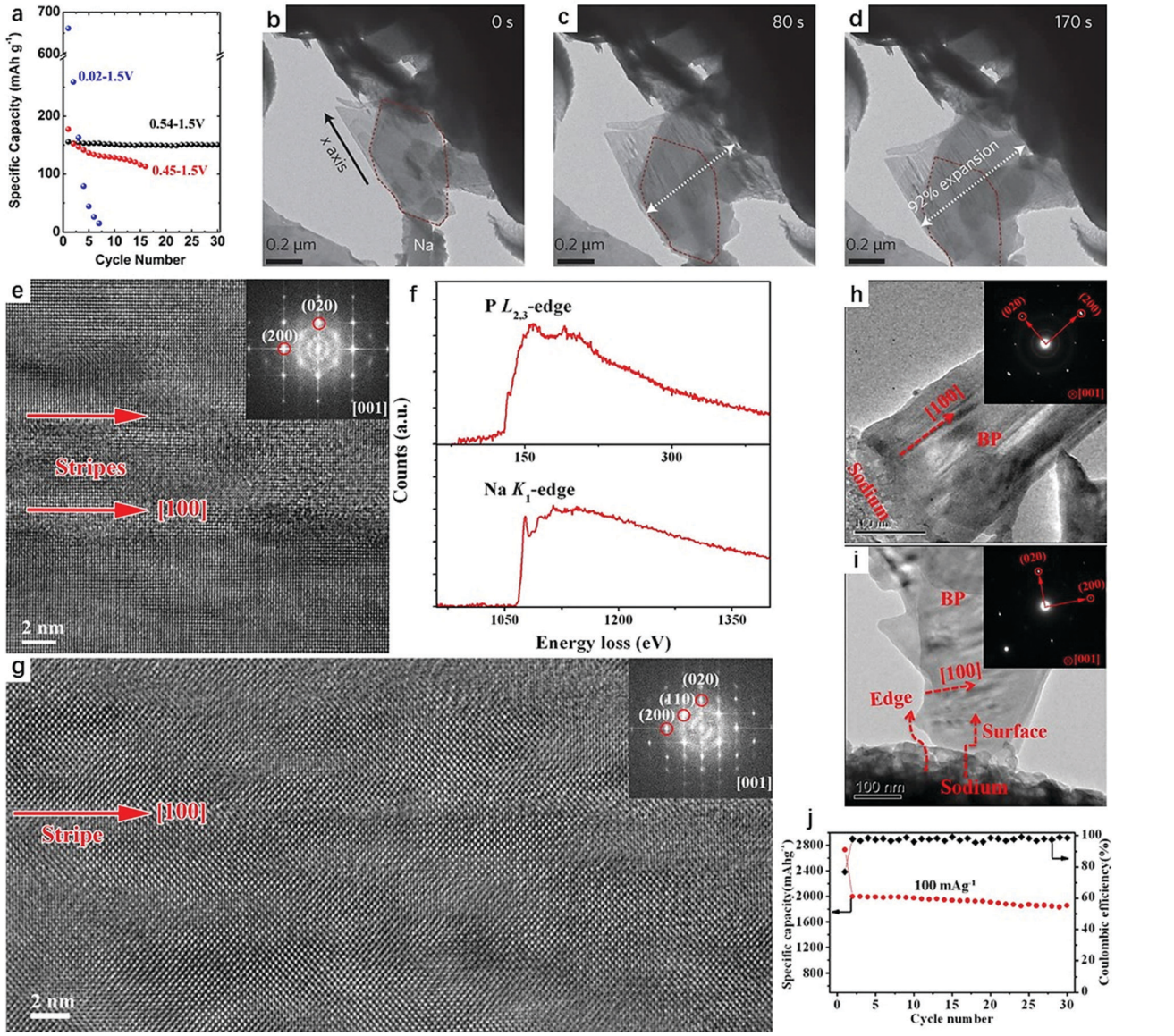

Fig. 5 Alloying mechanisms and performance in phosphorous-based electrodes during sodiation. (a–d) Black phosphorus. (a) Desodiation capacity of the black phosphorus electrodes (b–d), time-lapse TEM images of sodiation in black phosphorus. Reproduced with permission.[89] Copyright 2015, Nature Publishing Group. (e–j) Sodium ion transport in few-layer and monolayer phosphorene. (e) HRTEM image of partially sodiated few-layer phosphorene viewed in the [001] direction. (f) EELS spectra collected at the stripe of partially sodiated monolayer phosphorene. (g) HRTEM image of partially sodiated phosphorene with the top view. (h and i) Sodium transport at different contacts with respect to the sodium source. (h) Contact interface normal to the [100] direction. (i) Contact interface parallel to the [100] direction. (j) Cycling performance of the phosphorene at 100 mA g^{-1}. Reproduced with permission.[90] Copyright 2016, American Chemical Society.

produced in black phosphorous, could be efficiently addressed by manufacturing novel materials and structural designs. One way is to synthesize the composites of phosphorene with graphene and prepare a sandwich-like structure. Another method is to reduce the thickness and layer width of the black phosphorus, *i.e.*, the formation of mono- or few-layer phosphorene. It might assist in minimizing the stress along the *Y*-axis and *Z*-axis and thereby improve the electrochemical performance; therefore, it is interesting to study their structural evolution during sodiation. The *in situ* TEM study revealed that fractures or cracks were not found in mono- or few-layer phosphorene during the electrochemical cycling process, but volume expansion was observed along with the generation of stripes.[90] These sodiation stripes were observed parallel to the lattice plane of (020), *i.e.* along the [100] direction, in both few-layer and single-layer phosphorene, suggesting that Na ion diffusion preferentially occurs along the [100] direction rather than in other directions (Fig. 5e–g). These sodiation stripes were also detected by electron energy loss spectroscopy (EELS) (Fig. 5f), demonstrating that the edge sites and surface also affected the Na ion diffusion, and Na ion transport occurred preferentially at the zigzag edge instead of the armchair of phosphorene (Fig. 5h and i). Compared to black phosphorus, no obvious capacity loss in phosphorene was found during

electrochemical cycling processes (1845 mA h g^{-1} capacity retention after 30 cycles at 100 mA g^{-1}), demonstrating better cycling performance in phosphorene (Fig. 5a and j).[90]

Besides phosphorene, other elemental anodes like Ge,[93] Sn,[94] and Sb[95] and intermetallic compounds such as SnSb,[96] β-SnSb,[97] and ZnSb[98] were also analyzed by *in situ* TEM wherein mechanical stress and Na alloying/de-alloying behaviors were exposed. For the Ge alloying anode, the crystalline Ge (c-Ge) works well as an anode for LIBs, but Na ions cannot be inserted into or extracted from c-Ge due to their high diffusion barrier.[93,99] However, after its conversion from the crystalline to an amorphous state, a-Ge can be hosted as an anode for SIBs.[93] Contrary to the lithiation of Ge nanowires which occurs through a "*surface into core*" process, sodiation occurs *via* a "*V-shaped*" Na diffusion front.[93] After complete sodiation, the $Na_{1.6}Ge$ phase was observed with a volume expansion of 300%. This volume expansion might be reduced by designing a dual protective conductive network or by making porous and hollow nanostructures of Ge such as yolk shell structures. In addition, pores were also observed in Ge nanowires after de-sodiation.[93] The reformation of pores in Ge nanowires during repeated sodiation/de-sodiation processes could retain their structural robustness/integrity in SIBs.[93] Tin (Sn) is also a very promising alloying anode material, which undergoes a two step reaction during sodium insertion.[94] The first sodiation step consisted of two-phase reactions with a moving phase boundary and the formation of an amorphous Na_2Sn phase corresponds to a volumetric expansion of 60%. The second step was a single-phase reaction to sequentially form amorphous Na_9Sn_4 and Na_3Sn, and crystalline $Na_{15}Sn_4$ phases with a total volume expansion of about 420% (Fig. 6A). This huge volume expansion has not produced any fractures or cracks during sodiation, indicating the accommodation of the large sodiation-induced stress and excellent reversible sodiation/de-sodiation reactions. This might be attributed to the reversible volume variation in the initial cycles and self-healing of the Sn electrode.[94] These discoveries shed light on the design of Sn-based electrodes for rechargeable batteries with enhanced capacities and cyclic stability.

A comparative *in situ* TEM study of sodiation and lithiation has also been carried out using various alloy type electrodes to demonstrate how Na and Li ions transport and behave in these electrodes.[98,100,101] For instance, sodium ion insertion behavior in Se was observed, which was entirely different from that during the lithiation process.[100] Se, being an alloying electrode, displayed a multi-step reaction mechanism for sodiation, *i.e.* sequentially transforming from Se to amorphous $Na_{0.5}Se$ and polycrystalline Na_2Se_2 and Na_2Se phases (Fig. 6B). The variation in the diameter of the Se nanotube was observed during the multistep sodiation. In the first step, the Se nanotube expanded from 135 nm to 170 nm with a 58% volume expansion, while in the second step it again expanded to 232 nm with a total volume expansion of 336% (Fig. 6B(a–f)). The lithiation of Se proceeded in one step, *i.e.* from Se to Li_2Se, with an 88% volume variation.[100] The overall sodiation process in Se involved amorphization, recrystallization and solid-state phase transformation (Fig. 6B(k)) and can be described using the following reactions:

$$Se + xNa^+ + xe^- \rightarrow Na_xSe \quad (1)$$

$$2Na_xSe + 2(1 - x)Na^+ + 2(1 - x)e^- \rightarrow Na_2Se_2 \quad (2)$$

$$Na_2Se_2 + 2Na^+ + 2e^- \rightarrow 2Na_2Se \quad (3)$$

Interestingly, sodiation was observed to be 4–5 times faster than lithiation, whereas the solid state amorphization reaction was 10 times higher compared with lithiation.[100] This can be ascribed to the high ionic diffusivity and electronic transport of the intermediate alloy phases (Na–Se) generated during the sodiation process. Similar behavior was also observed in the Zn_4Sb_3 alloying electrode.[98,101] The observed fast diffusion kinetics of Na ions than Li ions in these alloying electrodes may be attributed to the high conductivity and diffusivity of various phases evolved during the sodiation process.[98,101]

Thus it is demonstrated that SIBs have the potential to replace traditional LIBs, which can be understood using *in situ* characterization. Further, the information from *in situ* TEM will provide scientists with a comprehensive understanding of the alloying electrode electrochemistry and shed new light in designing and engineering advanced electrode battery materials with improved electrochemical kinetics and performance.

3.1.3. Reversibility of the conversion reaction and stability of the SEI. The conversion reaction involves the reduction/oxidation processes into nano-sized transition metal compounds (TMX, where TM denotes a transition metal, *e.g.*, Fe, Co, Ni, and Mn, and X can be an anion such as S, O, Se, and F) with evolution between the metallic state (TM^O) and NaX,[102–104] and can be generalized as follows:

$$TM_aX_b + (b{\cdot}n)Na + (b{\cdot}n)e \leftrightarrow aTM + bNa_nX \quad (4)$$

During conversion reactions, a large number of electrons are transferred per unit formula of the TMX (starting compound), thus resulting in a higher theoretical specific capacity compared with intercalation reactions.[102–104] Moreover, conversion reactions can be optimized to achieve a high capacity by selecting active materials with high valence oxidation states and low atomic mass.[24] The reversible Na storage *via* conversion reactions takes place mostly in nano-sized transition metal oxides, sulfides, selenides and fluorides. Despite the conversion reaction, the intercalation reaction may also be involved in these compounds comparatively at a higher voltage, but the charge storage capacity in these compounds is mostly dominant through conversion reactions. Therefore, these compounds are considered as conversion-type materials. Although high specific capacities have been shown by the conversion-type electrodes, many issues were encountered during each sodiation/de-sodiation process such as the evolution of the SEI layer, degradation of active materials, generation of new phases, poor initial CE, and irreversible Na conversion reaction.[104] These problems can be overcome by understanding the basic information about these reaction dynamics during the working of the battery using *in situ* TEM.

Taking into account the larger size of the Na ion than the Li ion, the behavior and characteristics of sodiation conversion

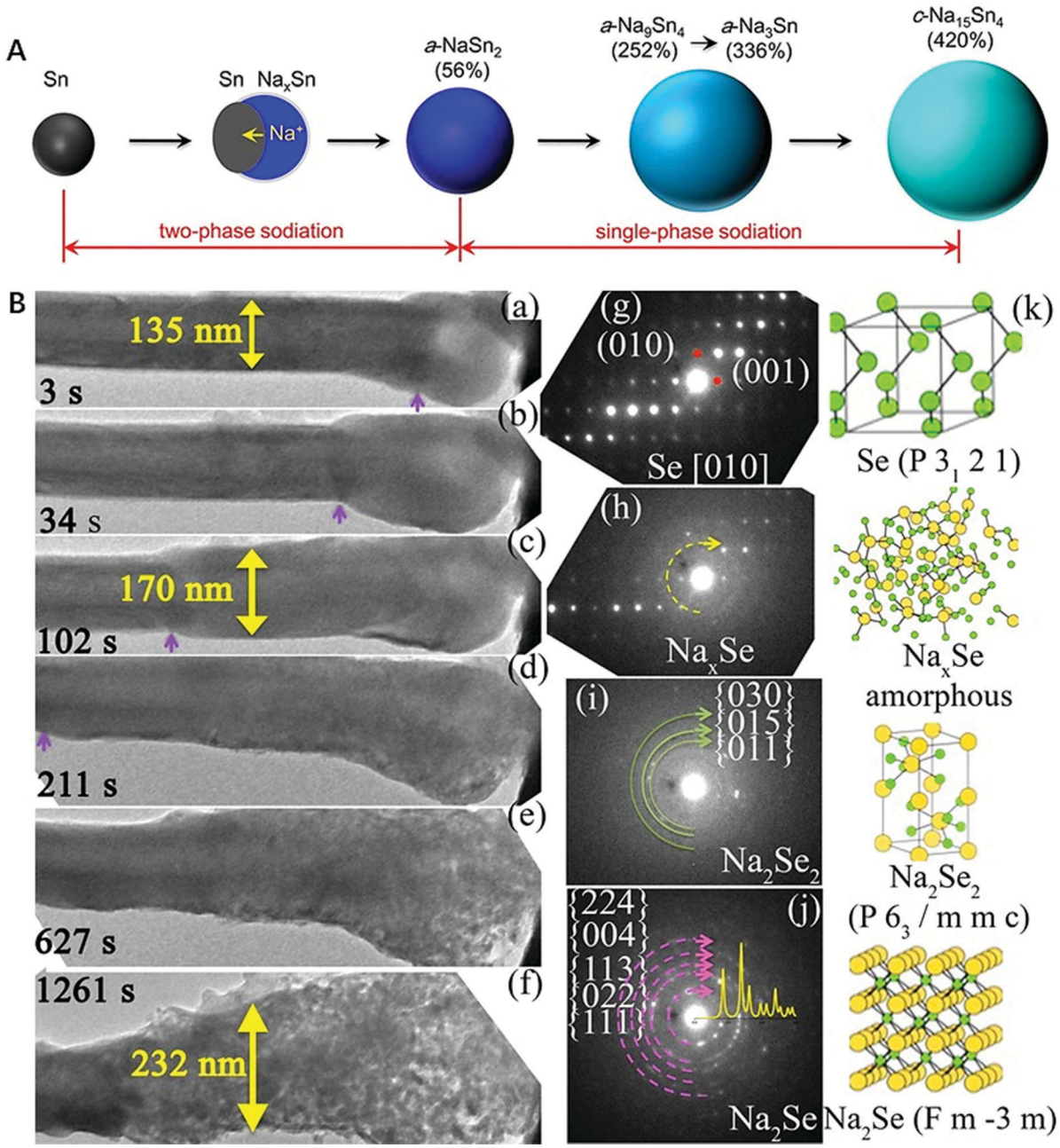

Fig. 6 Alloying reactions in various alloying electrodes: (A) schematic description of the structural evolution of Sn nanoparticles upon sodiation. Reproduced with permission.[94] Copyright 2012, American Chemical Society. (B) Reaction mechanism and phase transformation of the Se nanotube appearing in the sodiation process: (a–f) morphological evolution of the individual selenium nanotube and (g–j) evolution of EDP during the sodiation process. (k) Illustration of the atomic structures of Se during the sodiation process. Reproduced with permission.[100] Copyright 2016, American Chemical Society.

reactions are distinct from those of the intensively reported Li ions.[104–106] Therefore, the discoveries in real-time sodiation reactions involved in conversion type electrodes (including metal oxides, sulfides, and fluorides) are often compared with those of the *in situ* TEM study of lithium based electrochemistry. For instance, a comparative *in situ* TEM study of iron fluoride (FeF_2) shows that the morphology evolution is identical during lithiation and sodiation.[107,108] However, the conversion reaction of FeF_2 with lithium occurred in one step, whereas sodiation was a heterogeneous process which took place *via* a direct conversion reaction at the surface and a disproportionation reaction inside the FeF_2 nanoparticle core (Fig. 7A), which can be expressed as in eqn (5) and (6):[107]

$$FeF_2 + 2Na^+ + 2e^- \rightarrow 2NaF + Fe \quad (5)$$

$$FeF_2 + Na^+e^- \rightarrow 1/3Na_3FeF_6 + 2/3Fe \quad (6)$$

The generation of an interconnected conductive network of Fe nanocrystallites after the final sodiation of FeF_2 delivers excellent electronic conductivity. Besides, a comparative study of

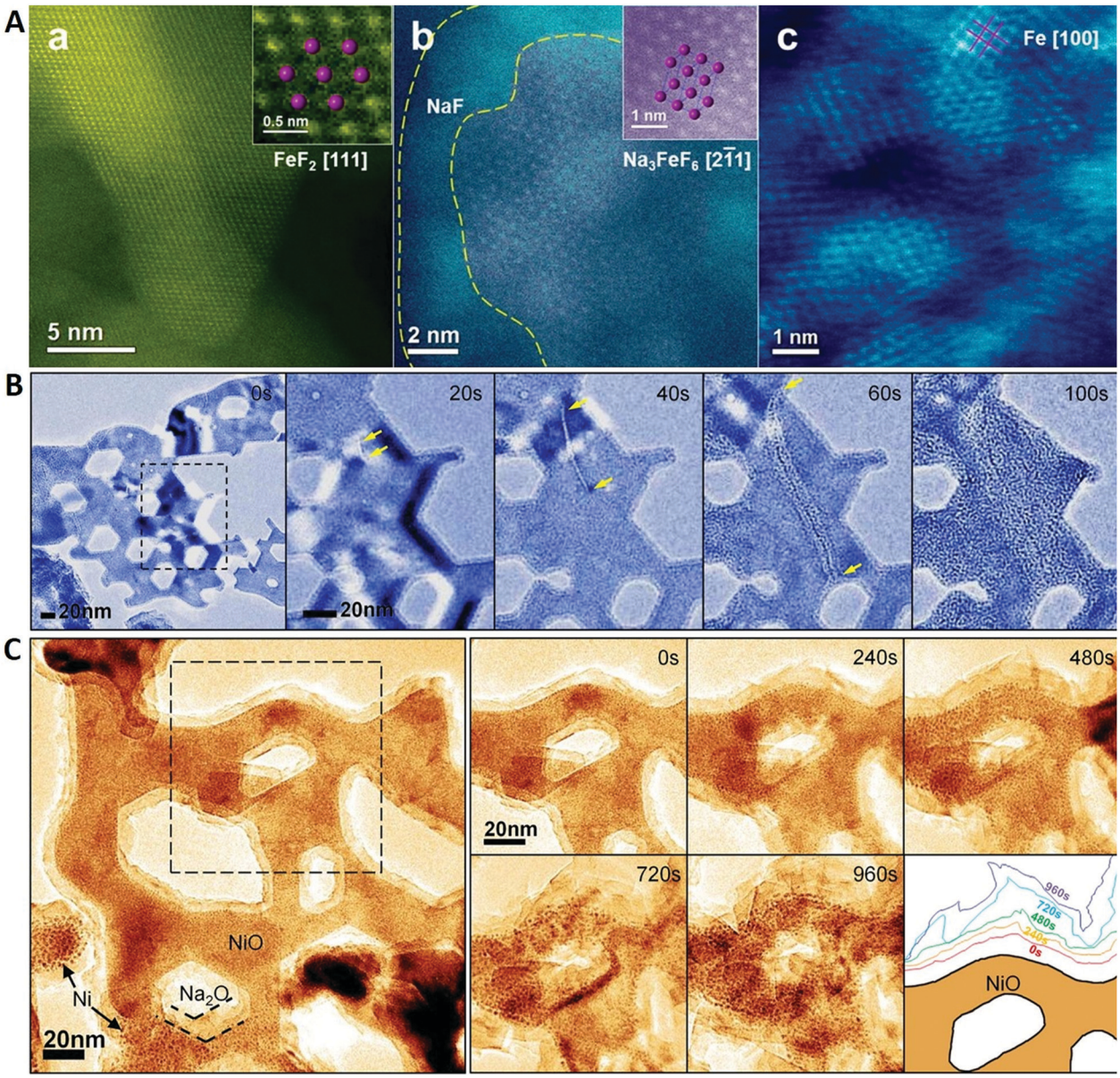

Fig. 7 Conversion reaction in various electrodes: (A) high-resolution scanning TEM (STEM) micrographs of FeF_2 showing (a) pristine FeF_2 nanoparticles, (b) crystalline Na_3FeF_6 phase and (c) interconnected Fe nanocrystallites in the sodiated particle. Reproduced with permission.[107] Copyright 2014, American Chemical Society. (B and C) Morphological evolution during *in situ* sodiation and lithiation in NiO: TEM imaging series captured in real time show morphological evolution during an *in situ* (B) sodiation, and (C) lithiation of NiO. Reproduced with permission.[110] Copyright 2015, American Chemical Society.

metal oxides also reveals a distinct charge storage mechanism for the Li and Na insertion processes. During the lithiation of NiO, firstly the Li ions diffused on the surface of NiO, followed by the conversion reaction through finger and shrinking-core modes (Fig. 7B).[109,110] However, the conversion reaction during sodiation proceeded through only the shrinking-core mode (Fig. 7C).[110] The conversion reaction *via* the finger mode is faster than that occurring through the shrinking-core mode. As a consequence, a slower sodiation reaction was observed in NiO than the lithiation. Moreover, during sodiation, a thicker passive layer (Na_2O with a grain size of ~4 nm) on NiO was observed than the passive layer during lithiation (Li_2O with a grain size of ~1 nm), which impeded more Na ions and decelerated their transport (Fig. 7B and C), resulting in slower sodiation than lithiation.[110]

Similarly, two phases of manganese oxides α-MnO_2 or α-MnO_3 underwent the same intercalation reaction with the insertion of both Li and Na ions, but distinct conversion reactions during lithiation/sodiation.[111,112] In the case of α-MnO_2, a reversible and stable phase transformation between the $Na_{0.5}MnO_2$ phase and the Mn_2O_3 phase was observed along with the fast degradation of tunnels during sodiation,[111] while a reversible conversion reaction between Mo and Na_2MoO_3 was observed for α-MnO_3.[112] Moreover, the structural/tunnel heterogeneity in MnO_2 significantly affects

the Na ion storage kinetics.[113] Similarly, different characteristics of conversion reactions have also been observed for other transition metal oxide based conversion materials such as CuO.[114,115]

In addition to metal oxides and fluorides, an *in situ* TEM study in metal sulfides was also carried out to understand the sodiation dynamics and morphological and structural evolution.[88,116–124] The sodiation behavior of metal sulfides may be distinct from that of lithiation based on their structures and the metal.[121] In the case of FeS_2 nanotubes (NT), a combination of intercalation and conversion mechanisms was reported (Fig. 8). During sodiation a reversible and stable phase transformation between the $NaFeS_2$ (different from lithiation where the reversible phase was $Li_{1.3}FeS_2$) and Na_2S + Fe phases was recognized.[32,117] However, a huge volume variation was observed, but it did not produce any fracture or pulverization in the FeS_2 NT during repeated cycles (Fig. 8a–g).[117] The excellent structural integrity and robustness of FeS_2 during the cycling process were attributed to the presence of plentiful micro-gaps of inter-nanoparticles within the FeS_2 NT that efficiently accommodates the huge volume expansion. These structural characteristics of 1D FeS_2 NT led to an excellent specific capacity of 360 mA h g^{-1} at 179 mA g^{-1} after 50 cycles which is much better than that of the commercial FeS_2 powder (Fig. 8i). Furthermore, the Cu_2S electrode also revealed distinct morphological evolution and nanoscale reaction pathways upon lithiation and sodiation.[121] Although large volume variations were found during the sodiation/de-sodiation process, excellent cyclic stability was exhibited by Cu_2S in SIBs. Therefore, substantial structural and morphological changes during sodiation in Cu_2S induced a new reaction pathway, but it may not essentially cause capacity fading.[121] Unlike other conversion type materials, layered type materials like SnS_2[116] and ReS_2[122] exhibit almost similar asymmetric reaction pathways during lithiation and sodiation. However, a large number of defects and dislocations were observed at the sodiation reaction front that were not seen during lithiation, which can be ascribed to the larger size of Na ions.[116] These *in situ* findings are important to understand the energy storage mechanisms in electrode materials and further improve the charge storage capacity and development of effective hybrid electrode materials.

3.1.4. *In situ* mechanical study in electrodes revealing both conversion and alloying reactions. Some metal oxides and sulfides materials store the charge *via* both conversion and alloying mechanisms, thus can be called as hybrid mechanism. For example, SnO_2 and ZnO undergo a conversion reaction along with alloying, resulting in a high specific capacity.[125–127] However, they face structural and mechanical degradation

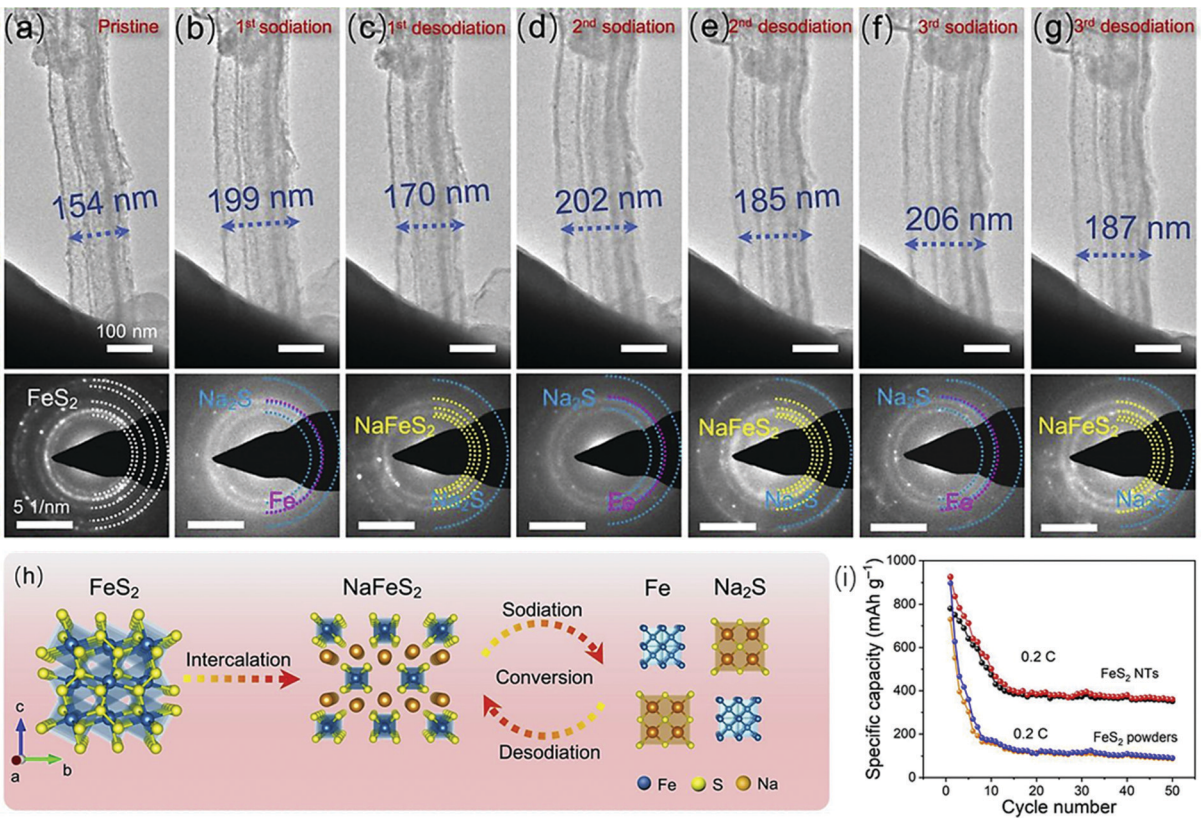

Fig. 8 (a–g) TEM images and corresponding ED patterns show morphological and structural evolutions during the first three cycles of sodiation/desodiation processes of a FeS_2 NT. The corresponding ED patterns are shown below. (h) Schematic illustration of the intercalation–conversion mechanism of the FeS_2 material. (i) Reversible charge/discharge capacities of FeS_2 NTs and FeS_2 powders at a current density of 0.2C (1C = 894 mA h g^{-1}). Reproduced with permission.[117] Copyright 2019, Elsevier Ltd.

during lithiation/sodiation, resulting in delamination of active materials, electrode cracking and higher impedance.[128] Moreover, voltage hysteresis due to incomplete phase recovery may also occur. Thus, it is of great significance to understand the underlying failure mechanism upon cycling, charge storage behavior and their comparison during lithiation and sodiation to develop their engineered structures. In the case of SnO_2, a two-step reaction took place during the first sodiation: (1) the displacement reaction with the generation of amorphous Na_xSn and Na_2O; (2) the alloying reaction in which Na_xSn was transformed into $Na_{15}Sn_4$.[126] A comparison between the Li and Na ion insertion revealed that the sodiation reaction (0.47 nm s^{-1}) is 20 times slower than the lithiation reaction (10 nm s^{-1}).[126,127] Also, the mechanical behavior during the lithiation and sodiation of SnO_2 showed a distinct behavior. It was revealed that during desodiation a large number of pores were observed, and they coalesced in the bulk of the electrode. This led to pulverization, cracking and higher electrical impedance in the electrode.[126] Comparatively, during the lithiation front, ample dislocation plasticity was formed in the electrode which made SnO_2 ductile without any fracture.[127] Therefore, the larger size of Na ions causes more mechanical degradation and capacity fading in the same materials upon cycling. However, this is not always the case. A correlation between the mechanical behavior and electrochemical cyclic stability in the ZnO electrode during lithiation and sodiation was also observed using *in situ* TEM.[129] The better cyclic stability in ZnO was observed during sodiation than lithiation. The formation of nanocracks and brittleness in ZnO during lithiation leads to electrode fracture and capacity fading (80% after 100 cycles), while sodiation results in plastic deformation and more ductility due to the presence of high-density dislocations in ZnO.[129]

The conversion/alloying reaction mechanisms have also been observed in metal sulfides.[130] For instance, during the initial stage of the first sodiation, Sb_2S_3 underwent an intercalation reaction at a very high reaction speed (146 nm s^{-1}). Upon further sodiation, the obtained intermediate amorphous $Na_xSb_2S_3$ phase transformed into Na_2S, Na_3Sb, and some traces of Sb *via* conversion and alloying reactions, whereas during de-sodiation Na ions were reversibly taken out from the nanocrystalline phases (Fig. 9a–c).[130] Such exceptional reaction behavior in the electrodes resulted in small volume variations (54%) and led to excellent performance.[130] Moreover, the effect of carbon coating on the reaction dynamics, morphology evolution and electrochemical performance were also studied, in which a faster sodiation reaction speed, a smaller volume expansion and better battery performance were observed in the case of carbon coated Sb_2S_3 compared with the uncoated one (Fig. 9d and e).[130] However, the original morphology of both electrodes remained well-preserved as no internal/external fractures or cracks were seen after full sodiation, suggesting its robust nature.[131] These *in situ* TEM findings elucidate the charge storage behavior of various electrode materials for SIBs. They also explain the morphological evolution, mechanical behavior and reaction dynamics, which therefore sheds light on a new perspective for designing and developing new electrode materials for SIBs.

3.2. *In situ* reaction dynamics in potassium ion and multivalent ion batteries

Just like SIBs, KIBs represent another attractive alternative to LIBs, but the *in situ* TEM study for electrode materials in KIBs is at the initial stage. Only a small number of reports have been published.[132–134] Due to the different ionic sizes of K than Li or Na ions, it is important to know how K ions behave electrochemically in the same materials as used for LIBs or SIBs. In the literature, most of the *in situ* TEM results for KIBs have been compared with those for LIBs and SIBs. In the case of CNF, the charge insertion mechanism and mechanical behavior have been illustrated to be similar for both SIBs and KIBs.[77] Upon complete sodiation/potassiation, a variation in the thickness of CNF walls was found.[77] This wall expansion in d-C was higher than that in c-C, suggesting the higher potassium and sodium storage capacity of the layers of d-C compared with that of c-C due to the presence of more defects in d-C than those in c-C.[77] It was also noticed that the expansion between the neighbouring graphitic layers (8.6%) was slightly larger compared with lithiation (7%) due to the larger sizes of Na and K ions.[33] In addition, interface fractures near the boundary of c-C/d-C of the CNF were also observed, which propagated in the axial direction upon sodiation/potassiation. Nonetheless, for KIBs, the cycling performance of the CNF anode was comparatively not good as in the case of NIBs, probably due to the relatively slow diffusion of larger K ions compared with that of Na ions. Besides intercalation, *in situ* reaction dynamics and microstructural evolution in alloying type materials have also been reported. Just like the sodiation of the Sn electrode,[94] potassiation of Sn underwent a two-step process with the formation of the KSn phase after complete reaction along with a 197% volume expansion, while reversible nanostructured pores were formed during de-potassiation.[134] However, just after a few cycles cracks and pulverization of Sn nanoparticles were observed, leading to mechanical degradation of electrodes and capacity fading. In another *in situ* TEM study, a small volume expansion (26%) was reported in red phosphorous (P) embedded into the nitrogen-doped porous hollow CNF (red P@N-PHCNFs) electrode during complete potassiation, indicating robust structural integrity of the electrode, *i.e.* without any fracture or cracking.[135] This volume expansion is much smaller compared with the volume expansion of other alloying based electrodes.[24,134] Generally, the mechanical degradation and cracking/fracture have been observed in the electrode materials during the electrochemical reaction of larger alkali ions (Na and K) compared with Li. But a different behavior was reported during the *in situ* electrochemical reaction of $FeSe_2$.[136] Although a smaller volume expansion occurred during lithiation compared to the reaction with Na or K ions, fractures were observed only during lithiation (Fig. 10A).[136] This is contradictory, because cracking, greater stresses and larger mechanical degradation are associated with larger volume variations. This unusual behavior may be attributed to two main reasons: (1) different mechanical stress evolution of the two-phase reaction front shape during the electrochemical

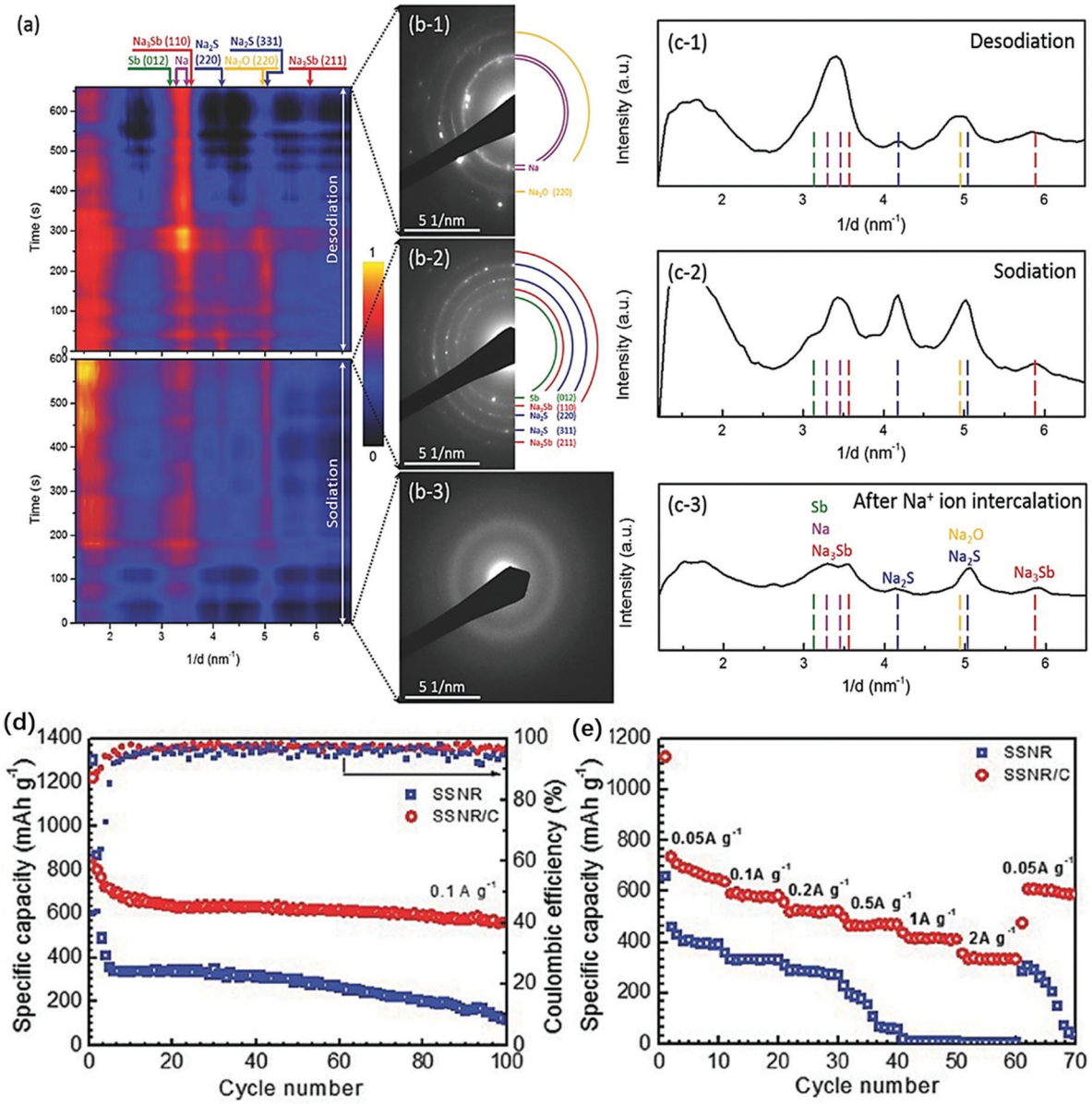

Fig. 9 Phase evolution during the first sodiation and desodiation processes of carbon-coated Sb_2S_3 nanorods probed by *in situ* electron diffraction. (a) Colored intensity profiles as a function of reaction time for the first sodiation and desodiation processes. (b) SAED patterns for (b-3) Na^+ ion intercalated, (b-2) sodiated, and (b-1) de-sodiated states. (c) Corresponding radially integrated intensity profiles of electron diffraction at (c-3) Na^+ ion intercalated, (c-2) sodiated, and (c-1) de-sodiated states. Comparison of (d) cycling performance and (e) rate capacities between carbon-coated Sb_2S_3 and uncoated. Reproduced with permission.[130] Copyright 2017, WILEY-VCH Verlag GmbH & Co. KGaA, Weinheim.

reaction of different alkali metal ions; (2) the unique mechanical behavior upon lithiation which results in cracking.[136] These *in situ* TEM findings reveal that electrode materials with larger volume variations can alleviate the mechanical stresses and degradation and may improve the cyclic stability for KIBs or NIBs.

Besides single ions (Na and K ions), batteries based on multivalent ions including Ca^{2+}, Mg^{2+} and Al^{3+} can be next-generation energy storage systems due to their high energy density.[137,138] However, the *in situ* TEM study on the electrode materials for multi-ion batteries is also at the preliminary stage. WO_3 is a conversion type electrode material and the *in situ* TEM investigation demonstrated that Ca^+ was first intercalated into WO_3 with the formation of an amorphous Ca_xWO_3 phase and then converted into W metal and CaO through a conversion process (Fig. 10B).[139] But, due to the low Ca^{2+} ion diffusivity in WO_3, the conversion reaction continued for *ca.* 2 nm into the single crystalline WO_3 film in the TEM. Co_3O_4 is also a conversion type material and has been studied intensively as an anode material for LIBs.[140] Its insertion behavior with Mg^{2+} and Al^{3+} was also investigated using *in situ* TEM.[141] The Mg^{2+} diffusion or insertion process was very sluggish during charging with Mg and overall no obvious sign of a conversion reaction was observed. Instead, an Mg thin film on the electrode was detected just like the striping process.[141] On the contrary, the Al^{3+} diffusion process into Co_3O_4

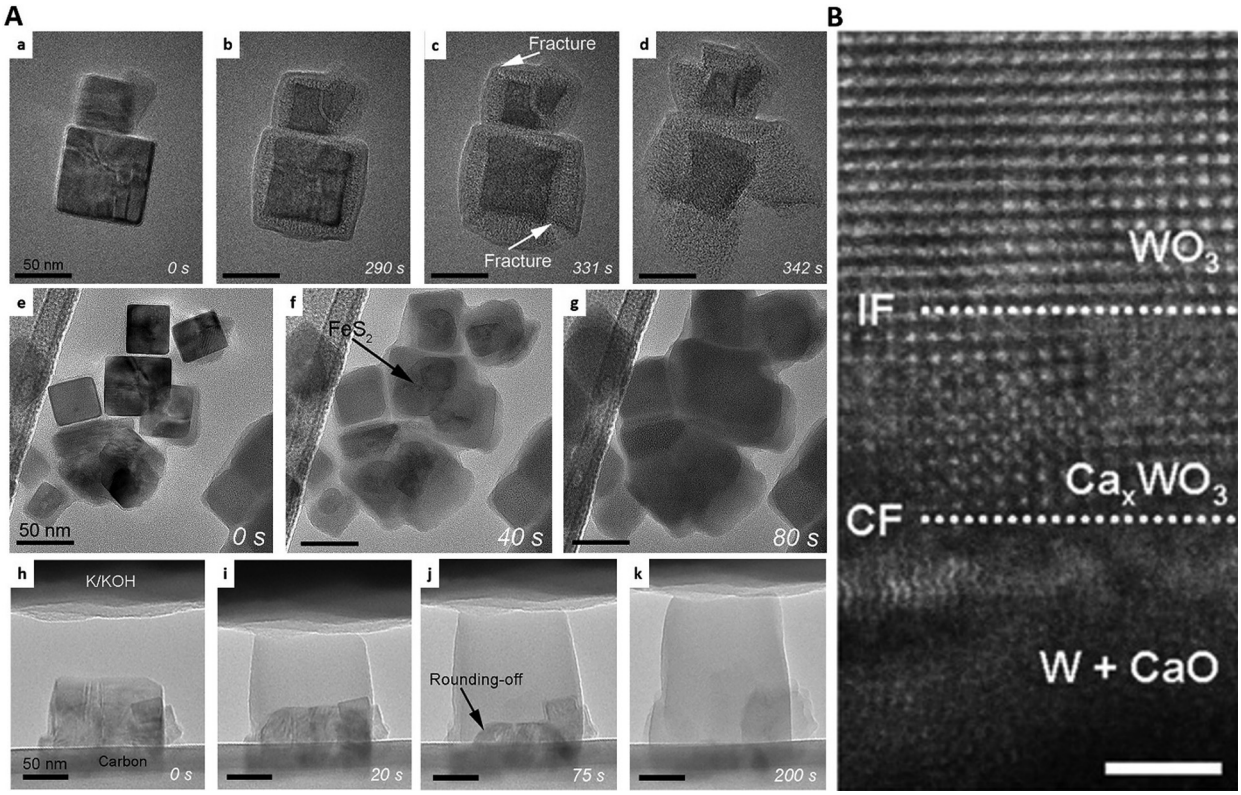

Fig. 10 *In situ* TEM study in various battery systems: (A) comparison of structural evolution among LIBs, NIBs and KIBs during the discharge process. (a–d) Snapshots of the lithiation of two FeS_2 nanoparticles. (e–g) Snapshots of the sodiation of a group of FeS_2 particles. (h–k) Snapshots of the potassiation of FeS_2. The scale bars are 50 nm. Reproduced with permission.[136] Copyright 2018, Elsevier Inc., Cell Press. (B) Atomic resolution high-angle annular dark-field in STEM (HAADF-STEM) image of WO_3 after Ca insertion. Scale bar, 2 nm. Reproduced with permission.[139] Copyright 2016, WILEY-VCH Verlag GmbH & Co. KGaA, Weinheim.

was even slower than the Mg^{2+} ion insertion process.[141] Such kinds of sluggish reaction kinetics are due to the large size of ions, high valence states and generation of solid state oxide films (MgO and Al_2O_3) that are inactive and covered over the surface of the electrode. These discoveries provide insights to understand the challenges regarding the reaction dynamics and behavior of multivalent ions (Ca^{2+}, Mg^{2+} and Al^{3+}) in the electrode materials.

In summary, the development of *in situ* TEM has led to a lot of discoveries and provided insights on the internal battery mechanisms of various electrode materials at the nanoscale for H-AIBs including SIBs, PIBs, and multi-ion batteries, and most of these findings are obtained using open cell solid state and *in situ* heating chip designs. In this section, we have summarized some of these discoveries including the reaction details of intercalation, conversion and alloying reaction mechanism during the charge/discharge process, absorption to intercalation mode mechanism in carbon based electrodes, transformations and propagation of the phase boundary, diffusivity of ions, nucleation of Na dendrites, selective ion transport in alloy type electrodes, and complex structural and phase evolution in conversion type electrodes. It is also found that when the same alloying and conversion type electrode materials for LIBs are used in SIBs and KIBs, they exhibit large volume variations (100–300%) upon insertion/extraction of ions, mechanical fracture and degradation of electrodes. However, some mechanisms for H-AIBs are still unknown such as the formation mechanism of the SEI layer. SEI is a distinct region between the active material and the electrolyte which generates and changes during the electrochemical process and is responsible for battery safety, CE, and battery performance. In *in situ* TEM history, considerable attention has been paid to the structural and morphological evolution of electrode materials for H-AIBs with little attention to the formation of a complex SEI layer, and there is still much which is not clear, particularly the structural evolution of the SEI during electrochemical processes, and how much and in what way it affects the battery performance, for example, how the SEI behaves toward electrode materials and evolves the morphology of active materials in solid state or liquid electrolyte. It is quite challenging to investigate the SEI evolution and its effect on active materials dynamically because the SEI is highly chemically reactive and very sensitive to an electron beam and cannot retain its original state. In this regard, cryo-TEM can be very attractive in which the SEI layer can be stabilized under cryogenic conditions and some investigations are reported to determine the atomic scale structure of the SEI layer of LIBs. However, no cryo-TEM study was reported yet for H-AIBs which can be a subject for future research. But cryo-TEM does not provide an in *operando* study; therefore, developing novel techniques that can provide a deep understanding of interphases and their role in rechargeable batteries can be a future research direction for electrochemists and microscopists.

Besides, most of these *in situ* TEM discoveries were obtained after one charge/discharge cycle, whereas real batteries are operated for many cycles and the SEI continuously evolves with cycling; therefore, it is quite difficult to understand the practical battery degradation mechanism that failed after many electrochemical cycles. Therefore, improved methods and techniques are required to understand the cell degradation mechanism. Another technical challenge for H-AIBs is the preparation of a sample holder which is made in a glove box and necessary precautions must be taken during the insertion of the sample holder into the microscope.

4. Real-time dynamic studies in Li–S batteries

Li–S batteries are attractive as next-generation rechargeable batteries due to their high theoretical specific capacity (1166 mA h g^{-1} based on Li_2S), high volumetric and gravimetric densities (2500 W h kg^{-1} and 2800 W h L^{-1}, respectively), low cost, non-toxicity and the high abundance of S.[142–144] Despite all these attractive characteristics, the currently reported practical performance (*i.e.* energy density and cycle life) of Li–S batteries cannot meet the theoretically estimated values.[11,20] This practical limitation is due to the insulating nature of active materials (sulfur), dissolution and shuttling effect of lithium polysulfides and inefficient usage of active materials.[11,20] To achieve this goal, it is essential to get insights into electrochemical reactions and degradation mechanisms. Being highly sensitive and used to directly visualize the morphology and microstructure evolution in electrodes, *in situ* TEM has been used to investigate the phase separation,[145] formation of polysulfides,[145,146] and self-discharge problems.[147] Notably, most of the *in situ* TEM investigations in Li–S batteries are carried out employing an open cell configuration using either SSEs or liquid ionic electrolytes. For instance, employing SSEs (Li_2O) in the open cell configuration, the real-time lithiation process of a sulfur cathode was investigated.[148] Here the diffusion of Li preferentially occurred at the surface of sulfur particles with the formation of a solid Li_2S layer on the bulk. The formation of the S_8/Li_2S interface during the lithiation process further inhibited the diffusion of Li ions into the sulfur bulk because of the insulating nature of Li_2S. This leads to an incomplete reduction of sulfur during the discharge process and results in capacity fading.[148] It is also noted that sulfur is sensitive to a high-energy electron beam due to the low vapor pressure of sulfur. Therefore, sulfur should be covered with an outer protective layer before being deployed in TEM.[23,149,150] In this regard, a carbon coating layer or MoS_2 flakes on the sulfur have been used as an effective method. In a typical study, initially the sulfur sample was distributed on the TEM grid and then encapsulated with a protective carbon layer of $\sim$5 nm thickness by sputtering (Fig. 11a).[145] In this design, the lithium source is not in direct contact with sulfur due to the protective carbon layer and inhibits the effects of an electron beam. As the lithiation reaction proceeded, the image contrast of sulfur became weaker due to the transformation of sulfur into Li_xS, which is attributed to the insulating nature of Li_xS (Fig. 11b and c). During the initial lithiation process, the S cathode partially transformed into polycrystalline S and Li_2S phases. As the lithiation proceeds further, the remnant S phase further transformed into Li_2S. Finally a pure Li_2S phase was obtained at the end of complete lithiation.[145] During the lithiation, the phase separation between the S and Li_2S at the nanoscale occurred (Fig. 11d–f), in which the first crystal S transformed into polycrystalline S and Li_2S phases, and finally to a pure Li_2S phase (Fig. 11g–i). This phase separation not only shortened the diffusion path but also created the interface network between the Li_2S and S phases. This interface network is beneficial for the fast diffusion and transport of electrons and Li ions during lithiation.[149]

Using SSEs, the direct transformation from the S to Li_2S phase, *i.e.* without any detectable intermediate lithium polysulfide (Li_2S_x, $4 \leq x \leq 8$) products, during lithiation was observed and confirmed by *in situ* TEM studies.[149,151] This direct transformation can be beneficial to the full use of the active material (S) in order to improve the electrochemical performance. On the contrary, a two-step reaction occurs during the lithiation of the sulfur cathode in a liquid Li–S battery. These findings provide an alternative way to address the incessant polysulfide shuttling effect in Li–S batteries.[144]

The real-time variation of volume in the active material during lithiation has also been monitored using *in situ* TEM studies. Moreover, the leakage or sublimation of the sulfur cathode during the lithiation process in TEM is a huge limitation for real-time structural characterization using TEM, which can be prevented by structural design of the cathode.[149,151,152] For instance, the *in situ* study of a porous carbon nanofiber (PCNF) electrode revealed that how optimized cathode design confined the lithiation product Li_2S within the electrode, accommodated the volume expansion (35%), and prevented the sulfur sublimation, whereas the carbon host (PCNF) remained unbroken without any detectable cracks (Fig. 12a–c).[151] These findings provide an insight on how the structural integrity of the electrode could be maintained.

In Li–S batteries, using a sulfur cathode has several technical challenges, namely, the loss of active material, volume variation, shuttle effect, and the solubility of lithium polysulfides which may degrade the electrochemical performance. In this regard, Li_2S (having a theoretical gravimetric capacity of 1166 mA h g^{-1}) is a prelithiated cathode material and has been considered an attractive alternative cathode material which can overcome the shortcomings of sulfur cathodes.[146,153–156] However, a deeper understanding of the structural change and electrochemical activation processes of the cathode (Li_2S) during real-time lithiation is also required. Few *in situ* TEM studies about Li_2S cathodes have been reported. The electrochemical activation of Li_2S occurred through the gradual dissolution of the generated lithium polysulfide in the ionic liquid electrolyte, resulting in capacity loss.[146] To further improve the electrochemical performance of Li_2S, encapsulation with a conductive matrix such as graphene or highly nitrated graphene over Li_2S has been proposed. The advantage of the conductive matrix onto Li_2S during battery operation was investigated using *in situ* TEM.

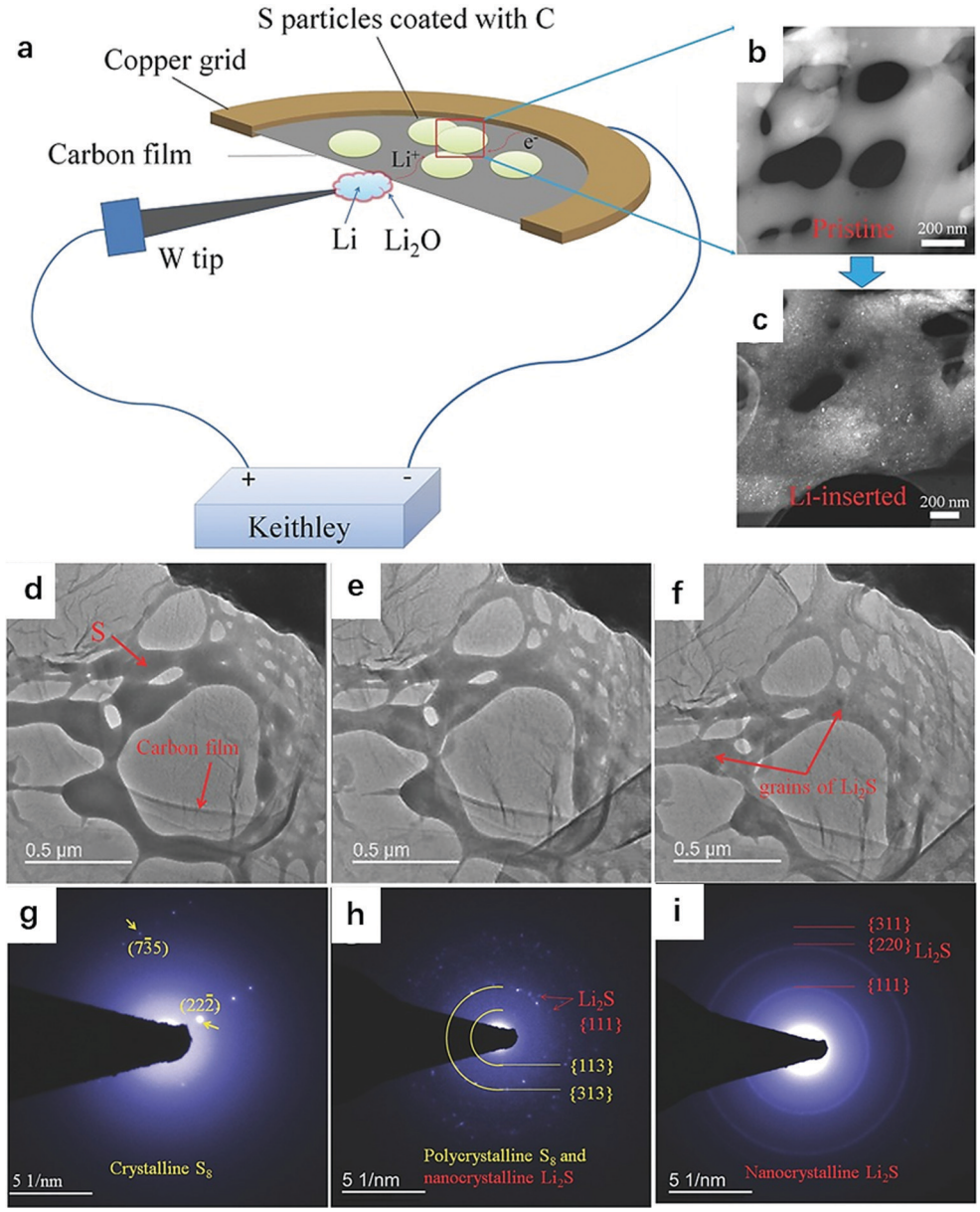

Fig. 11 (a) Schematic diagram of the electrochemical device setup for *in situ* TEM observation of the solid-state Li–S nanobattery. Typical annular dark-field-STEM (ADF-STEM) images of the S sample (b) before and (c) after lithiation. (d–i) Selected images of sample evolution during the lithiation process of S. (d) and (e and f) correspond to the images of the pristine sample and lithiated products, respectively. (d–f) TEM images captured from the video of the lithiation process and (g–i) their corresponding SAED patterns. Reproduced with permission.[145] Copyright 2016, Wiley-VCH.

A small volume change (10%) and no fracture in the Li_2S@graphene composite during lithiation/de-lithiation under *in situ* TEM were found,[156] indicating the high structural integrity of the cathode (Fig. 12d–j). Such electrode designs resulted in good cycling performance (440 mA h g^{-1} after 200 cycles at a 160 mA g^{-1} current density with a mass loading of 2 mg cm^{-2}) and rate capability (300 mA h g^{-1} at a current density of 2C) based on the full-cell system of Li_2S@graphene//graphite (Fig. 12k and l). However, in the case of pure Li_2S high structure vulnerability and pulverization during the charging/discharging process were observed, leading to severe electrode mass loss and decomposition, and consequently rapid capacity fading.

Using conventional TEM, the structural and chemical changes cannot be observed in beam sensitive and highly chemically reactive materials.[62] To obtain the reliable results of materials in TEM, the sample must not change its original state under the TEM conditions. But sulfur immediately sublimates and redistributes in the high vacuum condition of TEM, and therefore the results obtained from conventional TEM might be problematic, unreliable and misleading. The sulfur sublimation artifacts can be eliminated using cryo-TEM by suppressing the sublimation of sulfur at cryogenic temperatures and thus reliable results can be obtained at multiple length scales.[63] Using cryo-TEM, few studies have also been reported for

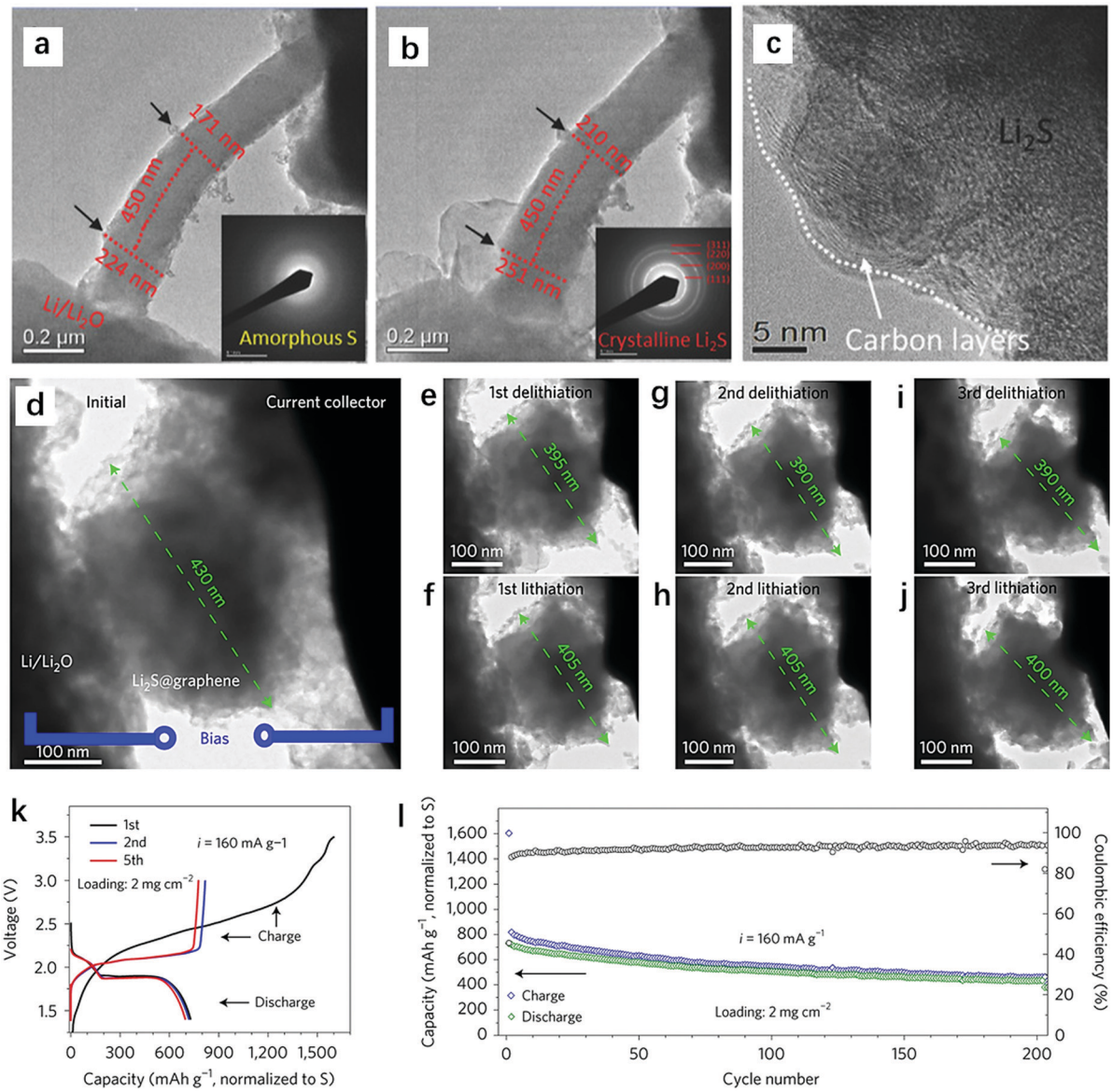

Fig. 12 TEM images and SAED patterns of (a) pristine and (b) fully lithiated PCNF/A550/S. (c) High resolution TEM image of lithiated PCNF/A550/S. Reproduced with permission.[151] Copyright 2017, WILEY-VCH Verlag GmbH & Co. KGaA, Weinheim. (d–j) *In situ* TEM observation of a Li_2S@graphene capsule under repetitive lithiation/de-lithiation cycling with an operating potential of 3 V. (d) indicates the initial TEM morphology of a Li_2S@graphene capsule. (e–j) TEM images of the capsule after different delithiation and lithiation cycles. (k) Voltage profiles and (l) cycling performance of the graphite//Li_2S@graphene cell at 160 mA g^{-1}. Reproduced with permission.[156] Copyright 2017, Nature Publishing Group.

rechargeable batteries. For illustration, the TiS_2 behavior in Li–S batteries was observed using cryo-TEM. It demonstrated that, instead of TiS_2, Li_xTiS_2 ($0 < x \leq 1$) adsorbed the polysulfides and catalytically decomposed Li_2S.[157]

The *in situ* findings demonstrate that TEM is a powerful technique to explore the reaction mechanisms, structural evolution and volume expansion in the cathode materials of Li–S batteries. It describes how outer protective layers including carbon, MoS_2 and nitrated graphene on sulfur or Li_2S cathodes can overcome the shortcomings (such as sublimation and volume expansion) of these cathodes. However, the *in situ* TEM study of Li–S batteries lacks maturity in comparison with LIBs, and many issues of Li–S batteries still need to be known, which cannot be observed by *in situ* TEM. These issues include a clear evaluation of the final discharge product, which is either Li_2S or Li_2S_2, and their full conversion back to S_8.[144] Moreover, the current *in situ* TEM technique gives information about one electrode (cathode or anode) or one phase (liquid or solid). Therefore, such systems or characterization techniques are more attractive because they can simultaneously visualize the structural evolution of sulfur, variation of polysulfides, reactions at the interfaces, and compositional or chemical changes in the electrolyte. This can be possible by combining various *in situ*/*operando* characterization approaches that can provide these details at the same time. However, such a study is not reported yet mainly

due to the complication in making the *in situ* cell design for such systems.

5. Real-time electrode behavior in alkali-metal oxygen batteries

AOBs (Li–O_2, Na–O_2, K–O_2) are powered by oxygen oxidation at the cathode and metal reduction at the anode,[13,158–161] and exhibit the highest theoretical energy densities among all of the rechargeable batteries, making them promising and ideal energy storage systems to fulfil the future energy storage demands.[12,162,163] However, to put these highly efficient energy systems into commercial applications, many technical challenges such as the formation mechanism of discharge products (metal peroxides, metal superoxides), a large overpotential in the oxygen reduction reaction (ORR) and oxygen evolution reaction (OER), and charge transport kinetics and sluggish kinetics in O_2 reduction need to be addressed.[13] Therefore the development of AOBs requires an in-depth understanding of the AOB reactions at the solid/liquid/gas interfaces. Insights into these reaction mechanisms have been obtained by advanced *in situ* TEM. The focus point of this section is to elaborate the basic insights into the reaction processes of AOBs (Li–O_2, Na–O_2, K–O_2) including the formation mechanism of the discharge product and its decomposition upon the charging process, and factors affecting the reaction mechanisms using *in situ* TEM studies.

5.1. Li–O_2 batteries

In Li–O_2 batteries the discharge product is Li_2O_2 which suffers from low electronic and ionic conductivities.[158] It is important to know how/where it is formed (*i.e.* at the electrode/Li_2O_2 interface or the electrolyte/Li_2O_2 interface) and how it is decomposed during the charging process. An early *in situ* TEM study used an all solid state configuration in vacuum and showed that the decomposition of Li_2O_2 in Li–O_2 batteries preferentially took place at the MWCNT/Li_2O_2 interface instead of the Li_2O_2/solid electrolyte interface at very high overpotentials (10 V *vs.* Li/Li^+).[48] Therefore, it was suggested that the high overpotential and decomposition of Li_2O_2 were attributed to the electron diffusion-limited charge kinetics contrary to ion conduction-limited ones.[48] Later, both the nucleation mechanism of Li_2O_2 during the discharge process and its decomposition during the charging process using a liquid cell in TEM were observed.[52] The oxidation of the discharge product (Li_2O_2) occurred at the Li_2O_2/current collector interface, indicating that electronic conductivity is the limiting factor analogous to Zheng's work.[48] Nevertheless, the discharge reaction nucleation of Li_2O_2 was observed at the reaction-product/electrolyte interface and limited by Li ion diffusivity, resulting in a large overpotential. Identical charge/discharge characteristics were also observed *via* liquid cell based *in situ* TEM studies.[50] Contrary to the growth of the discharge product at one place, the nucleation of Li_2O_2 was observed at two places:[164] (1) at the carbon electrode/electrolyte interfaces displaying Li ion diffusion-limited kinetics and (2) within the electrolyte environment showing that the presence of a non-faradaic disproportionation process of intermediate LiO_2 and Li_2O_2 and its kinetics were limited by O^{2-} ion diffusion (Fig. 13a).[164] Upon charging, Li_2O_2 at both places was decomposed gradually. From the full discharge diagram (Fig. 13a), it is clear that the discharge process occurred immediately after the biasing potential was applied to the

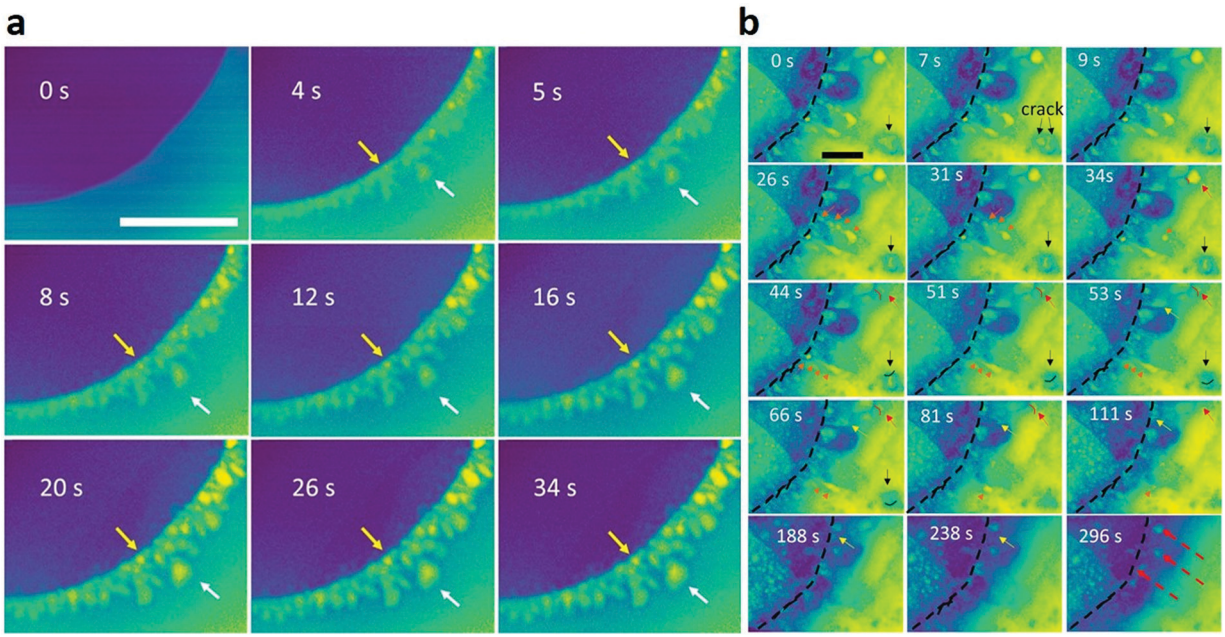

Fig. 13 (a) Time-sequential STEM images showing the full discharge process at the glassy carbon electrode. Scale bar: 5 μm. (b) Time-sequential STEM images showing the full charging process at the glassy carbon electrode.[164] Copyright 2018, Elsevier Ltd.

carbon working electrode and with the passage of the discharge process, Li_2O_2 at the interface and inside the electrolyte nucleated gradually and reached a size of 1 μm at 34 s. However, after 34 s, no changes in the shape or size of Li_2O_2 particles were observed, indicating the hindrance in Li^+ and O_2^- ion diffusion due to a continuous drop in electrolytes in the imaging area (Fig. 13a). Contrary to the instant growth of Li_2O_2 as in the discharge process, the decomposition of Li_2O_2 started approximately at 7 s. The decomposition of Li_2O_2 started at the electrode/Li_2O_2 interface instead of the electrolyte/Li_2O_2 interface (Fig. 13b) and was limited by electron conduction charge kinetics. Moreover, the inhomogeneous charge kinetics among various Li_2O_2 particles was found during the charging process. Similar conclusions were also reported in another study in which RuO_2 was used as a bifunctional catalyst towards ORR and OER.[53]

The morphology of the reaction products also affects the performance of Li–O_2 batteries. Using solid state batteries in aberration-corrected ETEM, the reaction pathways and product morphology evolution on the cathode surface were visualized.[57] ORR and OER presented reversible hollow spherical nanoparticles with Li_2O_2 and Li_2O inner and outer shells, respectively. These hollow spheres reversibly expanded and contracted on the CNT during the discharging and charging processes (Fig. 14a and b). Besides hollow spheres, a conformal coating layer, consisting of both Li_2O_2 and LiO_2, was also observed during the discharge process (Fig. 14c–e). Contrary to hollow spheres that decomposed completely upon the charging process, this conformal coating layer on the electrode surface (CNT) did not decompose or get removed completely, and a layer with a thickness of a few nanometers remained as a residue, which led to irreversible capacity loss.[57]

A deep understanding of the fundamental reaction mechanisms involving the discharge redox mediators may also assist in the further improvement of Li–O_2 batteries. Some attempts to investigate the ORR in real-time TEM by using redox mediators in the liquid cell have also been made.[49,51,165] The *in situ*

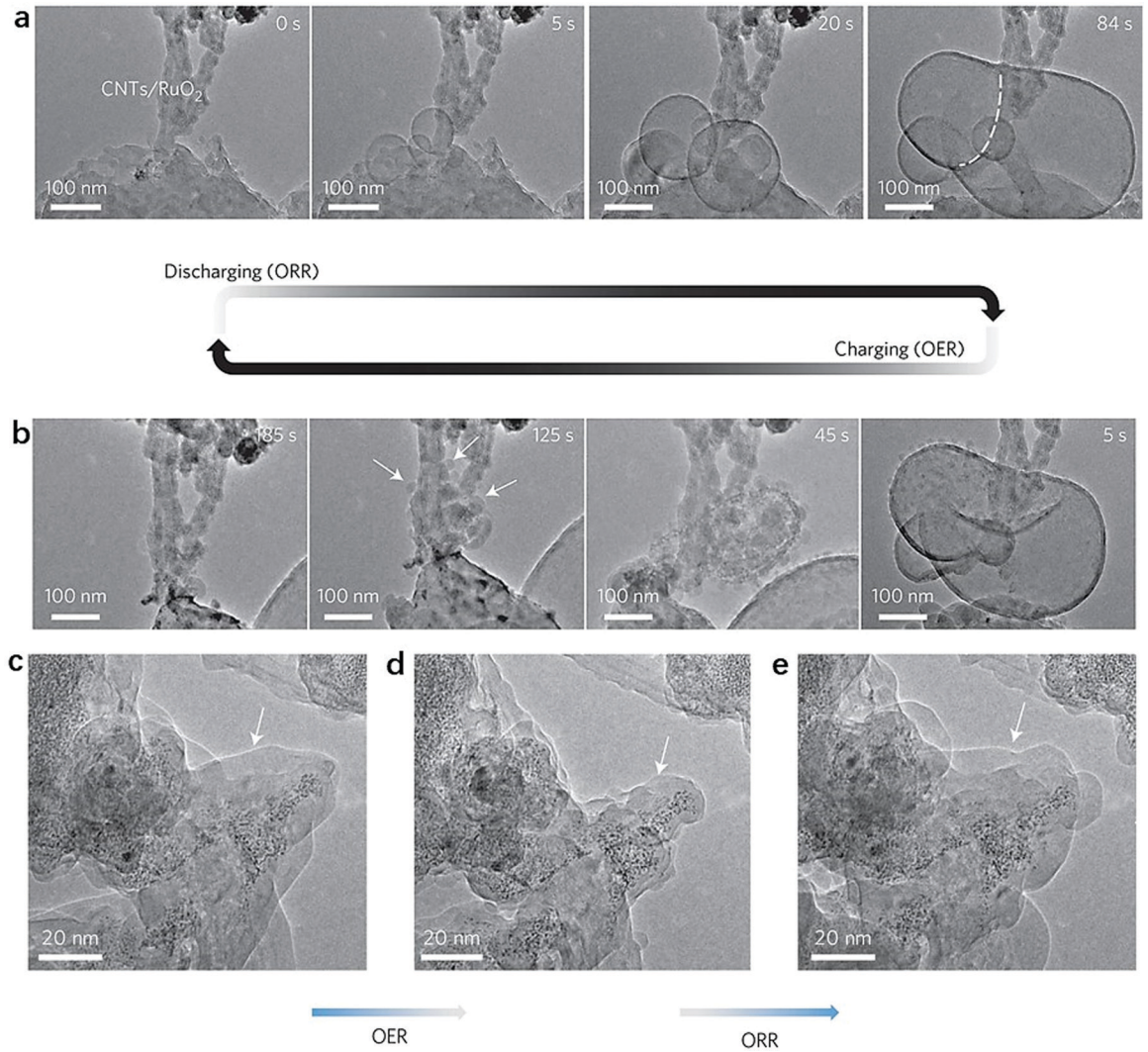

Fig. 14 *In situ* TEM observation of the morphological evolution of the discharge–charge products on the CNT cathode. (a) Time-resolved *in situ* TEM images show the nucleation and growth of hollow spherical particles during the discharging process and (b) charging process. (c–e) Conformal coatings of the discharging product. Reproduced with permission.[57] Copyright 2017, Nature Publishing Group.

reaction mechanism using 2,5-di-*tert*-butyl-1,4-benzoquinone (DBBQ) as the redox mediator was investigated as an example.[51] It was found that the discharge product Li_2O_2 formed in the solution instead of on the cathode surface involving the lateral growth of Li_2O_2 forming flat disc structures, followed by vertical growth along the peripheral area generating a toroidal structure like morphology. Recently, STEM observations revealed that the synergistic effect of the redox mediator tetrathiafulvalene (TTF) and the bifunctional solid catalyst RuO_2 improves the electrochemical performance of Li–O_2 batteries by lowering the overpotentials of ORR and OER.[165] These *in situ* findings pave a way for designing cathode catalysts and novel strategies for the development of highly energy efficient Li–O_2 batteries with good electrochemical performance.

5.2. Na–O_2 batteries

In contrast to Li–O_2 batteries, Na–O_2 batteries display some advantages such as better roundtrip energy efficiency, significantly low charging overpotential, better reversible decomposition of the discharge product, limited parasitic reactions and extremely low cost. However, it is still a subject of intensive research, and also the underlying mechanism is not completely understood.[166,167] Therefore, the mechanistic study of the discharge/charge process in Na–O_2 batteries using *in situ*/*operando* TEM is essential, providing new insights into the development of this technology. The *in situ* reaction mechanisms in Na–O_2 batteries have been studied in both solid and liquid based aprotic electrolytes. The first non-aqueous liquid electrolyte based Na–O_2 micro-battery to envision the on-site growth mechanism and dissolution of NaO_2 using *operando* TEM was reported in 2018.[54] It was suggested that the solution-mediated nucleation reaction was responsible for the generation of NaO_2 cubes with a size of ~500 nm during discharge, whereas the dissolution/oxidation of NaO_2 during the charging process also proceeded by a solution mechanism. It was also revealed that a porous shell with a thickness of ~200 nm at the NaO_2/electrolyte interface formed due to parasitic/side reaction (Fig. 15a), leading to low cyclic stability of Na–O_2 batteries. During the oxidation process, NaO_2 cubes decomposed gradually and concentrically (*i.e.* from outward to inward) at the cube/electrolyte interface, which leads to a stable decline in the size of NaO_2 cubes.[54] Besides, a solid-state Na–O_2 nanobattery was made using NaO_2 as a solid electrolyte to study the morphological evolution and electrochemical reaction mechanism of the discharge product during ORR and OER by *in situ* TEM (Fig. 15b and c).[60] The discharge product consisted of both cubic and conformal NaO_2. The huge cubic NaO_2 particles were reversibly generated and decomposed during the discharging/charging process, whereas conformal coatings were not fully oxidized during the charging

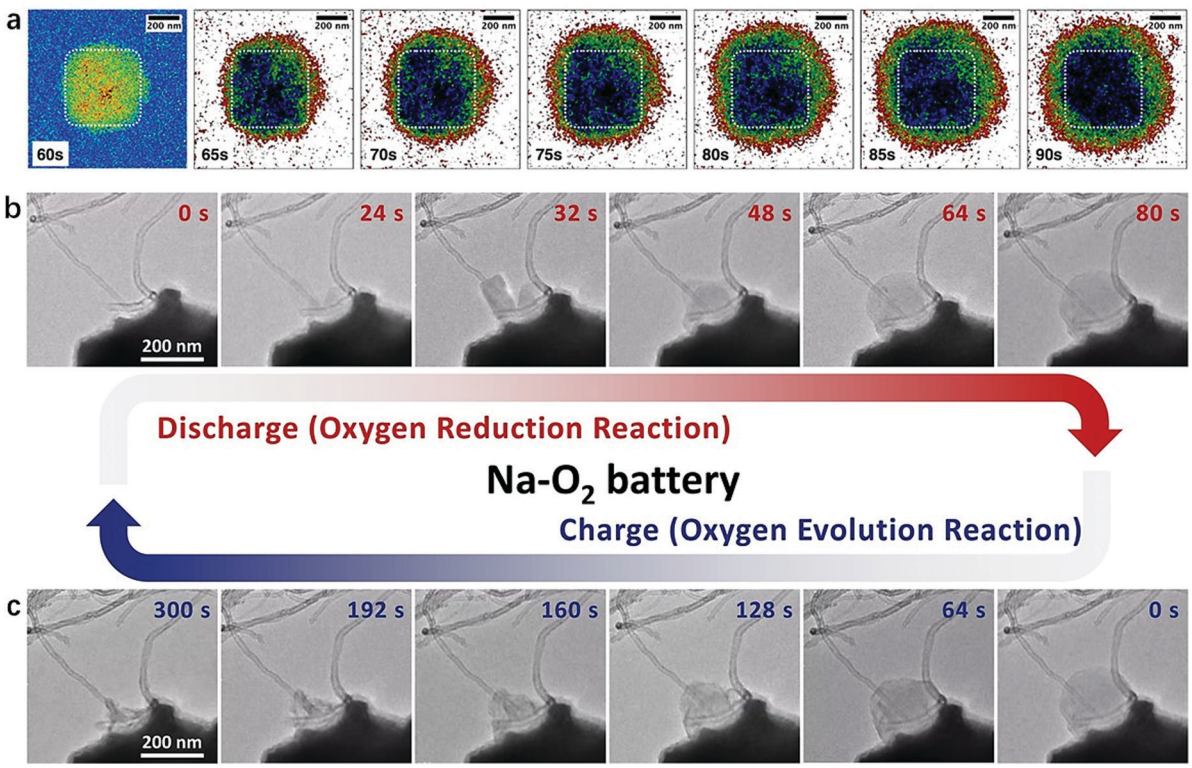

Fig. 15 (a) Fast and animated *operando* TEM images showing the evolution of the parasitic shell at the cube/electrolyte interface, indicated by the orange/green pixels. Reproduced with permission.[54] Copyright 2018, American Chemical Society. (b and c) *In situ* observation of the morphological evolution of the discharge/charge product using a Na–O_2 nanobattery in an ETEM chamber. (b) The time-resolved TEM images depicting the morphological evolution of the discharge product (ORR). (c) The images depict the morphological evolution upon charging (OER). Reproduced with permission.[60] Copyright 2018, American Chemical Society.

process, and the irreversible remnants formed on the electrode surface were a mixture of NaO_2 + Na_2O_2; however, their phase was maintained throughout the process. The same kind of behavior was also observed in Li–O_2 batteries.[57] In contrast to a liquid electrolyte, no side/parasitic reaction between the solid electrolyte and NaO_2 was observed, which has been a critical issue for the cyclic stability of batteries.

Unlike the cubic NaO_2 discharge product in Na–O_2 batteries using carbon based air cathodes,[54] mixtures of NaO_2 + Na_2O_2,[168] and Na_2O_2 + O_2[58,59,169] were detected using non-carbon based electrocatalysts, involving an extra disproportionation reaction during the discharging process. For example, Au-coated MnO_2 nanowires as electrocatalysts in a Na–O_2 battery and its oxygen chemistry during ORR and OER were studied (Fig. 16a),[58] which suggested that the nano-bubble like NaO_2 discharge product nucleated from Au with an 18% volume expansion on the surface of the MnO_2 nanowire during the ORR (Fig. 16b–e). With further discharge process, the NaO_2 rapidly disproportionated to Na_2O_2 and O_2, and resulted in the collapse of NaO_2 nanobubbles or cracks in NaO_2 (Fig. 16f–g). In the OER, the discharge product (Na_2O_2) electrochemically decomposed, but the decomposition of Na_2O_2 was partial with some particles existing on the surface of aggregated Au nanoparticles (Fig. 16h–j). However, no ORR occurred during the discharge process when a bare MnO_2 nanowire was used as the air cathode under similar experimental conditions to those in the case of Au coated MnO_2 nanowires; rather MnO_2 nanowires inflated 217% due to the intercalation of Na ions, indicating the inactive electrocatalytic activity of pure MnO_2 nanowires in a solid state Na–O_2 battery.[58]

Contrary to the one-step reaction,[58,168,169] the discharge process took place *via* a two-step reaction in the CuO air cathode.[59] The first one is a conversion reaction in which CuO transformed to Cu_2O and Cu. The second one involved multiple ORRs with the formation of the Na_2O discharge product, which was subsequently disproportionated to Na_2O_2 and O_2. However, the charging process could not completely oxidize or decompose the Na_2O_2 as observed in most of the solid state Na–O_2 batteries.[58,168,169] Moreover, when using non-carbon electrocatalysts, no carbonate generation was observed in the air cathode during battery cycling, and therefore this carbonate formation was the main factor affecting the battery performance.[59] The data obtained from the above real-time TEM studies suggest that highly efficient electrocatalysts are still required for the OER in solid state batteries to further decompose the discharge product Na_2O_2 in order to achieve better cyclability and reversibility, and a single electrocatalyst needs to be developed for both the ORR and OER, *i.e.* bifunctional catalysts, for which huge efforts have been made but still need more work to be done in the future.

5.3. K–O_2 batteries

K–O_2 batteries are another class of AOBs, which demonstrate good energy efficiency and a remarkable shelf life owing to the thermodynamically and kinetically stable discharge product KO_2.[170–173] However, understanding the formation mechanism of KO_2, which is the key to improve the performance of K–O_2 batteries, is at the initial stage. Until now, there is only one *in situ* TEM publication concerning the dynamic investigation of K–O_2 electrochemistry. Using single crystalline α-MnO_2 nanowires as electrocatalysts in solid state K–O_2 nanobatteries, the nucleation and growth mechanism of the discharge product KO_2 and structural evolution in α-MnO_2 during the ORR were

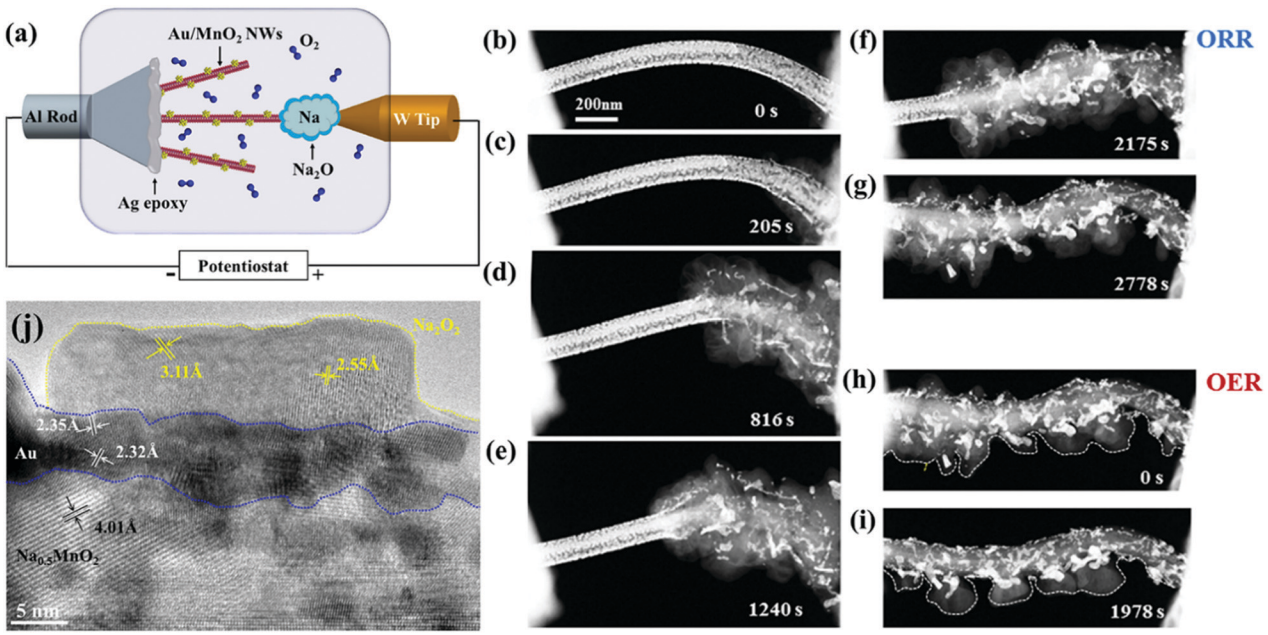

Fig. 16 *In situ* imaging of the Au-catalyzed ORR in a Na–O_2 nanobattery. (a) Schematic of the experimental setup of the Na–O_2 battery. (b–g) Structure evolution of the NaO_2 discharge product during ORR. (h–i) The charging process of the Au/MnO_2 NW (OER). (j) HRTEM image of the residue discharge products after the charging process. Reproduced with permission.[58] Copyright 2019, Elsevier Ltd.

investigated.[61] The discharge process occurred in two distinct reaction fronts in which MnO_2 was reduced to Mn_3O_4 and then to MnO with the formation of KO_2 as the reaction product and can be represented as follows (Fig. 17):

$$3MnO_2 + 4K^+ + 4e^- \rightarrow Mn_3O_4 + 2K_2O \quad (7)$$

$$Mn_3O_4 + 2K^+ + 2e^- \rightarrow 3MnO + K_2O \quad (8)$$

$$K^+ + e^- + O_2 \rightarrow KO_2 \quad (9)$$

Moreover, cracks and fractures were observed only in the 2nd reaction front (Fig. 17c and f). Contrary to other AOBs including Li–O_2 and Na–O_2, the discharge product KO_2 in K–O_2 batteries did not decompose into K_2O_2 as in other alkali oxygen batteries *via* the disproportionation reaction, which is an indication of the thermodynamic and kinetic stability of KO_2.[171,174,175] As reported in a previous study the ORR did not occur in Na–O_2 by using pure MnO_2 as the electrocatalyst,[58] indicating that the same catalyst cannot be functionalized in all AOBs.

The *in situ* findings shed light on many aspects of AOBs including how the discharge electrolyte environment affects the characteristics of the discharge product, what kind of factors (either electron diffusion-limited or ion conduction-limited charge kinetics) limit the kinetics in the discharge product during the growth and decomposition, sluggish charge/discharge kinetics, how various morphologies of the reaction products affect the performance of AOBs and how discharge redox mediators facilitate further improvement of AOBs. These findings significantly extend the knowledge and understanding of the underlying mechanisms at interfaces and assist in the development of novel methods to optimize the battery components such as air cathodes and offer novel insights into superoxide chemistry to improve the performance of AOBs. However, many issues are still unsolved and under discussion, for instance, how and what types of mechanisms are involved in the charging reaction, *i.e.* reaction intermediates and the origin of side reactions during charging. What is the role of cathode catalysts in the growth and decomposition of discharge products and how do these catalysts affect the ORR and OER? The development of a TEM technique that can examine the solid/liquid/gas interfaces at the same time may provide a deep understanding of these issues. ETEM has been used in AOBs; however, to get insights into solid/liquid/gas interfaces simultaneously, advanced differential pumping should be introduced in ETEM.

6. All solid-state batteries

ASSBs have been receiving wide attention for next-generation rechargeable batteries due to a high energy density, better

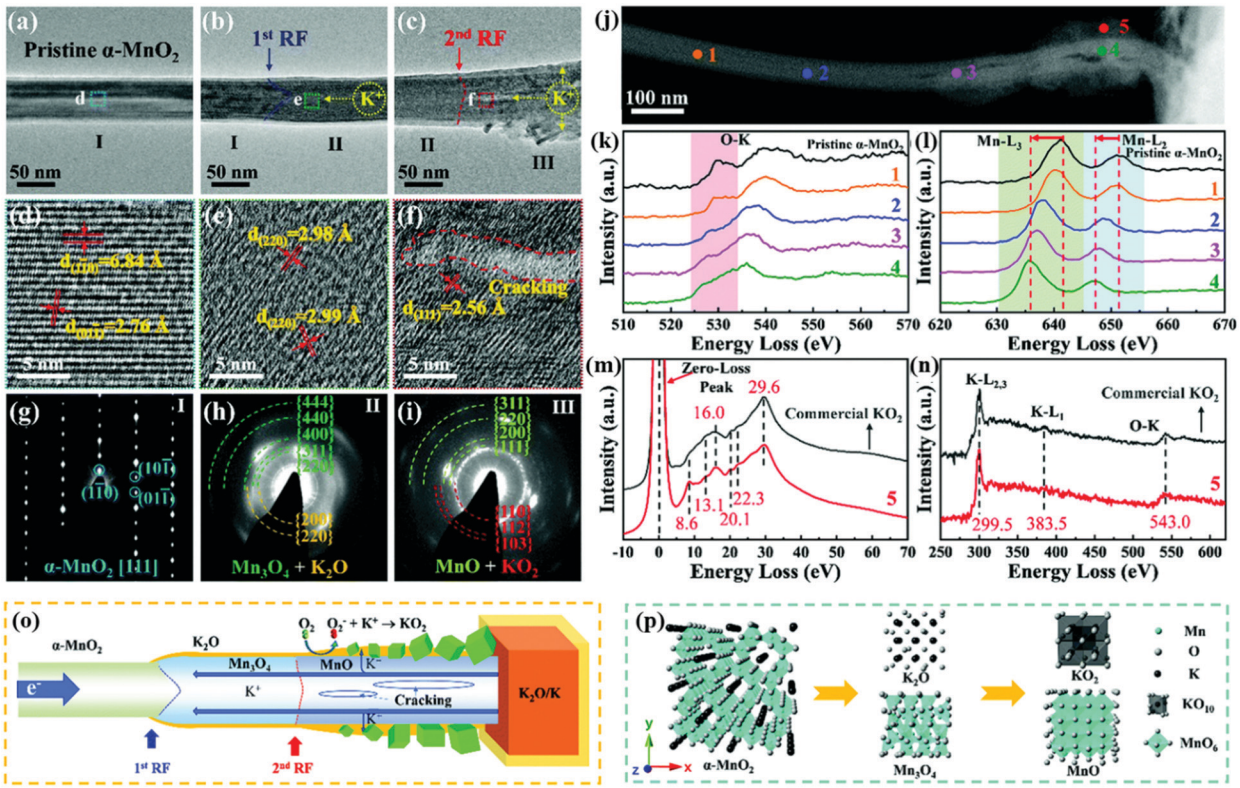

Fig. 17 Structural evolution and mechanism of the K–O_2 battery in an O_2 environment: (a–i) structural and phase characterization of an individual α-MnO_2 nanowire upon the discharge process: (a–c) two consecutive reaction fronts during discharging; (d–f) lattice-resolution structural evolution during potassiation; (g–i) EDPs collected from locations marked by "I", "II" and "III" in (a–c), respectively. (j–n) Arranged STEM-EELS data collected from the α-MnO_2 nanowire (black line) and potassiated nanowires in an O_2 environment. (o and p) Schematic illustration of the reaction mechanism of the ORR. Reproduced with permission.[61] Copyright 2019, The Royal Society of Chemistry.

battery packaging and superior safety compared with conventional LIBs.[18,176] In ASSBs inorganic/polymer SSEs are used instead of traditional organic liquid electrolytes, which are non-flammable, safer, and compatible with metallic Li anodes and also permits flexible configurations such as pliable and miniature batteries which are very important in wearable electronic devices.[177] However, currently numerous key issues such as understanding of interfaces and their evolution during the electrochemical process, the distribution and composition of species at the interface, interfacial potential distribution, and transport of ions are not well understood. It is quite difficult and challenging to detect the chemical species due to the elusive nature of the interface.[18,176] Moreover, ASSBs show high Li^+ transfer resistance at solid electrolyte/electrode interfaces, leading to a low power density.[178,179] Thus, advanced characterization is highly desirable to understand these key issues and electrochemistry of ASSBs. *In situ* TEM has been broadly used to examine the dynamic evolution of interfaces which gives information about the structure, morphology and elemental distribution, and provides an in-depth understanding of ionic diffusion kinetics and thus a critical aspect to improve the performance of ASSBs. In this section, we highlight the current progress made by *in situ* TEM of ASSBs with an emphasis on the direct visualization of reaction and deterioration in electrodes, SSEs and their interfaces.

6.1. *In situ* TEM observations at the electrode/solid–electrolyte interfaces

Over the past few years, great efforts have been devoted to examining the battery reaction occurring at the electrode/solid–electrolyte interface using TEM. The first cross sectional observation of ASSBs by TEM was reported by Brazier *et al.*;[38] however, this design faced critical issues in making real-time observations. These challenges include a loose contact between the electrode and electrolyte, a complicated process of the fabrication of the all-solid-state nanobattery, and rapid degradation of the interface due to the diffusion/migration of Li^+ ions. To date, planar solid-state battery, *in situ* heating chip, and individual nanowire based battery configurations have been suggested for the *in situ* TEM study of ASSBs. With running an individual nanowire battery in TEM, it was found that a thicker electrolyte ($\sim$180 nm) substantially reduced the self-discharge, while it was rapid with a thinner electrolyte ($\sim$110 nm), discovering thickness-sensitive self-discharge.[180] This was attributed to a short circuit caused by space-charge limited electronic conduction and gives useful information for the development of the 3D design of ASSBs.

Using the planar all solid state battery configuration in TEM, the 2D potential distribution produced by the diffusion of Li^+ ions at the LCO–cathode/solid–electrolyte interface was computed from electron holography, showing that the impedance was mainly concentrated near the electrode/electrolyte interface.[43] Within the similar planar battery configuration, a disordered interfacial thin layer between the cathode ($LiCoO_2$) and solid electrolyte (LiPON) interface without cycling was observed using *in situ* STEM.[44] Furthermore, upon the charging process, the interfacial layer evolved to form lithium oxides (Li_2O), lithium peroxides (Li_2O_2) and Co ion species, indicating that the chemical changes at the $LiCoO_2$/LiPON interface were responsible for interfacial impedance, instead of space charge effects. Later on, Nomura and co-workers discovered that Li ions were non-uniformly inserted/extracted during charge/discharge processes and an electrochemically inert layer consisting of a mixture of $LiCoO_2$ and Co_3O_4 was generated at the interface, resulting in high interfacial impedance for the Li ion transport.[181] Similar results were also reported in another study, in which the Li metal was accumulated near the cathode/electrolyte and at the anode current collector as well, indicating that the interfaces limit the diffusion of Li, which resulted in irreversible capacity fading.[182] Moreover, the direct visualization of Li ion diffusion at the atomic scale gives useful information for understanding the behavior of ions in batteries. The direct dynamics visualization showed that Li ions moved in the vertical and parallel directions of the electrode/solid–electrolyte interface, showing spatial variation of Li ions during the charging/discharging reactions (Fig. 18).[183] All the investigations discussed above are about the cathode/electrolyte interfaces, and the anode/electrolyte interface is also very critical in ASSBs.

To enable the use of the Li metal anode in ASSBs, it is very crucial to understand the chemistry, structure and formation mechanism of rarely existing interfaces between the anode and various solid-electrolytes. *In situ* TEM has also been widely used to examine the Li/SSE interface using a thin film solid state battery configuration. For instance, aberration-corrected *in situ* TEM is used to detect the structural and chemical evolution of an *in situ* generated Li/cubic-$Li_{7-3x}Al_xLa_3Zr_2O_{12}$ (c-LLZO) interface.[184] During contact against the Li anode, the surface of c-LLZO is reduced to a tetragonal LLZO interphase with a thickness of approximately five unit cells, which prevents further decomposition of c-LLZO with time while still maintaining the higher ionic conductivity. The Li phosphorus oxynitride (LiPON) kind of SSE has also shown high ionic conductivity and electrochemical stability with Li metal. Nevertheless, theoretical estimations reveal that LiPON may react with Li. The *in situ* TEM study revealed that a passive, electrochemically stable thin interface layer ($\sim$60 nm) with unique spatial distribution formed near the Li/LiPON interface upon contact with the Li metal. This valuable information gives a viewpoint for designing Li/SSE interfaces that can enable the use of the Li metal anodes in next-generation ASSBs. However, in many SSEs, the interfaces between the SSE and Li metal anode are not (electro)chemically stable, and thus an accurate understanding of interfacial transformations that are responsible for electrochemical deterioration is highly desired to stabilize the interfaces. The *in situ* TEM study reveals that the electro(chemical) reactions at the Li/$Li_{1.4}Al_{0.4}Ge_{1.6}(PO_4)_3$(LAGP) interface caused the volume expansion and amorphization which lead to the formation of cracks, mechanical stress and impedance, resulting in chemo-mechanical failure.[185] A similar kind of behavior was also discovered in the $Li_{1.3}Al_{0.3}Ti_{1.7}(PO_4)_3$(LATP) SSE during lithiation.[186] In these reports the enhanced electronic

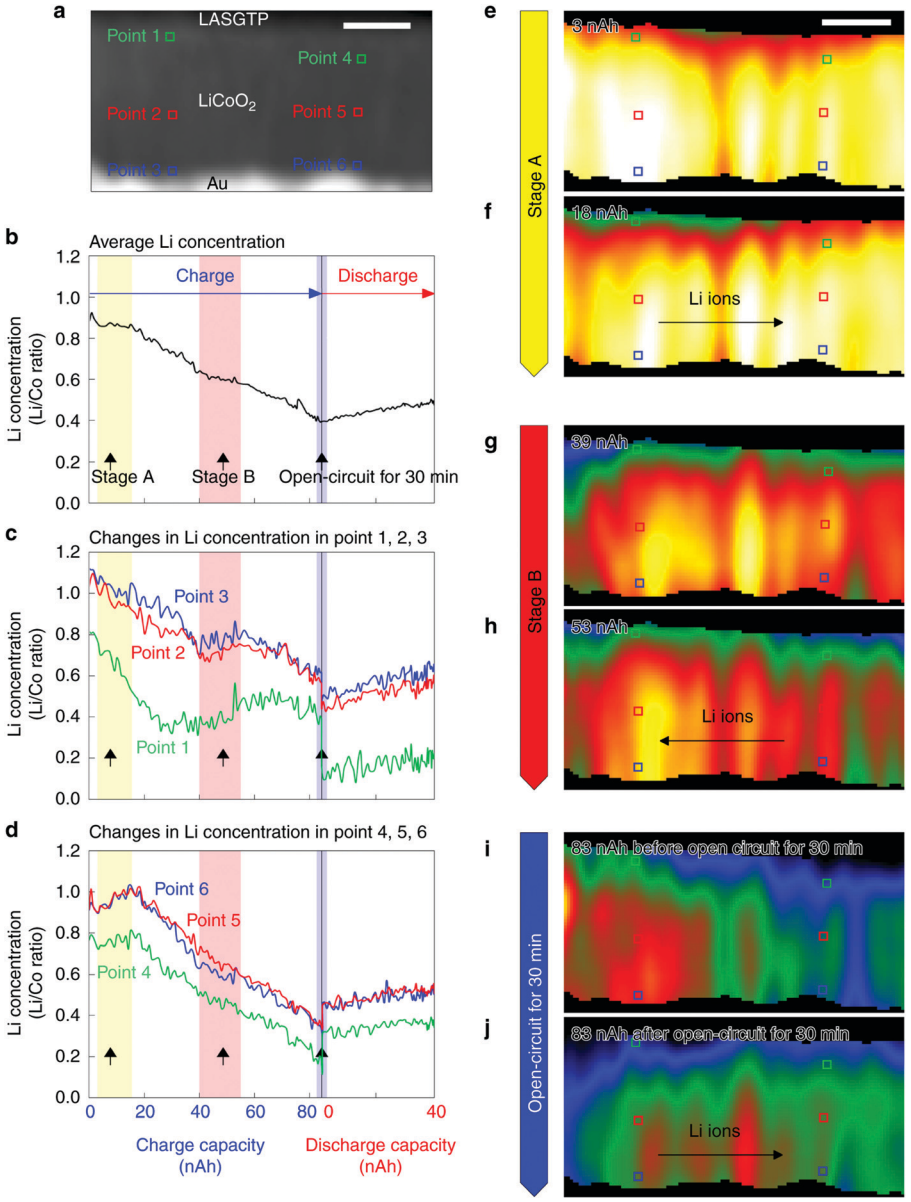

Fig. 18 Changes in the Li concentration at the atomic scale: (a) ADF-STEM image, (b) change in the average Li concentration in the entire cathode film in a. (c and d) Changes in the Li concentrations at points 1–3 and 4–6, respectively. (e–j) Changes in the Li maps at stages A (3–18 nA h), B (39–53 nA h), and C (open-circuit state for 30 min between the charge and discharge reactions), respectively. The scale bars in a and e are 100 nm. Reproduced with permission.[183] Copyright 2020, Nature Publishing Group.

conductivity at the Li/SSE interface is the main factor responsible for the continuous growth of the interphase.

In summary, the *in situ* TEM investigations on cathode/SEE and anode/SSE interfaces are highlighted. In cathode/SSE interfaces, the high interfacial impedance is the main reason for the poor electrochemical performance of ASSBs. *In situ* TEM discoveries reveal that this high interfacial resistance comes from the decomposition of the cathode which creates an ionic resistive region. The *in situ* information on anode/SSE interfaces demonstrates that the decomposition reactions at the Li/SSE interface are the major limiting factors in improving the performance of ASSBs. These findings demonstrate the significance of interfacial engineering in improving the cyclic stability, rate capability and reversibility of Li intercalation in ASSBs.

6.2. Investigating the *in situ* chemical/mechanical stability of SSEs

SSE is a key component of ASSBs, and the development of SSEs is vital for realizing ASSBs.[18,176] Among various SSEs, $Li_7La_3Zr_2O_{12}$ (LLZO) with a cubic phase is the most promising due to its high Li^+ ion conductivity and negligible electron transport, and because it is highly chemically/mechanically stable against the Li metal. The direct visual evidence of LLZO compatibility with Li metal was shown by an *in situ* biasing cell using STEM,[187] in which LLZO was observed to maintain the

original morphology, and no fracture/distortion or phase change could be identified during the Li ion transport process, showing the superior chemical/mechanical stability of LLZO *versus* Li metal.[187] However, a high temperature (>1100 °C) is required to synthesize the cubic LLZO phase; interestingly, this tetragonal-to-cubic phase transformation temperature (from >1100 °C to 900 °C) can be reduced by doping with Ga. However, it is important to understand the fundamental reaction paths and microstructure evolution during the synthesis of Ga–LLZO. The first experiment to observe the real-time microstructure evolution for the growth of Ga–LLZO at the atomic scale was reported by Huang *et al.*,[188] wherein the intermediate product LZO was first generated at 750 °C and then directly transformed to cubic Ga–LLZO *via* a layer-by-layer diffusion process at 900 °C, indicating that Ga doping significantly decreases the synthesis temperature. They also concluded that the doping of Ga occurred during conversion from LZO to LLZO, instead of at the start of the reaction, thus skipping the formation of the unwanted tetragonal intermediate phase. This effort provides a new method to investigate the structural evolution of SSEs during synthesis, thus providing a useful guideline for the development of SSEs. Besides LLZO, there are various ceramic SSEs like $Li_{1.3}Al_{0.3}Ti_{1.7}(PO_4)_3$ (LATP) which are also light, cheaper and highly conductive, but not stable with the Li anode. It can be stabilized by coating with an interfacial layer such as boron nitride (BN) which is chemically inert, mechanically robust, and ionically conductive; however, it is difficult to detect the interfacial evolution. By means of *in situ* TEM, it was reported that no phase change in LAPT/BN was observed after reacting with the Li metal, indicating good structural and chemical stability; however, bare LAPT transformed to an amorphous structure with the formation of $Li_3Al_{0.3}Ti_{1.7}(PO_4)_3$, showing the reduction of LATP after lithiation.[189] These *in situ* TEM results revealed that a 5–10 nm thick BN film is adequate to resist the reduction of LATP by the Li metal, and this strategy could be extended to other non-stable SSEs.

6.3. *In situ* TEM study of electrodes for ASSBs

The development of high-capacity electrode materials for ASSBs is facing critical issues (such as structural degradation, the formation of various defects, and Li dendrite formation) which requires an understanding of the dynamic process, fundamental mechanisms and structural evolution during electrochemical reactions. In the past few years, tremendous efforts have been devoted to developing electrode materials for ASSBs with an emphasis on the origin of structural evolution at the atomic scale using *in situ* TEM. So far, traditional probe based *in situ* TEM holders have been used to make real-time observations in TEM, but these holders are hard to tilt and keep stable for a long time.[190,191] Gong and his co-workers introduced a microchip *in situ* TEM holder to examine the chemical and structural evolution of layered $LiCoO_2$ upon electrochemical delithiation.[190] They discovered that, after delithiation, the single crystal $LiCoO_2$ became polycrystalline and connected with antiphase domain boundaries and coherent twin boundaries. This discovery was not consistent with traditional liquid electrolyte LIBs, where $LiCoO_2$ underwent a series of phase transitions upon delithiation.[192,193] Using a similar microchip TEM holder, a 3D atomic-level observation for structure evolution of $LiNi_{0.5}Mn_{1.5}O_4$ (LNMO) was also evaluated in a working ASSB.[194] It was observed that the non-uniform extraction of Li ions resulted in localized migration of transition metal ions with the generation of antiphase boundaries. Besides, the presence of inherent dislocations further assisted the migration of transition metal ions, which considerably decreased the battery performance. In contrast to traditional battery designs, recently a bulk type ASSB was developed and operated in TEM to analyze the conduction mechanism of Li ions in the $Li_xNi_{0.8}Co_{0.15}Al_{0.05}O_2$ (NCA) cathode.[195] A direct observation under low and high rate charge/discharge reaction conditions demonstrated that sluggish diffusion in nanocrystal grain boundaries was considered the main issue limiting Li transfer in cathodes (Fig. 19A). Such discoveries led to the use of single crystal particles without grain boundaries to enhance the rate performance of ASSBs.

Besides the cathode, the anode is also a key component of ASSBs in improving its performance where a Li metal anode offers the highest capacity (3860 mA h g^{-1}) with the lowest electrochemical potential (−3.05 V). However, a profound understanding of Li plating/de-plating is highly desired. Li plating/de-plating inside parallel hollow tubules made of the mixed ionic electronic conductor (MIES) was investigated by *in situ* TEM.[196] During plating, the Li crystal appeared with a lattice spacing of 0.248 nm perpendicular to the wall. Upon de-plating, a void plug is produced between the solid electrolyte and residual Li. Metallic Li in the form of single crystals can appear out of and back down inside the tubules through the diffusional ''Coble creep mechanism'' at the MIEC/metal phase boundary (Fig. 19B). It is believed that the Coble creep mechanism can retain the ionic and electronic contacts, efficiently relieve stress, eradicate solid state interphase debris and enable reversible plating/de-plating of Li over a length of a few micrometers (10 mm). Recently a solid electrolyte open cell was designed and the real-time observation of reversible Li ion insertion/de-insertion inside bilayer graphene was made by *in situ* TEM.[197] It was reported that upon insertion the multi-layer close-packed structure of the Li atom between two graphene sheets was viable and in this phase the Li storage capacity far exceeds that expected with the formation of LiC_6. These findings not only illustrate the direct observation of Li ion insertion/de-insertion in bilayer graphene but also point to the possibility of different storage mechanisms of ions in 2D materials than their bulk counterparts.[197]

Na metal as an anode has the highest gravimetric capacity (1166 mA h g^{-1}) in the Na metal battery system. However, the formation of Na dendrites during plating/stripping, interaction and distribution of the Na metal deposited on the carbon substrate is a crucial challenge that requires a deep understanding. Using CNF as the substrate (current collector), the direct dynamic electrochemical and topographical evolution upon Na plating/stripping was visualized.[80] During the plating

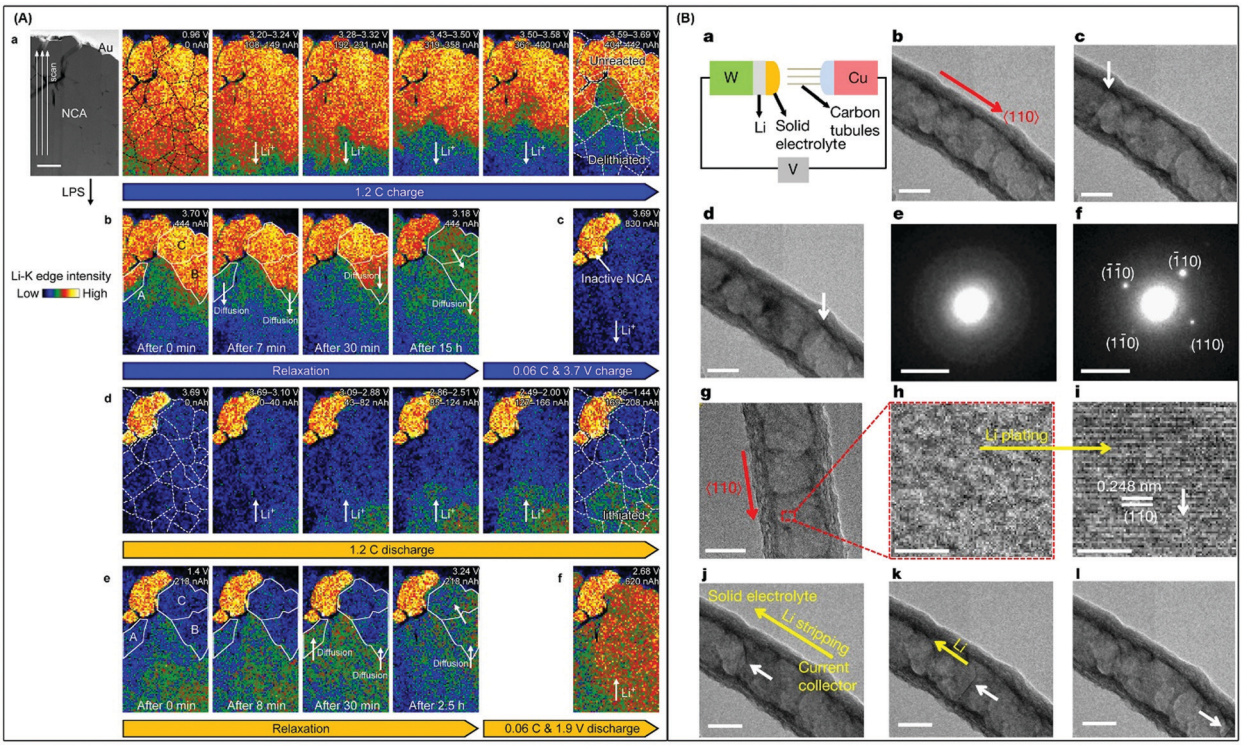

Fig. 19 (A) Dynamic imaging of Li-ion diffusion in NCA under high-rate reaction conditions: (a) ADF-STEM image and a series of corresponding Li concentration maps of NCA acquired during 1.2C charging. Scale bar: 500 nm. (b) A series of Li concentration maps acquired under open circuit conditions after 1.2C charging. (c) Li-Concentration map after constant voltage (3.7 V) charging. (d) A series of Li-concentration maps acquired during 1.2C discharging. (e) A series of Li-concentration maps acquired under open-circuit conditions after 1.2C discharging. (f) Li-concentration map after constant voltage (1.9 V) discharging. Reproduced with permission.[195] Copyright 2020, American Chemical Society. (B) Lithium plating/stripping inside carbon tubules: (a) *in situ* TEM set-up. (b–d) TEM imaging of Li plating with fronts marked by white arrows with increasing time. (e and f) SAED changes from e to f during Li plating. (g–i) HRTEM imaging of a tubule after plating. (j–l) TEM imaging of Li stripping. Scale bars: b–d, g, j–l, 100 nm; h, i, 2 nm; and e, f, 5 nm^{-1}. Reproduced with permission.[196] Copyright 2020, Nature Publishing Group.

process, initially the Na ions were inserted uniformly at a rate of 2 nm s^{-1} to 15 nm s^{-1} at the tip of a CNF. With the continuous insertion of Na ions, the deposition of Na occurred in the form of nanoparticles (tens of nanometers) homogeneously on the entire surface of the fiber, and subsequently these nanoparticles aggregated into micro-particles. During the stripping process, the Na micro-particles deposited on the CNF vanished entirely, showing a highly reversible process. Some interesting facts were also suggested regarding the CNF network: (1) the amorphous part of the CNF exhibited superior Na ion insertion or plating/stripping to its crystalline counterpart. (2) The diffusion rate of Na ion insertion inside the CNF is slower compared with the Na metal plating reaction. (3) The mesopores present in the CNF are more favorable sites for the deposition and nucleation growth of Na that may lead to the generation of Na dendrites in a real cell. (4) The diffusion of Na ions in the inter-fiber permits the even growth of Na inside the network without interfacing the solid electrolyte, as the interior void spaces are far from the solid electrolyte, and therefore can be used for dendrite-free Na storage or plating, particularly in all solid state Na batteries.[80]

In short, antiphase domain boundaries, coherent twin boundaries, dislocations and sluggish diffusion in nanocrystal grain boundaries are the major factors that lead to structural degradation of cathode materials and slow Li transfer, resulting in poor battery performance. Based on these discoveries, structural and compositional engineering (such as doping with lower valence state cations and reduction of particle size) can be attractive approaches to improve the performance of cathodes in ASSBs. During *in situ* Li deposition/extraction, a diffusional Coble creep mechanism is identified which is considered to effectively accommodate the mechanical stress and improve the performance.

6.4. Cryogenic TEM for the study of battery materials and interfaces

It is well known that the fragile nature of the interface, Li metal and SSEs are very sensitive to an electron beam. Therefore, it is not easy to perform atomically resolved imaging such as Li dendrite images from traditional TEM, because an electron beam seriously deteriorates the microstructures of Li dendrites. Recently, it has been revealed that cryogenic protection could preserve the intrinsic properties of the observed sample and minimize the beam effect.[62,198] This makes it possible to study the dendrites, single Li metal atoms and their interfaces with the SEI at atomic scale resolution. Using this method, no damage in the morphology of Li metal dendrites was identified up to or even after 10 minutes. However, in this approach, a very thin specimen (<100 nm) placed onto the TEM grid was

used, which prevents the examination of conventional fabricated and cycled bulk materials. Later, the potential of the cryogenic focused ion beam (cryo-FIB) approach was explored for processing and characterizing the bulk morphology of electrochemically deposited Li (EDLi) metal, which was coupled with cryo-TEM and revealed the complex structural phenomenon at Li–metal/SSE interfaces.[65] Kourkoutis and his co-workers also used the cryo-FIB and cryo-STEM techniques to study the chemical mapping of Li dendrites and solid–liquid interfaces in Li metal batteries.[64] They preserved the original characteristics of the liquid electrolyte by rapid freezing and vitrifying the liquid electrolyte and discovered two types of dendrites coexisting on the Li metal, each with different chemical composition and structure (Fig. 20a–f): one type of dendrite contains an extended SEI layer, a small curvature and a 5 μm diameter, while the other type consists of Li hydride (LiH) with a length of several hundred nanometers and might contribute disproportionately to capacity fading. These discoveries provide guidelines to find various strategies to overcome these issues and their detrimental effects.[66,67] It was also found that the introduction of the Li_2S additive can modify the Li–metal/electrolyte interface, resulting in stable ASSBs.[67] For example, without using any additive, a mosaic interface between the Li metal and poly(ethylene oxide) (PEO) was observed, in which ample grains of Li, LiOH, LiO_2 and Li_2O_3 are unevenly distributed as revealed by cryo-TEM (Fig. 20g–o).[67] However, the introduction of Li_2S rapidly decomposed the $N(CF_3SO_2)_2$, which promoted the generation of abundant LiF nanocrystals in the Li/PEO, leading to the inhibition of the continuous interface reaction at the Li/PEO interface and improved the cycling capability and stability (Fig. 20p–x).[67]

Although cryo-TEM is currently a subject of intense interest and has revealed the importance of studying beam sensitive battery materials, such as Li metal deposition, dendrites,

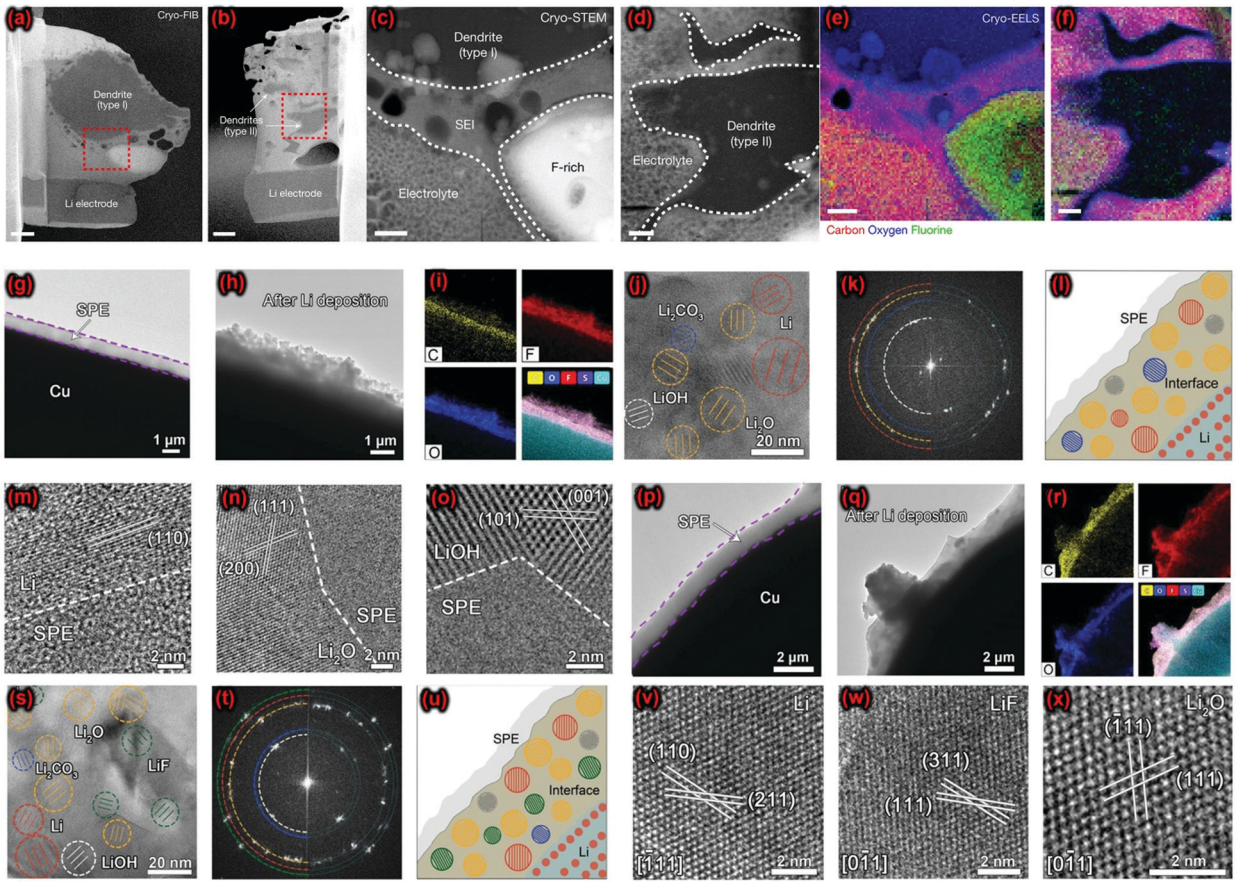

Fig. 20 (a–f) Structure and elemental composition of dendrites and their interphase layers in electron-transparent lamellae: electron transparent cryo-FIB lift-out lamellae of (a) type I and (b) type II dendrites. HAADF cryo-STEM images of (c) type I dendrites and (d) type II dendrites. (e and f) EELS elemental mapping shows that both SEIs are oxygen-rich, but that the type II SEI contains no carbon. Scale bars: (a and b), 1 μm (c–f), 300 nm. Reproduced with permission.[64] Copyright 2018, Nature publishing group. (g–o) Cryo-TEM characterization of the Li/PEO interface using the PEO–LiTFSI electrolyte: (g and h) TEM images illustrating morphological changes before and after Li deposition. (i) The corresponding distributions of C, O, F, S, and Cu elements. (j) Recognized crystalline grains of Li metal, Li_2O, Li_2CO_3, and LiOH in the interface. (k) The corresponding FFT of (j). (l) The schematic diagram for the identified mosaic structure of the interface. (m–o) HRTEM images of the interface between crystalline Li, Li_2O, and LiOH, and amorphous SPE. (p–x) Cryo-TEM characterization of the Li/PEO interface using the PEO–LiTFSI–Li_2S electrolyte: (p and q) TEM images illustrating morphological changes before and after Li deposition. (r) The corresponding distributions of C, O, F, S, and Cu elements. (s) HRTEM image of the interface. (t) The corresponding FFT of (s). (u) Schematic diagram of the observed LiF-rich interface. (v–x) HRTEM images of Li, LiF, and Li_2O showing a long-range ordering lattice. Reproduced with permission.[67] Copyright 2020, WILEY-VCH Verlag GmbH & Co. KGaA, Weinheim.

interface and failure mechanism of electrode materials in liquid and SSE electrolytes,[199,200] it cannot provide time-resolved critical observation regarding cell operation, so future advancement in TEM is still required to study chemically active and beam sensitive battery materials.

7. Summary and outlook

Nowadays, TEM has become an essential characterization technique to achieve mechanistic understanding regarding rechargeable batteries and beyond. A suitable nano-battery design and experimental setup in TEM enable direct visualization of the possible electrochemical processes involved in different kinds of batteries. Contrary to other bulk level characterizations, *in situ* TEM allows real-time imaging and provides localized information during electrochemical processes at the atomic level, thereby providing an in-depth understanding of the working principle, device failure and capacity fading mechanisms in rechargeable batteries. Therefore, it gives an opportunity to work on specific issues to increase the efficiency of electrode materials or electrolytes to increase the life span of batteries. This article summarizes studies on the recent progress and discoveries made by *in situ* TEM in monitoring and understanding the mechanisms for rechargeable batteries beyond Li, in which an extensive advancement has been achieved over the past few years. In particular, the charge storage mechanisms in four different rechargeable battery systems including H-AIBs (SIBs, KIBs, and multi-ion batteries), Li–S batteries, AOBs (Li–O_2, Na–O_2 and K–O_2) and ASSBs are elaborated. The key findings achieved by *in situ* TEM in various rechargeable battery systems in the past decade are summarized in Table 1. The substantial discoveries in H-AIBs including the role of crystal defects in charge storage and transport, reaction details in intercalation, alloying and conversion processes, the diffusivity of metal ions in various electrodes, phase transformations, the kinetics of phase boundary migration, structural/morphological evolution, mechanical stress changes and volume expansion/contraction are studied. The discoveries about the formation mechanism of SEI in H-AIBs are rarely available in the published literature. However, *in situ* TEM studies reveal that the SEI layer Na_2O is formed on the electrode in the case of SIBs, which is very thin,[81] while a thick SEI layer KOH is observed with a thickness of $\sim$10 nm in the case of KIBs.[134] Therefore, better initial CE and performance have been observed in SIBs than in KIBs because a thick layer may trap more irreversible K^+ ions, leading to a lower initial CE, high impedance in most electrode materials, and thus capacity fading. Besides, no *in situ* TEM study that reveals the formation mechanism of SEI in the anodes of Ca or Mg ion batteries is available *yet*.

In the case of Li–S batteries, the contributions of *in situ* TEM are towards understanding the Li dendrite evolution, degradation of the Li anode, phase separation, redox reaction kinetics, and generation of polysulfides. As for AOBs, real-time TEM directly visualizes the generation and oxidation mechanisms of discharge products, interactions among discharge products such as parasitic/side reaction, and important factors in limiting the kinetics of ORR and OER. In Li–O_2 and Na–O_2 batteries, the reaction intermediates generated during the ORR are LiO_2 and NaO_2, which subsequently transformed into Li_2O_2 and Na_2O_2, respectively, *via* disproportionation reactions, while in the case of K–O_2 batteries, the discharge product is only KO_2, which is more kinetically and thermodynamically stable than LiO_2 and NaO_2. During the OER, when an aprotic liquid electrolyte is used as the electrolyte, the reaction prefers to start at the interface between the electrode and discharge product (electronic conduction-limited). However, in the case of solid electrolyte, it happens at the electrolyte/discharge product interface, indicating the ion diffusion-limited process. These *in situ* TEM findings provide valuable guidance for the optimization of cathode materials, electrolytes, and electrocatalysts for air cathodes to prevent device failure and improve the overall performance of rechargeable batteries.

In ASSBs, *in situ* TEM comprehensively provides the phase transformation, structural evolution, dynamic interfacial behavior, reaction kinetics, and degradation and failure mechanism of electrodes, SSEs and their interphases. Moreover, *in situ* TEM still has much higher potential to further improve the basic knowledge for understanding the complex working mechanism of rechargeable batteries. Although great efforts have been made by microscopists and electrochemists, many challenges still exist, which need to be addressed to further improve the performance. The main challenges and future research directions associated with *in situ* TEM are given as follows:

(1) The *in situ* cell design for TEM should be prepared very carefully because most of the different information of the same materials in the literature may arise due to different cell geometry and the testing environment, leading to different results and confusions. Therefore, there should be standard criteria to prepare the *in situ* TEM cell and get more reliable results under optimized conditions.

(2) An electron beam has energy from tens to hundreds of keV that may generate adverse reactions such as sample heating or contamination, atomic displacement, and sputtering in a targeted sample and significantly disturb the imaging process. In the case of a solid state open cell, the alkali oxide (Li_2O, Na_2O) may decompose under an electron beam which may slow down the electrochemical process. This issue could be reduced by using a low dose electron beam or a low voltage operation. In contrast, in a sealed liquid cell design, an electron beam can induce more side reactions in liquid electrolytes including bubble formation, breakdown of the electrolyte and precipitation/dissolution. These issues can be addressed by designing a suitable micro/nanocell such as a graphene cell, which can allow the electron beam penetration as well as provide enough space and environment for electrochemical reactions.

(3) It is quite problematic to estimate the overpotential and its relation with electrochemical reaction dynamics upon *in situ* TEM tests, which rely on the contact geometry between the electrolytes and electrodes. This issue can be addressed by engineering a three-electrode setup inside the cells for reliable electrochemistry.

Table 1 *In situ* TEM findings in rechargeable batteries

Battery systems	*In situ* TEM discoveries
SIBs	Intercalation based materials: the charge storage mechanism and structural degradation of intercalation type electrodes can be found by *in situ* TEM.[76,77] The major findings in carbon-based electrodes are the irreversible interlayer (*d*-spacing) expansion,[73,75] reversible Na metal cluster generation and irreversible formation of Na_2O,[78] charge storage behavior,[75,81] absorption to intercalation mode and little structural degradation,[74] while in layered cathode materials thermal instability in a structure is found.[45,46,204] Alloying based materials: the major discoveries in alloying type electrodes are compositional and microstructure evolution,[94,95] sequential phase transformation,[97] stress relaxation,[95] formation of pores,[93] volume expansion,[14,18] mechanical cracking/fracture,[89,93,94,98] changes in the local structure and grain boundaries,[16] migrating phase boundary,[94] electrochemical sodiation rate,[98] diffusivity of Na ions,[96,98] elongation rate,[92] anisotropic volumetric expansion and strip-like sodium transport behavior in phosphorene,[91] sodiation kinetics,[100] and selective ionic transport properties in phosphorene.[90] Based on these discoveries, the battery performance of these electrodes can be improved by hybrid and structural engineering. Conversion based electrodes: the conversion type electrodes involve multiphase reactions, large volumetric expansion and morphology changes.[114] To date, *in situ* TEM findings include phase transformation,[130] microstructure and phase evolution,[112,120,121,124] formation of various defects such as pores,[126] dislocations[116,129] and grain boundaries,[116] cracking and fracturing,[123] different types of sodiation reactions,[87,107,111,126] shrinking core mode,[110,111] profuse dislocation plasticity,[129] nucleation of Na dendrites,[118] reaction kinetics[116,117,119] and anisotropic sodiation.[122] The SEI is a critical factor in determining the performance of a battery and there is no detailed discussion on SEI formation provided by *in situ* TEM, which can be the future direction.
KIBs and multi-ion batteries	In KIBs, the charge storage behavior and degradation mechanism in a few electrodes are observed by *in situ* TEM.[134,135,205,206] To date, discoveries for KIB electrodes include the potassiation mechanism,[134] fracture and volume expansion[77,134] and diffusivity of K ions within the CF_x cathode. In a FeS_2 electrode, fractures during lithiation are found, but not with larger alkali ions like K^+.[136] The *in situ* TEM study of multi-ion batteries reveals the sluggish ion diffusion of Mg^{2+} and Al^{3+} in a Co_3O_4 electrode, *i.e.* no electrochemical reaction,[141] while Ca^{2+} ion insertion in WO_3 follows the intercalation initiated conversion reaction in WO_3 along with poor diffusivity of Ca^{2+}.[139]
Li–S batteries	In Li–S batteries, the (de)lithiation processes, volume changes, structural evolution and Li polysulfide (LPS) formation are investigated by *in situ* TEM.[63,156] Specifically, *in situ* TEM findings are phase transformation,[149] S/Li_2S phase separation,[145] sulfur sublimation,[151] Li_2S dissolution/re-deposition mechanism,[146] diffusivity of Li ions[148,207] and catalytic decomposition of Li_2S by Li_xTiS_2.[157] In the future, the migration of LPS and structure evolution can be investigated by sealed cell nanobattery design using a liquid electrolyte that will be closer to a real battery system.
Li–O_2 batteries	In Li–O_2 batteries, *in situ* TEM is used to study the growth and decomposition of the discharge product, reaction mechanisms and morphology evolution of the discharge product. So far the *in situ* TEM findings in Li–O_2 are as follows: the factors limiting the kinetics in Li_2O_2 during growth and decomposition,[48,52,164] sluggish discharge–charge kinetics,[164] various morphologies of the discharge product, uneven distribution of electronic/ionic conductivities and kinetics of oxygen release,[56] conventional Ostwald ripening and nonclassical crystallization,[49] disproportionation reaction of LiO_2 and formation of a hollow nanostructure,[50,57] gradual growth of toroidal Li_2O_2,[51] and electrochemical activity of RuO_2 as a bifunctional catalyst.[53,165]
Na–O_2 batteries	The *in situ* findings for Na–O_2 batteries are as follows: the growth of NaO_2 and disproportionation reaction of Na_2O into Na_2O_2 and O_2,[58,59,168,169] ORR in bare MnO_2,[58] formation of NaO_2 cubes by solution-mediated nucleation process,[54] impingement of NaO_2 and particle coarsening by coalescence,[60] formation of Cu clusters during *in situ* sodiation of CuS,[169] accumulation of insoluble discharge products,[168] and high overpotential.[166]
K–O_2 batteries	The *in situ* TEM discoveries for K–O_2 batteries include the reduction of α-MnO_2 into Mn_3O_4 and MnO, and the growth of KoO_2 on the electrode (α-MnO_2) surface.[61]
ASSBs	*In situ* TEM can be used to observe the reaction and degradation in solid electrolytes, electrodes, and interfacial stability in ASSBs. So far the main discoveries include morphological and structural evolution at electrode/electrolyte interfaces,[184,185,188,189,194,208] localized phase transitions,[184] high interfacial impedance,[187] the decomposition of the cathode,[44] the deposition of Li dendrites inside the electrolyte,[186] self-discharge,[147,180] potential distribution and Li ion diffusion,[43] non-uniform extraction/insertion of Li ions during charging/discharging,[181] Li accumulation at the anode/current collector and cathode electrolyte interfaces,[182] the formation of twin boundaries and antiphase grain boundaries,[190] diffusional Coble creep mechanism[196] and sodium plating/stripping.[80] Based on these discoveries many side reactions and interfacial limitations can be addressed by efficient interfacial engineering (such as surface coating) of SSEs, anodes and cathodes.

(4) Currently, almost all *in situ* TEM nanocell systems in TEM perform the charge/discharge process for a few cycles, and therefore the microstructural changes of battery materials over long cycles cannot be revealed. This issue can be addressed using the execution of 4D imaging in combination with accelerated tests, which may provide an understanding of the structural evolution of materials over long cycles.

(5) Introducing multiple stimuli (heating or cooling together with bias) simultaneously inside TEM in a controlled environment can be interesting. Recently many sealed cell designs and microelectromechanical chips have been developed, and therefore it is quite interesting to perform the electrochemical investigation in a complex environment. The combination of sealed liquid cells and a thin film heater in one

cell design may be used to investigate the battery reactions at different temperatures, which could provide thermal failure mechanisms in secondary ion batteries. Moreover, using the solid state open cell design inside ETEM and introducing water vapor or air the degradation mechanisms of SSEs can be evaluated under atmospheric conditions.

(6) The new emerging TEM techniques such as 4D STEM, geometric phase analysis (GPA) and integrated differential phase constant (iDPC) may play vital roles in the investigation of ASSB materials. For example, 4D STEM is used to examine the structure, charge, composition and strain mapping of electrodes.[201]

(7) In AOBs, it is necessary to understand many issues such as (i) the working principle and usefulness of ORR/OER catalysis, (ii) discharging/charging reaction routes, (iii) the influence of electrode materials on the reaction intermediate and discharge products, (iv) active sites for the growth and decomposition of discharge products, and (v) the basic reason for cell degradation and reaction instability. This can be done by developing *in situ* TEM that can probe solid/liquid/gas interfaces simultaneously.

(8) For next-generation energy storage systems, aqueous rechargeable batteries (ARBs) are very promising as they use water electrolyte which is more ionically conductive, safe, environmentally benign and cost effective compared to flammable organic liquid electrolytes, and in the past five years a lot of progress has been made on this interesting topic.[202] It is worth studying the electrochemical dynamics of ARBs during the running of the battery. In this regard, an *in situ* TEM study was conducted in which a TEM liquid flow cell was used to study the real-time lithiation state of the $LiFePO_4$ cathode and the surrounding aqueous electrolyte during the charging/discharging processes.[203] However, despite the current intensive research on ARBs, no *in situ* TEM study that reveals the internal mechanism and structural degradation of electrodes has been reported. This is due to some issues such as inadequate atmospheric pressure produced by the currently available differential pumping technology, which leads to high vapor pressure in water, resulting in a precipitate out of dissolved salt in water, or may block out the liquid supplying pipe, particularly in ETEM. In order to mitigate these issues, advanced differential pumping techniques must be established for aqueous electrolyte based *in situ* TEM and a deep understanding of ARBs.

Conclusively, by giving an overview of *in situ* TEM to study these battery systems, this review article will attract more attention in this field and deliver broad investigations to the readers who are working on new electrode designs for enhancing the battery performance.

Conflicts of interest

There are no conflicts to declare.

Acknowledgements

The authors are grateful for the financial support of this work from the National Natural Science Fund for Distinguished Young Scholars (52025133), the Tencent Foundation through the XPLORER PRIZE, the Beijing Natural Science Foundation (JQ18005), the National Natural Science Foundation of China (Grant No. 51672007 and 11974023), the Fund of the State Key Laboratory of Solidification Processing in NWPU (Grant No. SKLSP202004) and the Key Area R&D Program of Guangdong Prov. (2018B030327001, 2018B010109009). Moreover, N. M. is grateful for the financial support from RMIT Vice-Chancellor Fellowship, RMIT University, Australia and would like to acknowledge the scientific and technical assistance of the Micro Nano Research Facility (MNRF) and the Australian Microscopy & Microanalysis Research Facility (RMMF) at RMIT University.

Notes and references

1 S. Chu, Y. Cui and N. Liu, *Nat. Mater.*, 2016, **16**, 16–22.
2 D. Larcher and J. M. Tarascon, *Nat. Chem.*, 2015, **7**, 19–29.
3 C. P. Grey and J. M. Tarascon, *Nat. Mater.*, 2016, **16**, 45–56.
4 L. A. Ellingsen, C. R. Hung, G. Majeau-Bettez, B. Singh, Z. Chen, M. S. Whittingham and A. H. Stromman, *Nat. Nanotechnol.*, 2016, **11**, 1039–1051.
5 S. Chu and A. Majumdar, *Nature*, 2012, **488**, 294–303.
6 R. Schmuch, R. Wagner, G. Hörpel, T. Placke and M. Winter, *Nat. Energy*, 2018, **3**, 267–278.
7 C. Vaalma, D. Buchholz, M. Weil and S. Passerini, *Nat. Rev. Mater.*, 2018, **3**, 18013.
8 G. Assat and J.-M. Tarascon, *Nat. Energy*, 2018, **3**, 373–386.
9 F. Fuso Nerini, J. Tomei, L. S. To, I. Bisaga, P. Parikh, M. Black, A. Borrion, C. Spataru, V. Castán Broto, G. Anandarajah, B. Milligan and Y. Mulugetta, *Nat. Energy*, 2017, **3**, 10–15.
10 T. Hosaka, K. Kubota, A. S. Hameed and S. Komaba, *Chem. Rev.*, 2020, **120**, 6358–6466.
11 P. G. Bruce, S. A. Freunberger, L. J. Hardwick and J.-M. Tarascon, *Nat. Mater.*, 2012, **11**, 172.
12 H. Yadegari and X. Sun, *Trends Chem.*, 2020, **2**, 241–253.
13 H.-F. Wang and Q. Xu, *Matter*, 2019, **1**, 565–595.
14 J. W. Choi and D. Aurbach, *Nat. Rev. Mater.*, 2016, 1.
15 V. Palomares, P. Serras, I. Villaluenga, K. B. Hueso, J. Carretero-González and T. Rojo, *Energy Environ. Sci.*, 2012, **5**, 5884.
16 R. Rajagopalan, Y. Tang, X. Ji, C. Jia and H. Wang, *Adv. Funct. Mater.*, 2020, **30**, 1909486.
17 A. Mistry and P. P. Mukherjee, *J. Phys. Chem. C*, 2017, **121**, 26256–26264.
18 A. Banerjee, X. Wang, C. Fang, E. A. Wu and Y. S. Meng, *Chem. Rev.*, 2020, **120**, 6878–6933.
19 J. Woods, N. Bhattarai, P. Chapagain, Y. Yang and S. Neupane, *Nano Energy*, 2019, **56**, 619–640.
20 J. Lu, T. Wu and K. Amine, *Nat. Energy*, 2017, 2.
21 Y. Yang, X. Liu, Z. Dai, F. Yuan, Y. Bando, D. Golberg and X. Wang, *Adv. Mater.*, 2017, 29.
22 L. Xu, S. Tang, Y. Cheng, K. Wang, J. Liang, C. Liu, Y.-C. Cao, F. Wei and L. Mai, *Joule*, 2018, **2**, 1991–2015.
23 R. Zou, Z. Cui, Q. Liu, G. Guan, W. Zhang, G. He, J. Yang and J. Hu, *J. Mater. Chem. A*, 2017, **5**, 20072–20094.

24 Z. Fan, L. Zhang, D. Baumann, L. Mei, Y. Yao, X. Duan, Y. Shi, J. Huang, Y. Huang and X. Duan, *Adv. Mater.*, 2019, **31**, e1900608.
25 J. Li, G. Johnson, S. Zhang and D. Su, *Joule*, 2019, **3**, 4–8.
26 K.-W. Nam, S.-M. Bak, E. Hu, X. Yu, Y. Zhou, X. Wang, L. Wu, Y. Zhu, K.-Y. Chung and X.-Q. Yang, *Adv. Funct. Mater.*, 2013, **23**, 1047–1063.
27 S. Wang, Q. Liu, C. Zhao, F. Lv, X. Qin, H. Du, F. Kang and B. Li, *Energy Environ. Mater.*, 2018, **1**, 28–40.
28 Y. Yuan, K. Amine, J. Lu and R. Shahbazian-Yassar, *Nat. Commun.*, 2017, 8.
29 J. Y. Huang, L. Zhong, C. M. Wang, J. P. Sullivan, W. Xu, L. Q. Zhang, S. X. Mao, N. S. Hudak, X. H. Liu and A. Subramanian, *Science*, 2010, **330**, 1515.
30 M. Shao, *J. Power Sources*, 2014, **270**, 475–486.
31 T. Shang, Y. Wen, D. Xiao, L. Gu, Y.-S. Hu and H. Li, *Adv. Energy Mater.*, 2017, **7**, 1700709.
32 X. H. Liu and J. Y. Huang, *Energy Environ. Sci.*, 2011, **4**, 3844.
33 X. H. Liu, J. W. Wang, Y. Liu, H. Zheng, A. Kushima, S. Huang, T. Zhu, S. X. Mao, J. Li, S. Zhang, W. Lu, J. M. Tour and J. Y. Huang, *Carbon*, 2012, **50**, 3836–3844.
34 Z.-H. Xie, Z. Jiang and X. Zhang, *J. Electrochem. Soc.*, 2017, **164**, A2110–A2123.
35 J. Wu, F. Ma, X. Liu, X. Fan, L. Shen, Z. Wu, X. Ding, X. Han, Y. Deng, W. Hu and C. Zhong, *Small Methods*, 2019, **3**, 1900158.
36 X. Liu and L. Gu, *Small Methods*, 2018, **2**, 1800006.
37 X. H. Liu, Y. Liu, A. Kushima, S. Zhang, T. Zhu, J. Li and J. Y. Huang, *Adv. Energy Mater.*, 2012, **2**, 722–741.
38 A. Brazier, L. Dupont, L. Dantras-Laffont, N. Kuwata, J. Kawamura and J. M. Tarascon, *Chem. Mater.*, 2008, **20**, 2352–2359.
39 J. Z. Lee, T. A. Wynn, Y. S. Meng and D. Santhanagopalan, *J. Visualized Exp.*, 2018, (133), e56259, DOI: 10.3791/56259.
40 S. Rubanov and P. R. Munroe, *J. Mater. Sci. Lett.*, 2001, **20**, 1181–1183.
41 M. Schaffer, B. Schaffer and Q. Ramasse, *Ultramicroscopy*, 2012, **114**, 62–71.
42 S. Bals, W. Tirry, R. Geurts, Z. Yang and D. Schryvers, *Microsc. Microanal.*, 2007, **13**, 80–86.
43 K. Yamamoto, Y. Iriyama, T. Asaka, T. Hirayama, H. Fujita, C. A. Fisher, K. Nonaka, Y. Sugita and Z. Ogumi, *Angew. Chem., Int. Ed.*, 2010, **49**, 4414–4417.
44 Z. Wang, D. Santhanagopalan, W. Zhang, F. Wang, H. L. Xin, K. He, J. Li, N. Dudney and Y. S. Meng, *Nano Lett.*, 2016, **16**, 3760–3767.
45 S. Hwang, Y. Lee, E. Jo, K. Y. Chung, W. Choi, S. M. Kim and W. Chang, *ACS Appl. Mater. Interfaces*, 2017, **9**, 18883–18888.
46 S. Hwang, S. M. Kim, S.-M. Bak, S. Y. Kim, B.-W. Cho, K. Y. Chung, J. Y. Lee, E. A. Stach and W. Chang, *Chem. Mater.*, 2015, **27**, 3927–3935.
47 M. Gu, L. R. Parent, B. L. Mehdi, R. R. Unocic, M. T. McDowell, R. L. Sacci, W. Xu, J. G. Connell, P. Xu, P. Abellan, X. Chen, Y. Zhang, D. E. Perea, J. E. Evans, L. J. Lauhon, J.-G. Zhang, J. Liu, N. D. Browning, Y. Cui, I. Arslan and C.-M. Wang, *Nano Lett.*, 2013, **13**, 6106–6112.
48 L. Zhong, R. R. Mitchell, Y. Liu, B. M. Gallant, C. V. Thompson, J. Y. Huang, S. X. Mao and Y. Shao-Horn, *Nano Lett.*, 2013, **13**, 2209–2214.
49 C. Yang, J. Han, P. Liu, C. Hou, G. Huang, T. Fujita, A. Hirata and M. Chen, *Adv. Mater.*, 2017, 29.
50 P. Liu, J. Han, X. Guo, Y. Ito, C. Yang, S. Ning, T. Fujita, A. Hirata and M. Chen, *Sci. Rep.*, 2018, **8**, 3134.
51 D. Lee, H. Park, Y. Ko, H. Park, T. Hyeon, K. Kang and J. Park, *J. Am. Chem. Soc.*, 2019, **141**, 8047–8052.
52 A. Kushima, T. Koido, Y. Fujiwara, N. Kuriyama, N. Kusumi and J. Li, *Nano Lett.*, 2015, **15**, 8260–8265.
53 C. Hou, J. Han, P. Liu, C. Yang, G. Huang, T. Fujita, A. Hirata and M. Chen, *Nano Energy*, 2018, **47**, 427–433.
54 L. Lutz, W. Dachraoui, A. Demortiere, L. R. Johnson, P. G. Bruce, A. Grimaud and J. M. Tarascon, *Nano Lett.*, 2018, **18**, 1280–1289.
55 J. B. Wagner, F. Cavalca, C. D. Damsgaard, L. D. Duchstein and T. W. Hansen, *Micron*, 2012, **43**, 1169–1175.
56 H. Zheng, D. Xiao, X. Li, Y. Liu, Y. Wu, J. Wang, K. Jiang, C. Chen, L. Gu, X. Wei, Y. S. Hu, Q. Chen and H. Li, *Nano Lett.*, 2014, **14**, 4245–4249.
57 L. Luo, B. Liu, S. Song, W. Xu, J. G. Zhang and C. Wang, *Nat. Nanotechnol.*, 2017, **12**, 535–539.
58 Q. Liu, L. Geng, T. Yang, Y. Tang, P. Jia, Y. Li, H. Li, T. Shen, L. Zhang and J. Huang, *Energy Storage Mater.*, 2019, **19**, 48–55.
59 Q. Liu, T. Yang, C. Du, Y. Tang, Y. Sun, P. Jia, J. Chen, H. Ye, T. Shen, Q. Peng, L. Zhang and J. Huang, *Nano Lett.*, 2018, **18**, 3723–3730.
60 W.-J. Kwak, L. Luo, H.-G. Jung, C. Wang and Y.-K. Sun, *ACS Energy Lett.*, 2018, **3**, 393–399.
61 Y. Tang, L. Zhang, Y. Tang, X. Wang, T. Zhang, R. Yang, C. Ma, N. Li, Y. Liu, X. Zhao, X. Zhang, Z. Wang, B. Guo, Y. Li and J. Huang, *Chem. Commun.*, 2019, **55**, 10880–10883.
62 Y. Li, Y. Li, A. Pei, K. Yan, Y. Sun, C.-L. Wu, L.-M. Joubert, R. Chin, A. L. Koh, Y. Yu, J. Perrino, B. Butz, S. Chu and Y. Cui, *Science*, 2017, **358**, 506–510.
63 B. D. Levin, M. J. Zachman, J. G. Werner, R. Sahore, K. X. Nguyen, Y. Han, B. Xie, L. Ma, L. A. Archer, E. P. Giannelis, U. Wiesner, L. F. Kourkoutis and D. A. Muller, *Microsc. Microanal.*, 2017, **23**, 155–162.
64 M. J. Zachman, Z. Tu, S. Choudhury, L. A. Archer and L. F. Kourkoutis, *Nature*, 2018, **560**, 345–349.
65 J. Z. Lee, T. A. Wynn, M. A. Schroeder, J. Alvarado, X. Wang, K. Xu and Y. S. Meng, *ACS Energy Lett.*, 2019, **4**, 489–493.
66 D. Cheng, T. A. Wynn, X. Wang, S. Wang, M. Zhang, R. Shimizu, S. Bai, H. Nguyen, C. Fang, M.-c. Kim, W. Li, B. Lu, S. J. Kim and Y. S. Meng, *Joule*, 2020, **4**, 2484–2500.
67 O. Sheng, J. Zheng, Z. Ju, C. Jin, Y. Wang, M. Chen, J. Nai, T. Liu, W. Zhang, Y. Liu and X. Tao, *Adv. Mater.*, 2020, **32**, e2000223.
68 J. R. Rodriguez, S. B. Aguirre and V. G. Pol, *J. Power Sources*, 2019, **437**, 226851.

69 A. Mahmood, S. Li, Z. Ali, H. Tabassum, B. Zhu, Z. Liang, W. Meng, W. Aftab, W. Guo, H. Zhang, M. Yousaf, S. Gao, R. Zou and Y. Zhao, *Adv. Mater.*, 2019, **31**, e1805430.
70 M. Yousaf, Y. Chen, H. Tabassum, Z. Wang, Y. Wang, A. Y. Abid, A. Mahmood, N. Mahmood, S. Guo, R. P. S. Han and P. Gao, *Adv. Sci.*, 2020, **7**, 1902907.
71 M. Yousaf, Y. Wang, Y. Chen, Z. Wang, A. Firdous, Z. Ali, N. Mahmood, R. Zou, S. Guo and R. P. S. Han, *Adv. Energy Mater.*, 2019, **9**, 1900567.
72 M. M. Doeff, Y. Ma, S. J. Visco and L. C. De Jonghe, *J. Electrochem. Soc.*, 1993, **140**, L169–L170.
73 Z. Jian, C. Bommier, L. Luo, Z. Li, W. Wang, C. Wang, P. A. Greaney and X. Ji, *Chem. Mater.*, 2017, **29**, 2314–2320.
74 K. Wang, Y. Xu, Y. Li, V. Dravid, J. Wu and Y. Huang, *J. Mater. Chem. A*, 2019, **7**, 3327–3335.
75 A. Beda, C. Villevieille, P.-L. Taberna, P. Simon and C. Matei Ghimbeu, *J. Mater. Chem. A*, 2020, **8**, 5558–5571.
76 Y. Wen, K. He, Y. Zhu, F. Han, Y. Xu, I. Matsuda, Y. Ishii, J. Cumings and C. Wang, *Nat. Commun.*, 2014, 5.
77 Y. Liu, F. Fan, J. Wang, Y. Liu, H. Chen, K. L. Jungjohann, Y. Xu, Y. Zhu, D. Bigio, T. Zhu and C. Wang, *Nano Lett.*, 2014, **14**, 3445–3452.
78 J. Wan, F. Shen, W. Luo, L. Zhou, J. Dai, X. Han, W. Bao, Y. Xu, J. Panagiotopoulos, X. Fan, D. Urban, A. Nie, R. Shahbazian-Yassar and L. Hu, *Chem. Mater.*, 2016, **28**, 6528–6535.
79 Y. Liu, H. Zheng, X. H. Liu, S. Huang, T. Zhu, J. Wang, A. Kushima, N. S. Hudak, X. Huang, S. Zhang, S. X. Mao, X. Qian, J. Li and J. Y. Huang, *ACS Nano*, 2011, **5**, 7245–7253.
80 X. Li, L. Zhao, P. Li, Q. Zhang and M.-S. Wang, *Nano Energy*, 2017, **42**, 122–128.
81 Y. Yang, D.-M. Tang, C. Zhang, Y. Zhang, Q. Liang, S. Chen, Q. Weng, M. Zhou, Y. Xue, J. Liu, J. Wu, Q. H. Cui, C. Lian, G. Hou, F. Yuan, Y. Bando, D. Golberg and X. Wang, *Energy Environ. Sci.*, 2017, **10**, 979–986.
82 X. Wang, Q. Weng, X. Liu, X. Wang, D. M. Tang, W. Tian, C. Zhang, W. Yi, D. Liu, Y. Bando and D. Golberg, *Nano Lett.*, 2014, **14**, 1164–1171.
83 Y. Cao, L. Xiao, M. L. Sushko, W. Wang, B. Schwenzer, J. Xiao, Z. Nie, L. V. Saraf, Z. Yang and J. Liu, *Nano Lett.*, 2012, **12**, 3783–3787.
84 P. Gao, L. Wang, Y. Zhang, Y. Huang and K. Liu, *ACS Nano*, 2015, **9**, 11296–11301.
85 L. Wang, Z. Xu, W. Wang and X. Bai, *J. Am. Chem. Soc.*, 2014, **136**, 6693–6697.
86 S. Chen, L. Wang, R. Shao, J. Zou, R. Cai, J. Lin, C. Zhu, J. Zhang, F. Xu, J. Cao, J. Feng, J. Qi and P. Gao, *Nano Energy*, 2018, **48**, 560–568.
87 X. Wang, Z. Yao, S. Hwang, Y. Pan, H. Dong, M. Fu, N. Li, K. Sun, H. Gan, Y. Yao, A. Aspuru-Guzik, Q. Xu and D. Su, *ACS Nano*, 2019, **13**, 9421–9430.
88 B. Han, S. Chen, J. Zou, R. Shao, Z. Dou, C. Yang, X. Ma, J. Lu, K. Liu, D. Yu, L. Wang, H. Wang and P. Gao, *Nanoscale*, 2019, **11**, 7474–7480.
89 J. Sun, H. W. Lee, M. Pasta, H. Yuan, G. Zheng, Y. Sun, Y. Li and Y. Cui, *Nat. Nanotechnol.*, 2015, **10**, 980–985.
90 A. Nie, Y. Cheng, S. Ning, T. Foroozan, P. Yasaei, W. Li, B. Song, Y. Yuan, L. Chen, A. Salehi-Khojin, F. Mashayek and R. Shahbazian-Yassar, *Nano Lett.*, 2016, **16**, 2240–2247.
91 C. Zhu, R. Shao, S. Chen, R. Cai, Y. Wu, L. Yao, W. Xia, M. Nie, L. Sun, P. Gao, H. L. Xin and F. Xu, *Small Methods*, 2019, **3**, 1900061.
92 C. Zhang, X. Wang, Q. Liang, X. Liu, Q. Weng, J. Liu, Y. Yang, Z. Dai, K. Ding, Y. Bando, J. Tang and D. Golberg, *Nano Lett.*, 2016, **16**, 2054–2060.
93 X. Lu, E. R. Adkins, Y. He, L. Zhong, L. Luo, S. X. Mao, C.-M. Wang and B. A. Korgel, *Chem. Mater.*, 2016, **28**, 1236–1242.
94 J. W. Wang, X. H. Liu, S. X. Mao and J. Y. Huang, *Nano Lett.*, 2012, **12**, 5897–5902.
95 Z. Li, X. Tan, P. Li, P. Kalisvaart, M. T. Janish, W. M. Mook, E. J. Luber, K. L. Jungjohann, C. B. Carter and D. Mitlin, *Nano Lett.*, 2015, **15**, 6339–6348.
96 J. S. Gutiérrez-Kolar, L. Baggetto, X. Sang, D. Shin, V. Yurkiv, F. Mashayek, G. M. Veith, R. Shahbazian-Yassar and R. R. Unocic, *ACS Appl. Energy Mater.*, 2019, **2**, 3578–3586.
97 H. Xie, X. Tan, E. J. Luber, B. C. Olsen, W. P. Kalisvaart, K. L. Jungjohann, D. Mitlin and J. M. Buriak, *ACS Energy Lett.*, 2018, **3**, 1670–1676.
98 A. Nie, L.-y. Gan, Y. Cheng, X. Tao, Y. Yuan, S. Sharifi-Asl, K. He, H. Asayesh-Ardakani, V. Vasiraju, J. Lu, F. Mashayek, R. Klie, S. Vaddiraju, U. Schwingenschlögl and R. Shahbazian-Yassar, *Adv. Funct. Mater.*, 2016, **26**, 543–552.
99 T. D. Bogart, A. M. Chockla and B. A. Korgel, *Curr. Opin. Chem. Eng.*, 2013, **2**, 286–293.
100 Q. Li, H. Liu, Z. Yao, J. Cheng, T. Li, Y. Li, C. Wolverton, J. Wu and V. P. Dravid, *ACS Nano*, 2016, **10**, 8788–8795.
101 A. Nie, Y. Cheng, Y. Zhu, H. Asayesh-Ardakani, R. Tao, F. Mashayek, Y. Han, U. Schwingenschlogl, R. F. Klie, S. Vaddiraju and R. Shahbazian-Yassar, *Nano Lett.*, 2014, **14**, 5301–5307.
102 S. Fang, D. Bresser and S. Passerini, *Adv. Energy Mater.*, 2019, **10**, 1902485.
103 L. Li, Y. Zheng, S. Zhang, J. Yang, Z. Shao and Z. Guo, *Energy Environ. Sci.*, 2018, **11**, 2310–2340.
104 F. Klein, B. Jache, A. Bhide and P. Adelhelm, *Phys. Chem. Chem. Phys.*, 2013, **15**, 15876–15887.
105 J. Cabana, L. Monconduit, D. Larcher and M. R. Palacin, *Adv. Mater.*, 2010, **22**, E170–192.
106 Z. Liu, T. Lu, T. Song, X.-Y. Yu, X. W. Lou and U. Paik, *Energy Environ. Sci.*, 2017, **10**, 1576–1580.
107 K. He, Y. Zhou, P. Gao, L. Wang, N. Pereira, G. G. Amatucci, K.-W. Nam, X.-Q. Yang, Y. Zhu, F. Wang and D. Su, *ACS Nano*, 2014, **8**, 7251–7259.
108 F. Wang, H. C. Yu, M. H. Chen, L. Wu, N. Pereira, K. Thornton, A. Van der Ven, Y. Zhu, G. G. Amatucci and J. Graetz, *Nat. Commun.*, 2012, **3**, 1201.
109 K. He, H. L. Xin, K. Zhao, X. Yu, D. Nordlund, T. C. Weng, J. Li, Y. Jiang, C. A. Cadigan, R. M. Richards, M. M. Doeff, X. Q. Yang, E. A. Stach, J. Li, F. Lin and D. Su, *Nano Lett.*, 2015, **15**, 1437–1444.

110 K. He, F. Lin, Y. Zhu, X. Yu, J. Li, R. Lin, D. Nordlund, T. C. Weng, R. M. Richards, X. Q. Yang, M. M. Doeff, E. A. Stach, Y. Mo, H. L. Xin and D. Su, *Nano Lett.*, 2015, **15**, 5755–5763.
111 Y. Yuan, L. Ma, K. He, W. Yao, A. Nie, X. Bi, K. Amine, T. Wu, J. Lu and R. Shahbazian-Yassr, *Nano Energy*, 2016, **19**, 382–390.
112 W. Xia, F. Xu, C. Zhu, H. L. Xin, Q. Xu, P. Sun and L. Sun, *Nano Energy*, 2016, **27**, 447–456.
113 Y. Yuan, C. Liu, B. W. Byles, W. Yao, B. Song, M. Cheng, Z. Huang, K. Amine, E. Pomerantseva, R. Shahbazian-Yassar and J. Lu, *Joule*, 2019, **3**, 471–484.
114 L. Zhang, Y. Wang, D. Xie, Y. Tang, C. Wu, L. Cui, Y. Li, X. Ning and Z. Shan, *RSC Adv.*, 2016, **6**, 11441–11445.
115 X. Wang, D. M. Tang, H. Li, W. Yi, T. Zhai, Y. Bando and D. Golberg, *Chem. Commun.*, 2012, **48**, 4812–4814.
116 P. Gao, Y.-Y. Zhang, L. Wang, S. Chen, Y. Huang, X. Ma, K. Liu and D. Yu, *Nano Energy*, 2017, **32**, 302–309.
117 L. Yao, W. Xia, H. Zhang, H. Dong, H. L. Xin, P. Gao, R. Cai, C. Zhu, Y. Wu, M. Nie, S. Lei, L. Sun and F. Xu, *Nano Energy*, 2019, **60**, 424–431.
118 X. Xia, Q. Wang, Q. Zhu, J. Xie, J. Wang, D. Zhuang, S. Zhang, G. Cao and X. Zhao, *Mater. Today Energy*, 2017, **5**, 99–106.
119 Q. Pan, Q. Zhang, F. Zheng, Y. Liu, Y. Li, X. Ou, X. Xiong, C. Yang and M. Liu, *ACS Nano*, 2018, **12**, 12578–12586.
120 L. Zhang, Y. Tang, Y. Wang, Y. Duan, D. Xie, C. Wu, L. Cui, Y. Li, X. Ning and Z. Shan, *RSC Adv.*, 2016, **6**, 96035–96038.
121 M. G. Boebinger, M. Xu, X. Ma, H. Chen, R. R. Unocic and M. T. McDowell, *J. Mater. Chem. A*, 2017, **5**, 11701–11709.
122 Q. Li, Y. Xu, Z. Yao, J. Kang, X. Liu, C. Wolverton, M. C. Hersam, J. Wu and V. P. Dravid, *ACS Nano*, 2018, **12**, 7875–7882.
123 Q. Su, G. Du, J. Zhang, Y. Zhong, B. Xu, Y. Yang, S. Neupane and W. Li, *ACS Nano*, 2014, **8**, 3620–3627.
124 K. Wu, F. Chen, Z. Ma, B. Guo, Y. Lyu, P. Wang, H. Yang, Q. Li, H. Wang and A. Nie, *Chem. Commun.*, 2019, **55**, 5611–5614.
125 H. Wang, Q. Pan, Y. Cheng, J. Zhao and G. Yin, *Electrochim. Acta*, 2009, **54**, 2851–2855.
126 M. Gu, A. Kushima, Y. Shao, J. G. Zhang, J. Liu, N. D. Browning, J. Li and C. Wang, *Nano Lett.*, 2013, **13**, 5203–5211.
127 J. Y. Huang, L. Zhong, C. M. Wang, J. P. Sullivan, W. Xu, L. Q. Zhang, S. X. Mao, N. S. Hudak, X. H. Liu, A. Subramanian, H. Fan, L. Qi, A. Kushima and J. Li, *Science*, 2010, **330**, 1515–1520.
128 X. Wang, F. Fan, J. Wang, H. Wang, S. Tao, A. Yang, Y. Liu, H. Beng Chew, S. X. Mao, T. Zhu and S. Xia, *Nat. Commun.*, 2015, **6**, 8417.
129 H. Asayesh-Ardakani, W. Yao, Y. Yuan, A. Nie, K. Amine, J. Lu and R. Shahbazian-Yassar, *Small Methods*, 2017, **1**, 1700202.
130 S. Yao, J. Cui, Z. Lu, Z.-L. Xu, L. Qin, J. Huang, Z. Sadighi, F. Ciucci and J.-K. Kim, *Adv. Energy Mater.*, 2017, **7**, 1602149.
131 L. Wu, H. Lu, L. Xiao, J. Qian, X. Ai, H. Yang and Y. Cao, *J. Mater. Chem. A*, 2014, **2**, 16424–16428.
132 Z. Jian, W. Luo and X. Ji, *J. Am. Chem. Soc.*, 2015, **137**, 11566–11569.
133 Y. Xu, J. Zhang and D. Li, *Chem. – Asian J.*, 2020, **15**, 1648–1659.
134 Q. Wang, X. Zhao, C. Ni, H. Tian, J. Li, Z. Zhang, S. X. Mao, J. Wang and Y. Xu, *J. Phys. Chem. C*, 2017, **121**, 12652–12657.
135 Y. Wu, S. Hu, R. Xu, J. Wang, Z. Peng, Q. Zhang and Y. Yu, *Nano Lett.*, 2019, **19**, 1351–1358.
136 M. G. Boebinger, D. Yeh, M. Xu, B. C. Miles, B. Wang, M. Papakyriakou, J. A. Lewis, N. P. Kondekar, F. J. Q. Cortes, S. Hwang, X. Sang, D. Su, R. R. Unocic, S. Xia, T. Zhu and M. T. McDowell, *Joule*, 2018, **2**, 1783–1799.
137 R. C. Massé, E. Uchaker and G. Cao, *Sci. China Mater.*, 2015, **58**, 715–766.
138 M.-C. Lin, M. Gong, B. Lu, Y. Wu, D.-Y. Wang, M. Guan, M. Angell, C. Chen, J. Yang, B.-J. Hwang and H. Dai, *Nature*, 2015, **520**, 324–328.
139 Y. He, M. Gu, H. Xiao, L. Luo, Y. Shao, F. Gao, Y. Du, S. X. Mao and C. Wang, *Angew. Chem., Int. Ed.*, 2016, **55**, 6244–6247.
140 Y. Chen, Y. Wang, Z. Wang, M. Zou, H. Zhang, W. Zhao, M. Yousaf, L. Yang, A. Cao and R. P. S. Han, *Adv. Energy Mater.*, 2018, **8**, 1702981.
141 L. Luo, J. Wu, Q. Li, V. P. Dravid, K. R. Poeppelmeier, Q. Rao and J. Xu, *Nanotechnology*, 2016, **27**, 085402.
142 R. Xu, J. Lu and K. Amine, *Adv. Energy Mater.*, 2015, **5**, 1500408.
143 E. Zhao, K. Nie, X. Yu, Y.-S. Hu, F. Wang, J. Xiao, H. Li and X. Huang, *Adv. Funct. Mater.*, 2018, **28**, 1707543.
144 M. Li, Z. Amirzadeh, R. De Marco, X. F. Tan, A. Whittaker, X. Huang, R. Wepf and R. Knibbe, *Small Methods*, 2018, **2**, 1800133.
145 Z. Yang, Z. Zhu, J. Ma, D. Xiao, X. Kui, Y. Yao, R. Yu, X. Wei, L. Gu, Y.-S. Hu, H. Li and X. Zhang, *Adv. Energy Mater.*, 2016, **6**, 1600806.
146 Y. Qiu, G. Rong, J. Yang, G. Li, S. Ma, X. Wang, Z. Pan, Y. Hou, M. Liu, F. Ye, W. Li, Z. W. Seh, X. Tao, H. Yao, N. Liu, R. Zhang, G. Zhou, J. Wang, S. Fan, Y. Cui and Y. Zhang, *Adv. Energy Mater.*, 2015, **5**, 1501369.
147 K. L. Harrison, K. R. Zavadil, N. T. Hahn, X. Meng, J. W. Elam, A. Leenheer, J. G. Zhang and K. L. Jungjohann, *ACS Nano*, 2017, **11**, 11194–11205.
148 R. Xu, I. Belharouak, X. Zhang, R. Chamoun, C. Yu, Y. Ren, A. Nie, R. Shahbazian-Yassar, J. Lu, J. C. Li and K. Amine, *ACS Appl. Mater. Interfaces*, 2014, **6**, 21938–21945.
149 H. Kim, J. T. Lee, A. Magasinski, K. Zhao, Y. Liu and G. Yushin, *Adv. Energy Mater.*, 2015, **5**, 1501306.
150 D. Qian, C. Ma, K. L. More, Y. S. Meng and M. Chi, *NPG Asia Mater.*, 2015, **7**, e193–e193.
151 Z.-L. Xu, J.-Q. Huang, W. G. Chong, X. Qin, X. Wang, L. Zhou and J.-K. Kim, *Adv. Energy Mater.*, 2017, **7**, 1602078.
152 Y. Hwa, H. K. Seo, J.-m. Yuk and E. J. Cairns, *Nano Lett.*, 2017, **17**, 7086–7094.

153 Z. W. Seh, J. H. Yu, W. Li, P.-C. Hsu, H. Wang, Y. Sun, H. Yao, Q. Zhang and Y. Cui, *Nat. Commun.*, 2014, 5.
154 Y. Hwa, J. Zhao and E. J. Cairns, *Nano Lett.*, 2015, **15**, 3479–3486.
155 K. Cai, M. K. Song, E. J. Cairns and Y. Zhang, *Nano Lett.*, 2012, **12**, 6474–6479.
156 G. Tan, R. Xu, Z. Xing, Y. Yuan, J. Lu, J. Wen, C. Liu, L. Ma, C. Zhan, Q. Liu, T. Wu, Z. Jian, R. Shahbazian-Yassar, Y. Ren, D. J. Miller, L. A. Curtiss, X. Ji and K. Amine, *Nat. Energy*, 2017, 2.
157 X.-C. Liu, Y. Yang, J. Wu, M. Liu, S. P. Zhou, B. D. A. Levin, X.-D. Zhou, H. Cong, D. A. Muller, P. M. Ajayan, H. D. Abruña and F.-S. Ke, *ACS Energy Lett.*, 2018, **3**, 1325–1330.
158 Y. Wang and Y.-C. Lu, *Energy Storage Mater.*, 2020, **28**, 235–246.
159 J. F. Changwei Shi, L. Huang, X. Liu and L. Mai, *Int. J. Electrochem. Sci.*, 2013, **8**, 8924–8930.
160 H. G. Jung, J. Hassoun, J. B. Park, Y. K. Sun and B. Scrosati, *Nat. Chem.*, 2012, **4**, 579–585.
161 D. Aurbach, B. D. McCloskey, L. F. Nazar and P. G. Bruce, *Nat. Energy*, 2016, 1.
162 W. D. McCulloch, N. Xiao, G. Gourdin and Y. Wu, *Chemistry*, 2018, **24**, 17627–17637.
163 C. Wang, Y. Yu, J. Niu, Y. Liu, D. Bridges, X. Liu, J. Pooran, Y. Zhang and A. Hu, *Appl. Sci.*, 2019, **9**, 2787.
164 K. He, X. Bi, Y. Yuan, T. Foroozan, B. Song, K. Amine, J. Lu and R. Shahbazian-Yassar, *Nano Energy*, 2018, **49**, 338–345.
165 C. Hou, J. Han, P. Liu, G. Huang and M. Chen, *Nano Lett.*, 2020, **20**, 2183–2190.
166 Q. Sun, J. Liu, B. Xiao, B. Wang, M. Banis, H. Yadegari, K. R. Adair, R. Li and X. Sun, *Adv. Funct. Mater.*, 2019, **29**, 1808332.
167 B. D. McCloskey, J. M. Garcia and A. C. Luntz, *J. Phys. Chem. Lett.*, 2014, **5**, 1230–1235.
168 Y. Zhu, F. Yang, M. Guo, L. Chen and M. Gu, *ACS Nano*, 2019, **13**, 14399–14407.
169 S. Han, C. Cai, F. Yang, Y. Zhu, Q. Sun, Y. G. Zhu, H. Li, H. Wang, Y. Shao-Horn, X. Sun and M. Gu, *ACS Nano*, 2020, **14**, 3669–3677.
170 N. Xiao, R. T. Rooney, A. A. Gewirth and Y. Wu, *Angew. Chem., Int. Ed.*, 2018, **57**, 1227–1231.
171 N. Xiao, X. Ren, W. D. McCulloch, G. Gourdin and Y. Wu, *Acc. Chem. Res.*, 2018, **51**, 2335–2343.
172 X. Ren and Y. Wu, *J. Am. Chem. Soc.*, 2013, **135**, 2923–2926.
173 W. Wang, N. C. Lai, Z. Liang, Y. Wang and Y. C. Lu, *Angew. Chem., Int. Ed.*, 2018, **57**, 5042–5046.
174 P. Hartmann, C. L. Bender, M. Vračar, A. K. Dürr, A. Garsuch, J. Janek and P. Adelhelm, *Nat. Mater.*, 2012, **12**, 228–232.
175 S. Kang, Y. Mo, S. P. Ong and G. Ceder, *Nano Lett.*, 2014, **14**, 1016–1020.
176 R. Chen, Q. Li, X. Yu, L. Chen and H. Li, *Chem. Rev.*, 2020, **120**, 6820–6877.
177 M. Yousaf, H. T. H. Shi, Y. Wang, Y. Chen, Z. Ma, A. Cao, H. E. Naguib and R. P. S. Han, *Adv. Energy Mater.*, 2016, **6**, 1600490.
178 K. Yamamoto, Y. Iriyama, T. Asaka, T. Hirayama, H. Fujita, K. Nonaka, K. Miyahara, Y. Sugita and Z. Ogumi, *Electrochem. Commun.*, 2012, **20**, 113–116.
179 S. A. Pervez, M. A. Cambaz, V. Thangadurai and M. Fichtner, *ACS Appl. Mater. Interfaces*, 2019, **11**, 22029–22050.
180 D. Ruzmetov, V. P. Oleshko, P. M. Haney, H. J. Lezec, K. Karki, K. H. Baloch, A. K. Agrawal, A. V. Davydov, S. Krylyuk, Y. Liu, J. Huang, M. Tanase, J. Cumings and A. A. Talin, *Nano Lett.*, 2011, **12**, 505–511.
181 Y. Nomura, K. Yamamoto, T. Hirayama, M. Ohkawa, E. Igaki, N. Hojo and K. Saitoh, *Nano Lett.*, 2018, **18**, 5892–5898.
182 D. Santhanagopalan, D. Qian, T. McGilvray, Z. Wang, F. Wang, F. Camino, J. Graetz, N. Dudney and Y. S. Meng, *J. Phys. Chem. Lett.*, 2014, **5**, 298–303.
183 Y. Nomura, K. Yamamoto, M. Fujii, T. Hirayama, E. Igaki and K. Saitoh, *Nat. Commun.*, 2020, **11**, 2824.
184 C. Ma, Y. Cheng, K. Yin, J. Luo, A. Sharafi, J. Sakamoto, J. Li, K. L. More, N. J. Dudney and M. Chi, *Nano Lett.*, 2016, **16**, 7030–7036.
185 J. A. Lewis, F. J. Q. Cortes, M. G. Boebinger, J. Tippens, T. S. Marchese, N. Kondekar, X. Liu, M. Chi and M. T. McDowell, *ACS Energy Lett.*, 2019, **4**, 591–599.
186 J. Zhu, J. Zhao, Y. Xiang, M. Lin, H. Wang, B. Zheng, H. He, Q. Wu, J. Y. Huang and Y. Yang, *Chem. Mater.*, 2020, **32**, 4998–5008.
187 X. Tao, Y. Liu, W. Liu, G. Zhou, J. Zhao, D. Lin, C. Zu, O. Sheng, W. Zhang, H. W. Lee and Y. Cui, *Nano Lett.*, 2017, **17**, 2967–2972.
188 C.-Y. Huang, Y.-T. Tseng, H.-Y. Lo, J.-K. Chang and W.-W. Wu, *Nano Energy*, 2020, **71**, 104625.
189 Q. Cheng, A. Li, N. Li, S. Li, A. Zangiabadi, T.-D. Li, W. Huang, A. C. Li, T. Jin, Q. Song, W. Xu, N. Ni, H. Zhai, M. Dontigny, K. Zaghib, X. Chuan, D. Su, K. Yan and Y. Yang, *Joule*, 2019, **3**, 1510–1522.
190 Y. Gong, J. Zhang, L. Jiang, J. A. Shi, Q. Zhang, Z. Yang, D. Zou, J. Wang, X. Yu, R. Xiao, Y. S. Hu, L. Gu, H. Li and L. Chen, *J. Am. Chem. Soc.*, 2017, **139**, 4274–4277.
191 J. Xie, J. Li, W. Mai and G. Hong, *Nano Energy*, 2021, **83**, 105780.
192 J. N. Reimers and J. R. Dahn, *J. Electrochem. Soc.*, 2019, **139**, 2091–2097.
193 P. Hou, G. Chu, J. Gao, Y. Zhang and L. Zhang, *Chin. Phys. B*, 2016, **25**, 016104.
194 Y. Gong, Y. Chen, Q. Zhang, F. Meng, J. A. Shi, X. Liu, X. Liu, J. Zhang, H. Wang, J. Wang, Q. Yu, Z. Zhang, Q. Xu, R. Xiao, Y. S. Hu, L. Gu, H. Li, X. Huang and L. Chen, *Nat. Commun.*, 2018, **9**, 3341.
195 Y. Nomura, K. Yamamoto, T. Hirayama, E. Igaki and K. Saitoh, *ACS Energy Lett.*, 2020, **5**, 2098–2105.
196 Y. Chen, Z. Wang, X. Li, X. Yao, C. Wang, Y. Li, W. Xue, D. Yu, S. Y. Kim, F. Yang, A. Kushima, G. Zhang, H. Huang, N. Wu, Y. W. Mai, J. B. Goodenough and J. Li, *Nature*, 2020, **578**, 251–255.
197 M. Kuhne, F. Borrnert, S. Fecher, M. Ghorbani-Asl, J. Biskupek, D. Samuelis, A. V. Krasheninnikov, U. Kaiser and J. H. Smet, *Nature*, 2018, **564**, 234–239.

198 X. Wang, M. Zhang, J. Alvarado, S. Wang, M. Sina, B. Lu, J. Bouwer, W. Xu, J. Xiao, J. G. Zhang, J. Liu and Y. S. Meng, *Nano Lett.*, 2017, **17**, 7606–7612.
199 M. Sun, T. Liu, Y. Yuan, M. Ling, N. Xu, Y. Liu, L. Yan, H. Li, C. Liu, Y. Lu, Y. Shi, Y. He, Y. Guo, X. Tao, C. Liang and J. Lu, *ACS Energy Lett.*, 2021, **6**, 451–458.
200 B. Zhang, H. Shi, Z. Ju, K. Huang, C. Lian, Y. Wang, O. Sheng, J. Zheng, J. Nai, T. Liu, Y. Jin, Y. Liu, C. Zhang and X. Tao, *J. Mater. Chem. A*, 2020, **8**, 26045–26054.
201 M. J. Zachman, J. A. Hachtel, J. C. Idrobo and M. Chi, *Angew. Chem., Int. Ed.*, 2020, **59**, 1384–1396.
202 D. Chao, W. Zhou, F. Xie, C. Ye, H. Li, M. Jaroniec and S.-Z. Qiao, *Sci. Adv.*, 2020, **6**, eaba4098.
203 M. E. Holtz, Y. Yu, D. Gunceler, J. Gao, R. Sundararaman, K. A. Schwarz, T. A. Arias, H. D. Abruna and D. A. Muller, *Nano Lett.*, 2014, **14**, 1453–1459.
204 L. Xiao, Z. Ding, C. Chen, Z. Han, P. Wang, Q. Huang, P. Gao and W. Wei, *iScience*, 2020, **23**, 100898.
205 Z. Ding, C. Yang, J. Zou, S. Chen, K. Qu, X. Ma, J. Zhang, J. Lu, W. Wei, P. Gao and L. Wang, *Adv. Mater.*, 2020, **33**, 2006118.
206 J. Cai, R. Cai, Z. Sun, X. Wang, N. Wei, F. Xu, Y. Shao, P. Gao, S. Dou and J. Sun, *Nano-Micro Lett.*, 2020, 12.
207 W. Tang, Z. Chen, B. Tian, H. W. Lee, X. Zhao, X. Fan, Y. Fan, K. Leng, C. Peng, M. H. Kim, M. Li, M. Lin, J. Su, J. Chen, H. Y. Jeong, X. Yin, Q. Zhang, W. Zhou, K. P. Loh and G. W. Zheng, *J. Am. Chem. Soc.*, 2017, **139**, 10133–10141.
208 Z. D. Hood, X. Chen, R. L. Sacci, X. Liu, G. M. Veith, Y. Mo, J. Niu, N. J. Dudney and M. Chi, *Nano Lett.*, 2021, **21**, 151–157.